Transformation of valence signaling in a striatopallidal circuit

Donghyung Lee[1], Nathan Lau, Lillian Liu[1], and Cory M. Root[1]

[1] University of California San Diego, Department of Neurobiology, School of Biological Sciences, San Diego, California

Abstract

The ways in which sensory stimuli acquire motivational valence through association with other stimuli is one of the simplest forms of learning. Though we have identified many brain nuclei that play various roles in reward processing, a significant gap remains in understanding how valence encoding transforms through the layers of sensory processing. To address this gap, we carried out a comparative investigation of the anteromedial olfactory tubercle (OT), and the ventral pallidum (VP) - 2 connected nuclei of the basal ganglia which have both been implicated in reward processing. First, using anterograde and retrograde tracing, we show that both D1 and D2 neurons of the anteromedial OT project primarily to the VP and minimally elsewhere. Using 2-photon calcium imaging, we then investigated how the identity of the odor and reward contingency of the odor are differently encoded by neurons in either structure during a classical conditioning paradigm. We find that VP neurons robustly encode reward contingency, but not identity, in low-dimensional space. In contrast, the OT neurons primarily encode odor identity in high-dimensional space. Although D1 OT neurons showed larger responses to rewarded odors than other odors, consistent with prior findings, we interpret this as identity encoding with enhanced contrast. Finally, using a novel conditioning paradigm that decouples reward contingency and licking vigor, we show that both features are encoded by non-overlapping VP neurons. These results provide a novel framework for the striatopallidal circuit in which a high-dimensional encoding of stimulus identity is collapsed onto a low-dimensional encoding of motivational valence.

Introduction

Animals exhibit an impressive ability to change how sensory inputs map onto behavioral outputs. Understanding how animals learn to output different behaviors through experience is one of the fundamental problems in neuroscience. Over the last half century, the field has developed compelling frameworks to tackle this problem at both the algorithmic level (Rescorla-Wagner models, Q-learning models) (Rescorla, 1972; Sutton, 1988) and the mechanistic level (Hebbian learning, STDP, neuromodulation) (Dan and Poo, 2004). By comparison, we lack frameworks through which to understand how the brain might implement learning algorithms through the updating of synaptic weights. One strategy has been to identify neural correlates of latent features assumed to be required for these algorithms (e.g. dopamine as a neural substrate for reward-prediction-error) (Hollerman and Schultz, 1998; Schultz et al., 1997). These results, however, can often be difficult to interpret because reward related signals are found globally throughout the brain (Allen et al., 2019), and are likely multiplexed with signals about motor output and/or stimulus identity. We propose that a more powerful approach is one that compares 1) how the encoding of reward cues changes from one brain nucleus to its downstream target and 2) how much of the encoding can be explained by valence vs. other features such as identity or motor output. In this present work, we implement this comparative approach to the investigation of how encoding of olfactory reward cues is transformed between the olfactory tubercle (OT) and the ventral pallidum (VP) in the context of classical conditioning.

The OT, also known as the tubular striatum (Wesson, 2020), is a 3-layered striatal nucleus situated at the bottom of the forebrain. As with other striatal structures, the OT is composed primarily of Spiny Projection Neurons (SPN's) which express either the *Drd1* or *Drd2* DA receptors (abbreviated as OT_{D1} and OT_{D2}, respectively) (Tritsch and Sabatini, 2012). In addition to receiving a wide range of inputs from cortical and amygdalar areas (e.g. AI, OFC, BLA, PlCoA, Pir) (Zhang et al., 2017b), it receives dense DAergic input from the midbrain (Ikemoto, 2007) and direct input from the mitral and tufted cells of the olfactory bulb (Haberly and Price, 1977; Igarashi et al., 2012; Scott, 1981), a unimodal and primary sensory area. There is a range of experiments that suggest that the OT's DAergic innervation is involved in reward processing. Coincident stimulation of the lateral olfactory tract and DAergic midbrain afferents supports LTP of excitatory current (Wieland et al., 2015) and rats self-administer cocaine, a DAergic drug, into the medial OT more vigorously than to any other striatal nuclei (Ikemoto,

52 2003). And while the OT neurons are known to respond to a wide range of odorants (Wesson
53 and Wilson, 2010), pairing stimulation of midbrain DAergic neurons with an odor drives
54 appetitive behavior towards the paired odor (Zhang et al., 2017a) and enhances the contrast of
55 the odor-evoked activity (Oettl et al., 2020). Lastly, a number of recent publications report
56 varying degrees of valence signals recorded from neurons in the OT (Gadziola et al., 2020,
57 2015; Martiros et al., 2022; Millman and Murthy, 2020; Oettl et al., 2020).
58 The most well-established target of the OT is the VP (Newman and Winans, 1980; Zahm
59 and Heimer, 1987), a pallidal structure that lies immediately dorsal to the OT. In addition to OT
60 input, VP receives strong input from the nucleus accumbens (Jones and Mogenson, 1980) and
61 the subthalamic nucleus (Ricardo, 1980; Turner et al., 2001). More recently, it was reported that
62 VP also receives inputs from several cortical and amygdalar areas that also project to the OT
63 (e.g. Pir, BLA, OFC) (Stephenson-Jones et al., 2020). The VP contains GABAergic neurons,
64 which respond to positive valence cues, and glutamatergic neurons, which respond to negative
65 valence cues. Consistent with their responsiveness, the GABAergic and glutamatergic neurons
66 drive real time place preference and avoidance, respectively (Faget et al., 2018). Though it is
67 well-established that the VP plays a critical role in reward processing, there has been ongoing
68 disagreement on what specific latent features are encoded by VP neurons. Interpretations have
69 included valence (Ottenheimer et al., 2018, 2020b; Richard et al., 2016; Tachibana and
70 Hikosaka, 2012), hedonics (Smith et al., 2009; Tindell et al., 2006), motivation (Faget et al.,
71 2018; Fujimoto et al., 2019; Lederman et al., 2021; Tindell et al., 2005), and reward-prediction
72 error (Ottenheimer et al., 2020a). This ongoing discussion highlights the need to adopt a more
73 comparative approach outlined above.
74 Here, we investigated the transformation of learned association encoding between the
75 OT and the VP. We began by refining our understanding of OT's efferents to reveal that,
76 contrary to a previous report, both OT_{D1} and OT_{D2} neurons of the anteromedial OT project
77 primarily to the ventrolateral portion of the VP and minimally elsewhere. Given this finding that
78 VP may be the only robust output of the anteromedial OT, we proposed that the OT to VP circuit
79 is an ideal model system for examining how the encoding of reward cues is transformed
80 between connected brain areas. Comparing the stimulus-evoked activity in anteromedial OT_{D1},
81 OT_{D2}, and VP neurons with 2-photon Ca^{2+} imaging, we found that VP neurons encode reward-
82 contingency in low-dimensional space with good generalizability. In contrast, activity in both
83 OT_{D1} and OT_{D2} neurons was high-dimensional and primarily contained information about odor

84 identity, though OT_{D1} neurons are modulated by reward. By examining the same neurons
85 across multiple days of pairing, we propose a putative cellular mechanism for reward-cue
86 responsiveness in VP wherein reward responsive VP neurons gradually become reward-cue
87 responsive. Finally, using a novel classical conditioning paradigm, we provide evidence that
88 non-overlapping sets of VP neurons contain information about the vigor of licking and reward-
89 contingency, but not both.

Results

In order to compare odor-evoked activity in connected brain nuclei, we first characterized which specific subregions of the VP receive input from the anteromedial portion of the OT. While considerable effort has been made to unravel the anatomy and function of the NAc, much less attention has been directed at the OT. Though multiple studies have characterized its anatomical connectivity (Zahm and Heimer, 1987; Zhang et al., 2017b; Zhou et al., 2003), there is inconsistency regarding whether or not OT projects to areas other than the VP. We therefore aimed to clarify previously reported OT connectivity by independently conducting anterograde viral tracing experiments in OT_{D1} and OT_{D2} neurons of the anteromedial OT. To this end, we injected AAVDJ-hSyn-FLEX-mRuby-T2A-syn-eGFP in the anterior OT of *Drd1*-Cre (labels D1+ SPN's) and *Adora2a*-Cre (labels D2+ SPN's) animals (Fig1A, FigS1C-E). Because viral contamination of areas dorsal to the target site can lead to difficulties in interpretation of tracing data, we also injected the same virus to the AcbSh immediately dorsal to the OT for comparison. Consistent with past findings (Kupchik et al., 2015), we observed robust projections VP, LH, and VTA from $AcbSh_{D1}$ neurons and primarily VP projections $AcbSh_{D2}$ neurons (Fig1B-C). We also observed dense labeling of the VP in D1-Cre and A2A-Cre animals injected at the OT. Contrary to one report (Zhang et al., 2017b) but consistent with another (Zhou et al., 2003), we observed minimal labeling in LH and VTA, or anywhere else in the brain, for both OT_{D1} and OT_{D2} experiments (Fig1B-C, FigS1A-B), suggesting that neither OT subpopulation from the anteromedial OT projects strongly outside the VP. As previously reported (Groenewegen and Russchen, 1984). It is also notable that OT projections were restricted to the lateral portions of the VP.

To corroborate and more precisely describe the OT to VP projection, we conducted retrograde tracing by injecting CTB::488 and CTB::543 to the lateral and medial portion of caudal VP, respectively (Fig1D, FigS1F-G). We found strong labeling of soma by both CTB::488 and CTB::543 in the Acb, AI, and Pir (Fig1E-F). By comparison, we found predominantly CTB:488, but not CTB::543, labeling in OT soma, indicating OT neurons are more likely to project to the lateral portion of the VP than to the medial. Similarly, to corroborate the lack of OT to VTA projection, we injected CTB::647 into the VTA (Fig1G, FigS1H-I). Consistent with previous findings (Beier et al., 2015; Faget et al., 2016; Watabe-Uchida et al., 2012), we found dense labeling of soma in various areas of the striatum such as AcbSh, AcbC, and CPu (Fig1H-

121 I). We also found some labeling of soma in some frontal cortical regions such as PrL, AI and IL
122 cortices. In contrast, we found that hardly any neurons within any part of the OT were labeled.
123 The rare OT neurons that did have CTB labeling were exclusively localized to the dorsal most
124 portion of layer III, closely bordering the VP. Taken together, we conclude that both D1 and D2
125 SPN's of the anteromedial OT project primarily to the lateral portion of the VP and negligibly to
126 other brain areas, including the VTA.
127 Once we had identified that the anteromedial OT has extremely constrained outputs to
128 the lateral VP, we set out to comparatively characterize the encoding of reward cue in this
129 striatopallidal circuit. Past analysis of valence encoding is confounded by not accounting for the
130 difficult-to-avoid overlaps among identity, salience, and reward contingency. To address this, we
131 carefully designed a 6-odor conditioning paradigm where these factors could be decoupled
132 (Fig2A). During each trial, the animal is exposed to 1 of 6 odors for 2 seconds. At the end of
133 odor delivery, the animal either receives: 2 µl of a 10% sucrose solution (S), 50 ms of airpuff at
134 70 psi (P) or nothing (X). 3 of the odors are ketones (hexanone, heptanone, octanone) and the
135 rest are terpenes (terpinene, pinene, limonene), but the pairing contingencies are chosen such
136 that each contingency group (S, P, or X) includes 1 ketone and 1 terpene. We reason that in a
137 valence-encoding population, but not in an identity-encoding population, we should see that
138 odor pairs of different reward-contingency (e.g. S_K, a sucrose-paired ketone vs. P_K, an airpuff-
139 paired ketone) are more different than odor pairs of same reward-contingency (e.g. S_K, a
140 sucrose-paired ketone vs. S_T, a sucrose-paired terpene). Additionally, because both sucrose-
141 pairing and airpuff-pairing should make the associated odor more salient, we can disambiguate
142 between increased discriminability due to salience vs. valence by comparing neural activity in
143 response to sucrose-cues or airpuff-cues.
144 To record the activity of the anteromedial OT and VP neurons across multiple days of
145 pairing, we injected C57BL/6 mice with AAV9-hSyn-jGCaMP7s-WPRE (lateral VP) and *Drd1*-
146 Cre or *Adora2a*-Cre animals with AAV9-hSyn-FLEX-jGCaMP7s-WPRE (anteromedial OT)
147 (Fig2B, FigS2A-F). Additionally, we implanted a 600µm Gradient Refractive Index (GRIN) lens
148 150µm dorsal to the virus injection site and cemented a head-fixation plate to the skull. 6-8
149 weeks after surgery, animals were water-restricted and habituated for 3-5 days in the head-
150 fixation setup (Fig2C). We processed the acquired time-series images using Constrained
151 Nonnegative Matrix Factorization (Pnevmatikakis et al., 2016) to obtain fluorescence traces
152 from each putative neuron (Fig2D,E). In total, we recorded Ca^{2+} signals from 231 OT_{D2} neurons

153 from 6 *Adora2a*-Cre animals (FigS3), 288 OT_{D1} neurons from 6 *Drd1*-Cre animals (FigS4) and
154 130 VP neurons from 5 C57BL6/J animals (FigS5).
155 After 3 days of odor-sucrose associations, the animals displayed anticipatory licking
156 behavior primarily during sucrose-paired odors (Fig2F,G). Starting on day 4, the sucrose and
157 airpuff contingencies were switched such that every odor had a reassigned contingency. By day
158 6, animals had adapted their anticipatory licking behavior to match the new sucrose-contingency
159 (Fig2G). Quantification of the animal's licking behavior showed that the accuracy of animals'
160 licks during odor increased across time and was not different across lens-placement groups
161 (Fig2H, TableS4,S5; ANOVA: F_{day}=27.64, p_{day}=2.29e-16, $F_{lens\ location}$=2.30, $p_{lens\ location}$=0.11).
162 These results show that the animals learn to associate S odors with reward in a flexible manner
163 in our paradigm. Because we saw the strongest behavioral evidence that animals learned odor-
164 sucrose associations by day 6, we focused our analysis on how reward cues are encoded on
165 the last day of imaging. The animals also showed trends of behavioral changes in response to
166 airpuff-cues, though they were not significant: during airpuff-cues, animals walked less and
167 closed their eyes more than during other odors (FigS6D-G, TableS32-S36). These behavioral
168 changes for aversive cues were less robust than that for reward association. However, animals
169 show clear responses to the US indicating that they perceive the aversive stimulus.
170 OT and VP neurons showed heterogeneous responses to 6 odors across all 6 days of
171 imaging (FigS3, FigS4, FigS5). To unbiasedly describe the difference between regions, we
172 performed hierarchical clustering on the pooled trial-averaged responses to the 6 odors on the
173 6th day of imaging (Fig3A). We observed both inhibitory (clusters I, II) and excitatory (clusters
174 III-VI) responses to odors as well as broad (clusters II, VI) and narrow (clusters IV, V) odor-
175 tuning (Fig3B). Cluster I and cluster III most closely fit our description of putative valence-
176 encoding neurons, i.e. neurons that had similar responses to 2 sucrose-cues (S_K vs. S_T) but
177 different responses to a sucrose-cue and a puff-cue or control odor (S_K vs. P_K or X_K). Although
178 all clusters included neurons from all subpopulations, cluster I and cluster III, which showed
179 larger responses to odors predicting sucrose, were enriched for VP neurons (Fig3C), leading us
180 to hypothesize that individual neurons in the VP were more likely to be valence encoding
181 neurons than in either anteromedial OT subpopulation.
182 To assess this hypothesis, we quantified the number of neurons that had statistically
183 significant responses to each of the 6 odors on the last day of imaging. We found that more VP
184 neurons were either excited (29.8±4.1%, 36.6±4.0% for S_K, S_T) or inhibited (24.5±3.0%,

185 29.4±3.8% for S_K, S_T) to either sucrose-paired odor than to control or puff-paired odors (7.6-
186 11.1% excited, 8.1-12.9% inhibited) (Fig3D, FigS8A). For statistical comparisons see (FigS8B,
187 TableS37). When compared across days, we found that the percentage of VP neurons that
188 respond to both S odors increases from 6.1±2.2% on day 1 to 34.1±5.1% by the 6th day of
189 imaging (Fig3E,TableS11). By comparison, the percentage of OT neurons that respond to both
190 S odors in the same direction (i.e. excited by both S odors or inhibited by both S odors) did not
191 increase through training. Furthermore, whereas OT_{D1} and OT_{D2} neurons were more likely to
192 respond to a single odor than they were to respond to both S odors (12.6 vs 31.3% in OT_{D1},
193 11.8 vs 21.7% in OT_{D2}), VP neurons were more likely to respond to both S odors than to a
194 single odor (34.1 vs 23.3%).
195 Similarly, we found that the magnitude of trial-averaged odor responses in the VP were
196 significantly higher for S odors than X or P odors on the last day of imaging (FigS9, TableS38).
197 By comparison, neither sucrose-pairing nor airpuff-pairing had any impact on the magnitude of
198 odor responses in OT_{D2} neurons on day 6. And though we did observe a significant effect of
199 sucrose-pairing on response magnitudes in OT_{D1} neurons, both the effect size and significance
200 were weaker than observed in VP. We propose that an ideal valence-encoding neuron should
201 respond similarly to 2 odors of equal reward-contingency but disparate molecular structure, and
202 we looked at the correlation between each neuron's response to the sucrose-paired ketone (S_K)
203 and to the sucrose-paired terpene (S_T). VP neurons had a high correlation between a neuron's
204 responses to S_K and S_T (Fig3F; R^2=0.89). This similarity was much higher than between the
205 sucrose-paired ketone (S_K) and the control ketone (X_K) despite the greater structural similarity
206 between S_K and X_K (Fig3G; R^2=0.33). In contrast, for both OT_{D1} and OT_{D2} neurons, there was a
207 higher correlation between responses to similar molecular structure (S_k and $X_{K,}$) than between
208 responses to similar contingency (S_K and S_T) (OT_{D2}: S_K vs. S_T R^2=0.04, S_K vs. X_K R^2=0.58; OT_{D1}:
209 S_K vs. S_T R^2=0.13, S_K vs. X_K R^2=0.40). Moreover, most VP neurons (76.5%), had a smaller
210 absolute difference in the response magnitude to the 2 S odors ($|S_K-S_T|$) than the absolute
211 difference between the sucrose-paired ketone and the control ketone ($|S_K-X_K|$) (Fig3H). By
212 comparison, only half of OT_{D2} and OT_{D1} neurons showed smaller $|S_K-S_T|$ than $|S_K-X_K|$, as would
213 be expected if response magnitude to an odor did not depend on reward-contingency. This
214 trend was not due to the fact that VP neurons were more likely to respond to both S odors than
215 the OT neurons were since it was consistent across various thresholds for odor response

magnitude. This trend was consistent for other pairwise odor comparisons where one odor was a sucrose-cue and the other was not (e.g. S_K vs. P_T, FigS10A-B).

Finally, we reasoned that the activity of reward-contingency encoding neurons would support good decoding of odor pairs which have different valence but not of odor pairs that have the same valence. To do this, we trained binary logistic classifiers from each neuron's response to all 15 odor pairs and quantified the area under their receiver operating characteristic (auROC). Because auROC values were non-normal with large spread, we quantified what percentage of neurons had an auROC of at least 0.75, halfway between ideal and at-chance decoding. We also note that all classifiers with auROC>0.75 showed bootstrapped p-values less than 10^{-3} (FigS10C-D). To assess whether neurons from each region were encoding valence, we compared a neuron's {S_K vs. X_K} decoder performance (*inter*valence classification) against its {S_K vs. S_T} decoder performance (*intra*valence classification) (Fig3I-K, FigS10E-F). Across multiple days of imaging, we found that the percentage of neurons that support intervalence classification increased regardless of region but that this effect was markedly more pronounced among VP neurons than among OT_{D1} or OT_{D2} neurons (Fig3I-J, TableS12-S15, FigS10F, TableS39-S41). Intravalence classification, however, did not depend on days or region (Fig3K, TableS16-S17, FigS10F, TableS42-S44). By day 6, there were thrice as many VP neurons with good intervalence decoding than with intravalence decoding (51.8±5.0% vs. 14.4±5.8% for {S_K vs X_K} and {S_K vs S_T}, respectively). In contrast, a similar number of OT neurons displayed good intervalence decoding as did intravalence decoding (20.8% vs 19.9% of OT_{D1}; 12.8% and 21.0% of OT_{D2} for {S_K vs X_K} and {S_K vs S_T}, respectively). The pattern of better intervalence decoding than intravalence decoding among VP neurons was observed across all 15 pairwise classifiers (FigS10H). Whereas 10.2% of all day 6 VP neurons had auROC>0.75 for {S_K vs. S_T}, 46.9-57.8% had auROC>0.75 for any classification between a sucrose-cue and a control odor or airpuff-cue. By comparison, there were few neurons with auROC>0.75 for any classification between a puff-cue and a control odor (2.3-10.9%), suggesting that negative valence is either not encoded in these VP neurons or the negative valence was not learned.

Plotting a neuron's {S_K vs. S_T} auROC against its {S_K vs. X_K} auROC, we can categorize a neuron into the 4 categories (Fig3L). 1) a valence encoding neuron ({S_K vs. S_T}<0.75 and {S_K vs. X_K}>0.75), 2) an identity encoding neuron (both auROC>0.75), 3) an identity encoding neuron that does better with S odors ({S_K vs. S_T}>0.75 and {S_K vs. X_K}<0.75), and 4) an uninformative neuron (both auROC<0.75). According to this categorization, half of VP neurons

248 were valence encoding by day 6, followed by OT_{D1} then OT_{D2} (Fig3M-N; 47.7, 16.2, 7.3% for
249 VP, OT_{D1}, and OT_{D2}, respectively). The opposite was true for identity encoding. VP had a
250 smaller percentage of identity encoding neurons than either OT_{D1} or OT_{D2} (14.8, 21.1, 22.9% for
251 VP, OT_{D1}, and OT_{D2}, respectively). We note that these conclusions can also be replicated when
252 analyzing multinomial regression (MNR) classifiers trained on single neuron activities (FigS11F-
253 G, TableS50-S53). Namely, the rates of confusion between the 2 sucrose cues are highest in
254 VP and lowest in OT_{D2} whereas the rates of confusion across all ketones (S_K, X_K, P_K) are
255 highest in OT_{D2} and lowest in VP. These single-neuron classifier analyses further indicate that
256 VP neurons, more than either OT_{D2} or OT_{D1} neurons, were encoding reward contingency at the
257 single neuron level. However, the most striking observation was that while only a subset
258 (37.5%) of VP neurons had auROC<0.75 for both {S_K vs. X_K} and {S_K vs. X_K}, a majority of OT_{D2}
259 and OT_{D1} neurons (69.7% and 62.6%, respectively) showed auROC<0.75 for both {S_K vs. S_T} or
260 {S_K vs. P_K}. Thus, in comparison to the VP, most individual anteromedial OT neurons have little
261 discriminatory information about olfactory stimuli regardless of valence at the single-neuron
262 level and may be better suited in a population code.
263 Our data indicated that valence encoding emerges in VP neurons over the course of
264 learning. To explore the potential mechanisms at the cellular level, we compared the activity of a
265 subset of neurons we could observe on both day 1 and day 3 (Fig4A-F). We noticed there were
266 neurons that responded to the sucrose delivery on day 1 that responded to the sucrose cue on
267 day 3 (Fig4C,F), reminiscent of models of Hebbian plasticity. When quantified, we found that
268 17.9, 20.9% of VP neurons were responsive to sucrose on day 1 and S_K and S_T on day 3,
269 respectively (Fig4G). We specifically considered neurons that had the same direction of
270 response (excitation or inhibition) to both cues on separate days. This figure was much lower
271 among OT subpopulations (11.5, 8.2% for S_K and S_T in OT_{D1}; 10, 2.5% for S_K and S_T in OT_{D2}).
272 Consistent with above observations, we also found that the odor responses to sucrose-cues
273 were larger on day 3 than day 1 in 85% of tracked VP neurons, but only in 65% and 57% of
274 OT_{D1} and OT_{D2} neurons, respectively (Fig4H-I, TableS18-S19). We did not see the same effect
275 in VP neurons' responses to control or puff-paired odors. Together, our data suggest that
276 sucrose pairing causes sucrose-responsive VP neurons to increase their responses to the
277 sucrose-predictive odors.
278 Olfactory brain areas are known to use population codes to encode sensory information,
279 whereby single neurons have weak discriminatory information, but the activity of the population

allows for an efficient encoding of high-dimensional data. To assess if there is discriminatory information about the odorants within the population-level activity, we compared the pairwise Euclidean distance of trial-averaged odor responses for all 15 odor pairs (Fig5A,B). We saw that, in general, the pairwise Euclidean distance for all odor pairs examined increases quickly after the onset of odor, reaches peak distance towards the end of the 2 second odor delivery, and slowly decays after odor ends (Fig5A). When examining the average pairwise distance during the last second of odor, there was a relatively unstructured distribution of pairwise distance in OT_{D2} odor-response such that $||S_K-X_K||$, $||S_K-P_K||$, $||S_K-S_T||$, and $||X_K-X_T||$ were all similar (Fig5B). By comparison, in VP populations, the distribution was structured such that intervalence pairwise comparisons between sucrose-paired and not sucrose-paired odors (e.g. $||S_K-P_K||$ and $||S_K-X_K||$) were larger than intravalence pairwise comparisons (e.g. $||S_K-S_T||$, or $||X_K-X_T||$). OT_{D1} populations showed an intermediate trend where most intravalence pairwise distances were smaller than intervalence pairwise distances with the exception of $||S_K-S_T||$. Thus, at the population level VP representations appear to encode valence but not identity, whereas the anteromedial OT representations encode some valence information but appear to be better suited for identity encoding.

In parallel, we also performed decoding analysis using linear classifiers to assess how reliably a given pair of odors could be decoded from population-level activity (Fig5C-D). To quantify this, we extracted the average $\Delta F_{i,k}/F$ values for each trial $i \in [1,m]$ and each neuron $k \in [1,n]$. The resulting matrix of size m x n was used to train a binary linear classifier with a logistic learner. For each classifier, we looked at the average accuracy across 5-fold cross-validation (CV accuracy). Classifiers were trained on simultaneously recorded populations (i.e. neurons from the same animal recorded on the same day) to capture biological variability. A total of 765 pairwise linear classifiers were trained (15 pairwise comparisons, 17 animals, and 3 days). When compared against 10,000 shuffles, 569 of these classifiers showed bootstrapped p-value less than 0.001 (FigS12A). Importantly, all classifiers with CV accuracy higher than 0.75 had p-value less than 0.001.

Linear classifiers trained on day 6 OT_{D2} population data had similar ranges of accuracy regardless of valence (Fig5D). For example, the intravalence classification $\{S_K$ vs. $S_T\}$ was more accurate (86.6±3.9**%**) than some and intervalence classifications (e.g. $\{S_K$ vs. $X_K\}$, 72.8±5.4**%**) but less accurate than others (e.g. $\{S_T$ vs. $P_K\}$, 88.2±3.1**%**). Classifiers trained on VP population activity, however, always showed more accurate intervalence decoding (range: 89.5-96.1%)

312 than intravalence decoding ({S_K vs. S_T}, 79.9±6.1**%)**. Additionally, whereas OT_{D2} population
313 classifiers could decode the 2 control cues {X_K vs. X_T} at accuracy (85.8±4.2**%)** comparable to
314 sucrose-cue vs. non-sucrose-cue, VP population classifiers were consistently less accurate
315 (76.8±3.7**%)** at {X_K vs. X_T} than the aforementioned intervalence classifiers. This suggests that
316 whereas OT_{D2} encodes odor identity agnostic to the valence, VP does not encode identity at all
317 but rather encodes reward contingency or positive valence. OT_{D1} pairwise classification was a
318 mixture of the other 2 regions: sucrose-cue vs. non-sucrose-cue classification was more
319 accurate than most other pairwise classifications (range: 86.4-94.3%), but the {S_K vs. S_T}
320 classification was comparably accurate (90.9±4.7%). This rules out the interpretation that OT_{D1}
321 strictly encodes valence since the identity of 2 sucrose-cues can be decoded well.
322 To address the possibility that our results are due to the limitations of linear
323 classification, we repeated the analysis using support vector machines (SVM's) with a radial
324 basis function kernel and found we could draw the same conclusions (FigS12E). Similarly, to
325 verify our results are not epiphenomena of forcing the data into binary classification, we looked
326 at population-level MNR classifiers trained on day 6 data. Importantly, we observe high
327 confusion between 2 sucrose cues in MNR classifiers trained on VP data, but not those trained
328 on OT_{D2} or OT_{D1} data (FigS12F), corroborating through an alternate analysis method that VP
329 population activity encodes reward contingency whereas either anteromedial OT subpopulations
330 are better at encoding identity.
331 The fact that VP populations showed higher decoding for odor pairs of unequal sucrose-
332 contingency provides strong evidence that VP encodes reward-contingency more than identity.
333 Results from OT decoder analyses, however, are less intelligible: all 15 odor pairs, regardless of
334 sucrose-contingency, could be decoded with above-chance success. Though this result is
335 consistent with OT populations encoding identity rather than valence, it does not rule out the
336 possibility that valence and identity are both encoded. In the context of cue-association, 2 cues
337 of different valence cannot have the same identity, meaning that good decoding of {S_K vs. P_K}
338 can be extracted from either valence encoding or identity encoding populations. To
339 disambiguate these 2 possibilities, we looked at the generalizability of pairwise decoders.
340 Briefly, linear classifiers were trained on each of the 15 possible odor pairs. Afterwards, the
341 resulting classifier was tested on every other odor pair (Fig5E). We reasoned that if neural
342 populations encode valence in addition to identity, classifiers trained on any odor pair of unequal
343 sucrose-contingency should consistently perform above chance on a different odor pair of

unequal sucrose-contingency (e.g. train on {S_K vs. P_K}, test on {S_T vs. X_T}). In other words, given valence encoding, {S_K vs. P_K} should be discriminable in a way that can also discriminate {S_T vs. X_T}. As expected, VP population decoders were consistently generalizable when trained on odor pairs of unequal sucrose-contingency then tested on other odor pairs of unequal sucrose-contingency (Fig5F,G). OT_{D2} population decoders, on the other hand, showed negligible generalizability across pairs of unequal sucrose-contingency. Similarly to other metrics of valence encoding, we found that anteromedial OT_{D1} displayed a generalizability in between that of VP and OT_{D1}, suggesting that OT_{D1} could encode some valence in addition to identity. However, we note that the VP population, on average, outperforms OT_{D1} at generalized valence decoding (95.0±2.0**%** vs 78.5±3.9**%;** TableS22-S23).

After performing these population-level analyses, we noticed a discrepancy: although single-neuron intervalence decoding was worse in anteromedial OT than in VP (Fig3M-N), population-level intervalence decoding was comparable between either OT subpopulations and the VP (Fig5C-D). This led us to speculate that the encoding of odor information had a higher dimensionality in OT than in VP. To explicitly compare the dimensionality of VP and OT population activities, we looked at the extent to which the population vector is spread across multiple axes using principal component analysis (PCA). Dimensionality can further be quantified using the participation ratio (PR) of a population, which is the square of the sum of eigenvalues of its covariance matrix divided by the sum of the squares of its eigenvalues (Litwin-Kumar et al., 2017; Recanatesi et al., 2019). This value will have a range of 1 to n, where n is the total number of features. If a single principal component can describe all of the total population variance (i.e. the data is low-dimensional), the population will have PR equal to 1. Conversely, if every principal component equally describes n^{th} of the total variance (i.e. the data is high-dimensional), the population will have PR equal to n. Because the number of total neurons recorded was different between OT and VP experiments, we first assessed if and how the normalized PR would vary with the number of total neurons through random sampling (Fig5H). After observing a consistent decrease in PR with increasing n, we compared the PR of OT and VP animals by repeatedly subsampling a fixed number of neurons (k=15) and found that VP animals had lower PR (PR_{VP} =5.83±0.80) than either OT_{D2} (PR_{D2}=9.61±0.37) or OT_{D1} (PR_{D1}=9.24±0.44) animals after training (Fig5I, TableS24-S25). There was also a difference, however, in how valence information vs. identity information was encoded by VP populations. Though the first PC of each VP population was sufficient to train adequate {S_K vs. P_K} decoders

(CV accuracy$_{PC1}$ = 85.5±2.7%), all 15 PC's were required for comparable {S_K vs. S_T} decoding (CV accuracy$_{PC1:15}$ = 75.1±13.4%) (Fig5J-L, TableS26-S29). In either OT populations, the first PC did not support good decoding of either {S_K vs. P_K} or {S_K vs. S_T}. Together, our population-level analysis indicates that VP encodes valence, but not identity, in low-dimensional space, OT_{D2} encodes identity but not valence in high-dimensional space, and OT_{D1}, has some valence information and encodes identity in high-dimensional space.

Analyses at the single-neuron and population levels showed that VP activity encodes reward contingency, rather than the identity, of the olfactory stimulus. However, due to the task design, the reward-contingency of a stimulus was highly correlated with the vigor of licking (Fig2F). This raised concerns that some neurons classified as robust reward-contingency encoders were potentially encoding motor-related information. Indeed, many VP neurons showed consistent increases in fluorescence time-locked to the onset of a licking-bout (FigS13A-B), and could be used to train distributed lag models to predict onset of licking bouts (FigS13C). Across all VP neurons, we observed a positive and significant correlation between a neuron's valence decoding ability and licking decoding ability (FigS13D; slope=0.41, $p=2.2\times10^{-10}$, R^2=0.28). This motivated us to develop a new conditioning paradigm that could decouple reward-contingency of an odor cue from the behavioral output.

Initially, we attempted to train animals on a symmetric Go/No-Go operant task where reward delivery was contingent on licking or withholding licks during odor. However, consistent with previous findings (Gubner et al., 2010), we found that animals struggled to learn the No-Go behavior in comparison to the Go behavior (data not shown). In an operant paradigm, this leads to a problematic difference in valence of Go/No-Go cues. Consequently, we opted to develop a classical conditioning paradigm whereby licks were encouraged/discouraged by physically moving the lick spout before odor presentation (Fig6A-B).

Briefly, headfixed animals were presented with 1 of 6 odors in pseudorandomized order. During the presentation of 3 of these odors, the lick spout was moved away from the mouse with a linear stepper motor. These odors are denoted as N odors (N for No-lick spout). During the presentation of the other 3 odors, the lick spout remained within licking distance of the mouse's tongue. These odors are referred to as L odors (L for lick spout). 1 odor from each group served as a control odor that had 0% reward-contingency (L_X, N_X). The other 2 odors in each group were paired with sucrose at low (50%) or high (100%) probability (L_{lo}, L_{hi}, N_{lo}, N_{hi}).

407 We reasoned that this contingency could allow us to make pairwise comparisons where one
408 odor has a higher value but lower anticipatory licking than the other (e.g. N_{hi} vs. L_{lo}).
409 To monitor anticipatory licking in the absence of the lick spout, we trained a distributed lag
410 model (DLM) using features of the mouse's face tracked using DeepLabcut (Mathis et al., 2018)
411 (FigS13E-G). We chose to pool data across all mice from the day of the highest licking
412 differential between L_{hi} and N_{hi} odors (FigS13H) to maximize the decoupling of value and motor
413 output in our analysis. Anticipatory licking during L_{lo} or L_{hi} began during the last second of the
414 odor and increased gradually until sucrose delivery whereas licking during N_{lo} or N_{hi} was
415 delayed by about one second (Fig6C). When quantified across animals on their days of highest
416 lick differential, we found that mice consistently licked most during L_{hi}, followed by L_{lo} and N_{hi},
417 then N_{lo} (Fig6D, TableS30-S31). Mice showed little to no licking during either control odors.
418 Thus, this behavioral assay affords us the opportunity to assess the decoupled effects of
419 reward-contingency and licking vigor on neural activity.
420 To begin to characterize the presence of reward-contingency and/or licking vigor
421 encoding in the VP, we first pooled and clustered the neural activity taken from 5 animals on
422 their days of highest lick-differential (Fig6E). When clustering VP neurons into 3 clusters, we
423 found that one cluster (I) showed a largely similar inhibitory response to the 4 sucrose-paired
424 odors, but not control odors- much like cluster (I) from the previous conditioning experiment
425 (Fig3A-B, Fig6E-F). Another cluster (III) by comparison, showed a varied excitatory response to
426 each of the 4 sucrose-paired odors, much like cluster III from the previous experiment. Cluster
427 (III) neurons seemed to have a particularly strong response to L_{hi} for which there was most
428 anticipatory licking. This led us to speculate the existence of both reward-contingency encoding
429 and vigor encoding neurons in the VP.
430 To test this directly, we quantified single neuron decodability of odor pairs and examined
431 how correlated decoding along the reward-contingency axis is to decoding along vigor axis
432 (Fig6G-H). We reasoned that auROC values for {L_{hi} vs. N_{hi}} would be high for vigor encoding
433 neurons but not value encoding neurons given these 2 odors have the same reward-
434 contingency but disparate licking behaviors. Similarly, we reasoned that auROC values for {N_{hi}
435 vs. N_X} would be high for reward-contingency encoding neurons but not vigor encoding neurons
436 given there is a large difference in value but small difference in licking between these 2 odors.
437 First, we saw that while single neuron decodability along the reward-contingency axis (e.g. {N_{hi}
438 vs N_X}) was higher than along the lick axis (e.g. {L_{hi} vs N_{hi}}), there were more neurons that could

439 decode {N_{hi} vs N_X} than could decode {L_X vs N_X} at auROC>0.75 (Fig6G-H). Furthermore, we
440 saw a lack of significant correlation between the single-neuron decodability of 2 odors that had
441 similar licking but different reward-contingency ({N_{hi} vs N_X}) and the decodability of 2 odors that
442 had different licking but same reward-contingency ({L_{hi} vs. N_{hi}}) (Fig6I; slope=0.038, p=0.61,
443 R^2=0.0039). This decoupling suggests that reward-contingency and vigor information are both
444 encoded in the VP but by different populations. As a control, we saw a significant correlation
445 between 2 pairwise comparisons that both had high difference in reward-contingency ({N_{hi} vs
446 N_X} and {L_{hi} vs L_X}) (Fig6J; slope=0.60, p=3.8×10^{-10}, R^2=0.30).
447 We also performed the converse experiment where the $\Delta\Delta F/F_{baseline}$ values of each
448 neuron were linearly fitted to either 1) the reward contingency, 2) the anticipatory licking or 3)
449 both values and the interaction term. Then, we compared the ΔR^2 when either variable was
450 omitted in the model and plotted the $\Delta R^2_{\text{-valence}}$ against the $\Delta R^2_{\text{-licking}}$ (Fig6K). We reasoned that,
451 if a typical VP neuron's activity could be well-explained by either reward-contingency or vigor
452 but not both, we would see points along either x or y-intercepts. On the other hand, if a typical
453 neuron's activity could be well-explained by a linear combination of the 2 variables, we would
454 see data fall along a line of positive slope. We found that most neurons tended to have large
455 $\Delta R^2_{\text{-valence}}$ *or* large $\Delta R^2_{\text{-licking}}$ values but not both, supporting the idea that 2 largely non-
456 overlapping sets of VP neurons encode reward-contingency *or* vigor but not both.
457 Lastly, we trained linear classifiers of pairwise odor comparisons using population-level
458 activity to assess if both reward-contingency and vigor information were present in the
459 population-level activity. Consistent with single-neuron decoder analysis, we found that {L_{hi} vs
460 L_X} and {N_{hi} vs N_X} could both be decoded better than {L_X vs N_X} (Fig6L-M). Because we train
461 each classifier using simultaneously recorded neural activity (i.e. from a single animal), we had
462 a total of 75 classifiers (15 pairwise classifiers for 5 animals). The cross validated accuracies of
463 these classifiers were then fitted to a linear model of pairwise differences in either 1) reward-
464 contingency, 2) anticipatory licking, or 3) both. If the population VP activity encodes either
465 reward-contingency or vigor but not both, we expect to see one of the single-variable models
466 outperform the other greatly. But if the population VP activity encodes both variables, we expect
467 the multivariable model would outperform either single model. We found that Δlicking has a
468 weak and not significant relationship with pairwise CV accuracy (Fig6N; slope=0.076, p=0.079,
469 R^2=0.042). By comparison Δreward-contingency (or P(S), as in probability of sucrose delivery
470 following odor) had a larger and statistically significant correlation with pairwise accuracy

(Fig6O; slope=0.15, $p=3.7x10^{-4}$, $R^2=0.16$). The combined model, however, showed larger coefficients and larger R^2 than either single variable model, suggesting an additive effect of both features on CV accuracy (Fig6P; accuracy = 0.18Δlick + 0.24ΔP(S) - 0.22Δlick*ΔP(S) +0.65, $R^2=0.23$). Thus, we conclude that both reward-contingency and licking vigor are encoded in the population-level activity of VP neurons.

Discussion

Our anatomical investigations demonstrate that the primary output of the anteromedial OT is to the VP, with minimal connections to the VTA. Given its constrained connectivity, we propose that the anteromedial OT to VP circuit is an ideal model system for examining how the encoding of reward cues is transformed across brain circuits. Utilizing comparative longitudinal imaging, we found that VP, but not OT_{D2}, robustly encodes the sucrose-contingency of odors. Although our analyses revealed that sucrose-contingency influences odor-evoked responses in OT_{D1} neurons more so than in OT_{D2} neurons, other evidence suggests valence encoding is not the appropriate framework for interpreting OT_{D1} activity. Specifically, information about sucrose-contingency in OT_{D1} resides in a high-dimensional space and generalizes poorly, whereas VP encodes reward-contingency robustly in a low-dimensional and generalizable manner. Thus, we suggest that the changes in anteromedial OT_{D1} activity are more likely to reflect increased contrast of identity or an intermediate encoding of valence that also encodes identity. Finally, using a novel classical conditioning paradigm, we assigned motor-related signals and expected-value signals to non-overlapping VP subpopulations.

Some of our findings were unexpected. For example, we found no evidence that either OT_{D1} or OT_{D2} have significant extrapallidal outputs. This is in contrast to a previous study which reported that OT_{D1} neurons, and to a lesser extent, OT_{D2} neurons, project to the LH and VTA (Zhang et al., 2017b). It is possible that other parts of the OT have extrapallidal outputs, as we only performed anterograde tracing from the anteromedial portion. It is also possible that at least some of the VTA labeling Zhang and colleagues observed from anterograde viral tracing experiments could be due to backflow of the tracer virus in nuclei immediately dorsal to the OT (e.g. AcbSh). As a critical control, we provide evidence that retrograde tracing from VTA robustly labels AcbSh neurons but hardly any neurons from any part of the OT. And the few VTA projecting OT neurons we did observe were restricted to the distal portions of layer III bordering the VP. Consistent with this, quantification of OT afferents is glaringly absent from 2 independent characterizations of brainwide inputs onto VTA (Beier et al., 2015; Faget et al., 2016). In contrast, OT has been reported to be one of the most prominent inputs to both GAD2+ and Vglut2+ VP neurons (Stephenson-Jones et al., 2020). It is difficult, however, to completely rule out the existence of OT *to* midbrain projections due to the limitations of our experiments: we primarily targeted layer II in the anteromedial portion of the OT for anterograde tracing and only

508 tested the VTA with retrograde tracers. More posterior and/or lateral portions of the OT could
509 have extrapallidal outputs posterior to the VTA. Despite these caveats, the evidence suggests
510 that *Drd1*+ neurons in the anteromedial portion of the OT have little extrapallidal projections
511 when compared to the AcbSh.

512 Though we found little difference in the output patterns of anteromedial OT_{D1} and OT_{D2}
513 neurons, we observed differences in how these 2 subpopulations encode odor valence.
514 Consistent with a previous report (Martiros et al., 2022), we found that OT_{D1} activity, more than
515 OT_{D2} activity, is modulated by reward contingency. For example, OT_{D1} neurons, but not OT_{D2}
516 neurons, were more likely to respond to sucrose-paired odors than other odors. And the
517 magnitude of responses in OT_{D1} but not OT_{D2} neurons were significantly larger to sucrose-
518 paired odors than to other odors. We refrain, however, from concluding that the primary feature
519 encoded in OT_{D1} neurons is valence or reward contingency, for the following reasons. First, the
520 above-mentioned effects of sucrose-contingency on neural activity are much stronger for VP
521 than for OT_{D1}. Additionally, whereas more than 50% of VP neurons could be categorized as
522 reward-contingency encoders, this figure was less than 20% for OT_{D1}. Lastly, population-level
523 decoders trained on odor pairs of different valence can generalize in the case of VP
524 populations, but not OT_{D1} populations. While we acknowledge that there is poor standardization
525 when it comes to defining valence encoding, it is unlikely that discrepancies between our
526 conclusions and those of Martiros et al. stem from differences in interpretation alone.
527 Comparative examination of our analyses reveals clear dissimilarities in the effect-size of
528 shared metrics (e.g. % odor responsive). Given the high Z-resolution afforded by 2-photon
529 microscopy, it is probable that we recorded from different layers of the OT, which should not be
530 assumed to have identical physiology. We note that the lens placements in our experiments are
531 considerably more ventral than those reported in Martiros et al. It is possible that these neurons
532 are recorded from layer III of the OT whereas the majority of the neurons in the present study
533 are recorded from layer II. A direct comparison of layer II and layer III OT neurons and their
534 valence encoding could prove useful in understanding the discrepancies between the two
535 studies. It is also possible that some of the neurons recorded in Martiros et al. could be from the
536 rostral portion of the VP which lies immediately dorsal to layer III of the OT. Although *Adora2a*
537 and *Drd1* are not expressed as mRNA in the VP, the BAC-transgenic lines used for both the
538 present work and work by Martiros et al. label neurons in the VP.

539 Our comparison of OT and VP is reminiscent of previous comparisons made between
540 value encoding in VP and NAc (Ottenheimer et al., 2018; Richard et al., 2016). These
541 publications showed that VP encodes incentive value more robustly than the NAc. Given that
542 OT and NAc share many anatomical, physiological, and molecular traits, it is tempting to
543 speculate that the encoding schemes, too, would be similar between the 2 areas. Optogenetic
544 activation of OT_{D1} supports RTPP (Murata et al., 2019), as does activation of D1 or D2 neurons
545 of the NAc (Soares-Cunha et al., 2020). While we acknowledge stimulation experiments provide
546 unique insights that cannot be obtained from recordings alone, we note that SPN's have
547 extensive inhibitory collaterals and exhibit high-dimensional activity. Given these peculiarities of
548 the striatum, we predict that bulk stimulation leads to activity patterns well outside the
549 physiologically relevant range and that this warrants conservative extrapolations regarding OT
550 SPN's endogenous role.
551 An interesting conclusion from our work is that, within the context of our conditioning
552 paradigm, the dimensionality of neural activity was much lower in VP than in OT. Furthermore,
553 the dimensionality of the imaged subpopulations were anti-correlated with the robustness of
554 sucrose-contingency encoding: OT_{D2} displayed the highest dimensionality and lowest valence
555 encoding whereas VP displayed the lowest dimensionality and highest valence encoding. As
556 discussed elegantly by others (Chu et al., 2016; Shannon, 1948), there is generally a tradeoff
557 between the efficiency of a neural population (i.e. its total information capacity) and the
558 robustness of its encoding scheme (i.e. redundancy of encoding). Consistently, it is likely that
559 VP neurons display such robust encoding of valence, in large part, due to the loss of odor
560 identity information. By comparison, OT populations may be able to encode information about
561 the large olfactory identity space due to their high dimensionality. We speculate that the
562 extensive inhibitory collaterals among SPN's play a role in enforcing the high dimensionality of
563 OT activity. Though it is entirely unknown what anatomical or physiological strategies are used
564 to reduce VP dimensionality, we consider this an important piece of the puzzle in understanding
565 VP computations.
566 We saw little evidence of negative valence neurons in any of the 3 populations that were
567 imaged. This was surprising given previous reports of negative valence neurons in the VP
568 (Stephenson-Jones et al., 2020). We consider 2 potential explanations for this discrepancy.
569 First, it is possible that our conditioning paradigm was not sufficiently aversive for the animals.
570 Although our behavioral evidence for aversive association is significant, it is less robust than

571 sucrose association raising the possibility that the learning was insufficient. This could be due to
572 the fact that we targeted the airpuff to the animal's hindquarters rather than to the face. But we
573 note that in a previous report, airpuff delivery to the snout and to hindquarters elicited similar
574 ingress response in a burrowing assay (Fink et al., 2019). Additionally, we observed clear
575 unconditioned responses to the airpuff itself. Another possibility is that, while negative valence
576 neurons do exist in the VP, as has been reported, they were outside of our field-of-view.
577 Previous work in the VP supports positive and negative valence as being encoded by *Vgat*+ and
578 *Vglut2*+ neurons, respectively (Faget et al., 2018; Stephenson-Jones et al., 2020). Most *Vglut2*+
579 neurons are found in the dorsomedial portion of the VP, whereas our lenses were specifically
580 targeted to the ventrolateral portion where we found the most OT afferents. Given this
581 distinction, our results are not inconsistent with previous reports of negative valence neurons in
582 the VP.
583 In this work, we present evidence that may appear to contradict previous anatomical and
584 physiological characterizations of the OT. We find that the anteromedial portion of the OT sends
585 high-dimensional information about odor identity primarily to the VP and not the VTA. By directly
586 comparing OT and VP population-level activity in the same paradigm, we bridge together, for
587 the first time, the fields of OT and VP. This provides valuable context which not only helps us
588 evaluate past conclusions about valence encoding in the OT but also consider the implications
589 of the stimulus-evoked activity in the OT. This comparative approach leads us to conclude that
590 the anteromedial OT has relatively little valence information. However, our findings are not
591 generally inconsistent with what has been observed in previous studies. We do find reward
592 modulation in the OT_{D1} population, however, we do not find valence encoding single neurons
593 and the population vector does not generalize between two rewarded odors as it does in the VP.
594 Therefore, we propose that representation in the anteromedial OT reflects either an
595 intermediate representation of reward-contingency or a contrast modulation to reflect the
596 contingency.
597
598 **Speculation**
599 It is interesting to note the discrepancy between the anatomical organization of dorsal
600 striatum (DS) vs. ventral striatum (VS): SPN's of the DS project exclusively to either the
601 substantia nigra pars reticulata (SNr) of the midbrain (Drd1+) or the exterior portion of the
602 globus pallidus (GPe) (Drd2+), but Drd1+ neurons in the VS (Acb) project to both the VTA of the

603 midbrain and the ventral pallidum (Kupchik et al., 2015). The anteromedial OT appears to have
604 further limited output divergence, whereby both OTD1 and OTD2 neurons project primarily to
605 the VP. This may reflect at a gradient of anatomical connectivity where the most dorsal Drd1+
606 SPN's project primarily to the midbrain and the most ventral Drd1+ SPN's (i.e. OTD1 neurons)
607 project primarily to the pallidum. Functionally, the lack of evidence for OTD1 to midbrain
608 connectivity challenges the dichotomy of direct vs. indirect pathways in the ventral basal
609 ganglia. In this model, DA orchestrates motor initiation by oppositely modulating Drd1+ and
610 Drd2+ SPN's, which have differential downstream targets. Given the lack of clear differences in
611 OTD1 and OTD2 projections, we think this canonical model of basal ganglia connectivity
612 inadequately explains the functional consequences of DA modulation in the OT.
613 In our work, we described key differences in how reward cues are encoded in 2
614 synaptically connected nuclei. What insights can we infer about the role of OT on shaping VP
615 activity through this comparison? The most salient observation of VP activity is the large and
616 widespread excitatory responses to sucrose-cues. Though the effect size is smaller, OT_{D1}
617 neurons also showed larger excitatory responses to sucrose-cue when compared to other
618 odors. Given that these neurons are GABAergic and their primary target are the VP neurons, it
619 is difficult to explain how these 2 responses are related. We consider 3 possible explanations for
620 this paradox. First, in addition to large excitatory responses that were specific to the sucrose-
621 cues, we also observed inhibitory responses that were specific to the sucrose-cues. It is
622 possible that the excitatory VP activity during sucrose-cue presentation is driven mainly by the
623 numerous excitatory afferents (Pir, BLA, etc.) while the inhibitory VP activity is driven mainly by
624 OT_{D1} and OT_{D2} afferents. In a second model, there could be mechanisms downstream of
625 somatic activity that could explain the discrepancy. For example, though brief optical stimulation
626 of D2 neurons in Acb leads to a decrease of VP activity, prolonged activation causes an
627 increase in VP activity via the δ-opioid receptor (Soares-Cunha et al., 2020). Our experiments
628 do not provide any information on how neuropeptide release from OT neurons is different during
629 presentation of sucrose-cue vs. control odor. Similarly, we cannot measure if and how positively
630 valent stimuli change the input-output-function of OT neurons. Previous reports have found that
631 Drd2 agonism in Acb neurons leads to a decrease in collateral inhibition through a presynaptic
632 mechanism (Dobbs et al., 2016). Given that more DA is expected to be released during
633 presentation of sucrose-cues, it is plausible that the probability of GABA release from OT
634 boutons onto VP dendrites is affected. In a third and perhaps the most parsimonious model,

635 endogenous OT activity does not contribute significantly to explaining the bulk excitatory activity
636 in VP. This goes against the prevailing working model in Acb to VP circuit which assumes that
637 Acb excitation leads to VTA disinhibition by inhibiting the VP. And while there is evidence
638 supporting from bulk stimulation of D1 or D2 neurons in the Acb (Soares-Cunha et al., 2020),
639 under endogenous conditions, both Acb neurons and VP neurons are excited in response to
640 reward-cues (Lederman et al., 2021; Ottenheimer et al., 2018). Furthermore, given that
641 GABAergic synapses from SPN's to VP neurons is likely dendritic (Bolam et al., 1986), we think
642 it is unlikely that OT to VP drives large-scale shunting of action potential in the presence of
643 excitatory drive from other areas known to respond preferentially to reward cues such as the
644 BLA (Beyeler et al., 2018) or the OFC (Wang et al., 2020). We consequently propose an
645 alternate framework in which the mechanistic role of the OT in this circuit is to provide
646 spatiotemporally precise inhibition to coordinate the integration of excitatory inputs onto VP.
647 This form of inhibition could gate which excitatory synapses go through Hebbian potentiation vs.
648 anti-Hebbian depression. Under such a framework, OT would function as a high-dimensional
649 filter for VP neurons to adaptively scale its various excitatory afferents.
650
651

652 Methods

653 Stereotaxic Surgery:

654 All procedures were approved by the UCSD Institutional Animal Care and Use
655 Committee. Animals were anesthetized with isoflurane (3% for induction, 1.5-2.0% afterward)
656 and placed in a stereotaxic frame (Kopf Model 1900). Mouse blood oxygenation, heart rate and
657 breathing were monitored throughout surgery, and body temperature was regulated using a
658 heating pad (Physio Suite, Kent Scientific). A small craniotomy above the injection site was
659 made using standard aseptic technique. Virus was injected with needles pulled from capillary
660 glass (3-000-203-G/X, Drummond Scientific) at a flow rate of 2nl/s using a micropump (Nanoject
661 III, Drummond Scientific). For OT anterograde tracing experiments, 50µl of AAV9-phSyn1-
662 FLEX-tdTomato-T2A-SypEGFP-WPRE diluted to 10^{12} vg/ml (The Salk Institute GT3 core) was
663 injected into the rostral portion of the medial OT (AP: 1.6mm, ML: -1.0mm, DV: -5.375mm) in

664 *Drd1*-Cre or *Adora2a*-Cre mice. For VP retrograde tracing experiments, 100 nl of Cholera Toxin
665 Subunit B CF 488A (Biotium) was injected at into the caudal portion of the ventrolateral VP (AP:
666 0.75mm, ML: -1.4mm, DV: -5.4mm) and 100 nl of Cholera Toxin Subunit B CF 543 (Biotium)
667 was injected into the dorsomedial VP (AP: 0.75mm, ML: -1.0mm, DV: -5.35mm) in C57BL6/J
668 mice. For VTA retrograde tracing experiments, 100 nl of Cholera Toxin Subunit B CF 647
669 (Biotium) was injected to the rostral portion of the VTA (AP: -3.1mm, ML: 0.8mm, DV: -4.5mm)
670 in C57BL6/J mice. CTB injections were done at 1 mg/ml dilution in PBS. In some cases, tracers
671 were injected bilaterally and each hemisphere was analyzed independently. Following each
672 injection, the injection needle was left at the injection site for 10 minutes then slowly withdrawn.
673 For imaging experiments, the skull was prepared with OptiBond™ XTR primer and
674 adhesive (KaVo Kerr) prior to the craniotomy. After performing a craniotomy 800 um in diameter
675 centered around the virus injection site, a 27G blunt needle was used to aspirate 1.5 mm below
676 the brain surface. For OT imaging experiments, 500 ul of AAV9-syn-FLEX-jGCaMP7s-WPRE
677 (Addgene viral prep #104491-AAV9) was diluted to 10^{12} vg/ml and injected into the left and
678 rostral portion of the medial OT in D1-Cre or A2A-Cre mice. For VP imaging experiments, 300 ul
679 of AAV9-syn-jGCaMP7s-WPRE (Addgene viral prep #104487-AAV9) was diluted to 10^{12} vg/ml
680 and injected into the left and caudal portion of the ventrolateral VP in C57BL6/J mice. Following
681 the viral injection, a head-plate (Model 4, Neurotar) was secured to the mouse's skull using
682 light-curing glue (Tetric Evoflow, Ivoclar Group). At least 30 minutes after viral injection, a
683 600um GRIN lens (NA, ~1.9 pitch, GrinTech) was sterilized with Peridox-RTU then slowly
684 lowered at a rate of 500 um/min into the craniotomy until it was 200 um dorsal to the injection
685 coordinate. The lens was adhered to the surface of the skull using Tetric Evoflow. We then
686 placed a hollow threaded post (AE825ES, Thorlabs) to act as a housing for the lens and
687 adhered it using Tetric Evoflow. Any part of the skull that was still visible was covered using
688 dental cement (Lang Dental). Finally, the housing was covered with a Nylon cap nut
689 (94922A325, McMaster-Carr) screwed onto the thread post to protect the lens in between
690 imaging. Animals were left on the heating pad until they fully recovered from anesthesia.

691 ## Histology:

692 Mice were administered ketamine (100 mg/kg) and xylazine (10 mg/kg) and euthanized
693 by transcardial perfusion with 10 ml of cold PBS followed by 10 ml of cold 4% paraformaldehyde
694 in PBS. Brains were extracted and left in a 4% PFA solution in PBS overnight. 50 um coronal

695 sections were cut on a vibratome (VT1000, Leica). A subset of tissue was labeled using the
696 following simplified staining protocol. First, brain sections were incubated for 48 hours at 4°C in
697 the primary antibody diluted in PBST (0.3% Triton-X in PBS). Brain sections were then washed
698 3 times for 15 minutes in PBST before and after incubating for 2 hours at room temperature in
699 the secondary antibody diluted in PBST. The antibodies used in this study and their dilutions
700 are: Rb α-substance P (1:1,000 dilution; 20064, Immunostar), Rb α-TH (1:1,000 dilution;
701 AB152, Millipore), Dk α-Rb Alexa Fluor™ 488 (1:2,000 dilution; A-210206, Thermo Fisher
702 Scientific), Dk α-Rb Alexa Fluor™ 647 (1:2,000 dilution; A-31573, Thermo Fisher Scientific).
703 Slices were mounted using Fluoromount with a DAPI counterstain (SouthernBiotech) and
704 imaged on an Olympus BX61 VS120 Virtual Slide Scanner and 10x objective (Olympus). Brains
705 were harvested 21-30 days or 5-7 days after surgery for anterograde and retrograde tracing
706 experiments, respectively. Brains injected for Ca^{2+} imaging were harvested within a week of the
707 last imaging session.
708 For anterograde tracing quantification, 4-6 slices containing each of the brain regions of
709 interest (VP, LH, and VTA) were analyzed per animal. To quantify the relative abundance of OT
710 axons in a given brain region, boundaries for the region were drawn on ImageJ Fiji (National
711 Institutes of Health) with reference to the Paxinos and Franklin Mouse Brain Atlas. Afterwards,
712 the percentage of the 16-bit pixels within the boundary that had intensity above 200 was
713 quantified. For retrograde tracing experiments, cells were counted manually every 4th slice.

714 Behavior

715 Mice were water restricted to reach 85-90% of their initial body weight and given access
716 to water for 5 minutes a day in order to maintain desired weight. Prior to imaging, mice were
717 habituated to the head fixation device (Neurotar) and treadmill for 3-5 days, 15-30 minutes per
718 session. The treadmill parts were 3D printed using a LCD printer (X1-N, EPAX) from publicly
719 available designs (Jackson et al., 2018). During habituation, mice were provided 10% sucrose
720 from the water spout. Walking and licking behaviors were measured using a quadrature encoder
721 (HEDR-5420-es214, Broadcom) and a capacitance sensor (1129_1, Phidgets), respectively. A
722 video feed of the animal's face was also recorded using a camera (acA1300-30um, Basler) with
723 a 8-50mm zoom lens (C2308ZM50, Arducam) at 20 Hz with infrared illumination (VQ2121,
724 Lorex Technology).

725 Odor was delivered to the mouse using a custom-built olfactometer. Compressed
726 medical air was split into 2 gas-mass flow controllers (GFC17, Aalborg). One flow controller
727 directed a constant rate of 1.5 L/min to a hollowed out teflon cylinder. The other flow regulator
728 was connected to a 3-way solenoid valve (**LHDB1223418H,** The Lee Co.). Prior to odor delivery,
729 the 3-way valve directs clean air at 0.5 L/min to the teflon cylinder. During odor delivery, the 3-
730 way valve directs air to an odor manifold, which consists of an array of 2-way solenoid valves
731 (LHDB1242115H, The Lee Co.), each connected to a different odor bottle. Depending on the
732 trial type, the appropriate 2-way valve opens, directing 0.5 L/min of air flow through the odor
733 bottle containing a kimwipe blotted with 50 ul of diluted odor. All odors were diluted in mineral oil
734 (M5310, Sigma-Aldrich) to 1.5 mmHg. The kinetics and consistency of odor delivery were
735 characterized for 30 trials of terpinene delivery using a miniature Photoionization Detector
736 (mPID) (Aurora Scientific, Inc).
737 During classical conditioning, animals were exposed to the following odors for 2
738 seconds: 3-hexanone, 3-heptanone, 3-octanone, α-terpinene, α-pinene, and (R)-(+)-limonene
739 (all odors were purchased from Sigma with the highest available purity). In days 1-3 of training,
740 each of the 6 odors and associated outcomes were provided 30 times with 12-18 seconds of
741 inter-trial interval. Hexanone and terpinene were not associated with any outcome, heptanone
742 and pinene were associated with 2 ul of 10% sucrose, and octanone and limonene were
743 associated with a 70 psi airpuff delivered to their hindquarters. Sucrose or airpuff was delivered
744 100-300 ms after the end of odor delivery. Trials were organized into 30 blocks, each of which
745 consisted of 1 trial of each of the 6 odors in randomized order. In days 4-6 of training, the
746 outcome contingencies were switched such that heptanone and limonene were not associated
747 with any outcome, octanone and terpinene were associated with 2 ul of 10% sucrose, and
748 hexanone and pinene were associated with 70 psi airpuff.
749 In the lick-no-lick paradigm, trials were also structured into 30 blocks, each of which
750 consisted of 1 trial of each of the 6 odors in randomized order. Hexanone and terpinene were
751 not associated with any outcome, heptanone and pinene were paired with 2 ul of 10% sucrose
752 at 50% chance, and octanone and limonene were paired with 2 ul of 10% sucrose at 100%
753 chance. 200 ms prior to the onset of 3 of the odors (terpinene, octanone, and limonene), the lick
754 spout was retracted 30 mm away from the animal's mouth using a linear stepper motor (BE073-
755 1, Befenybay) and driver (A4988, BIQU). The lick spout would return to its original position 100
756 ms prior to the earliest possible time of sucrose delivery.

DeepLabCut

DeepLabCut2.3.3 with Tensorflow 2.12 was used to track 4 points on the periphery of the eye during 2-photon Ca^{2+} imaging. The mini-batch k-means clustering method was used to extract a total of 100 frames (20 frames from 5 animals). These frames were labeled and used to train a Deep Neural Network (DNN) model for 100,000 iterations. After the first training session, 20 outlier frames were picked up from each video and added to the training data for a second training session. The area of the eye at a given time point was estimated as an ellipse. For the lick-no-lick paradigm, we used DeepLabCut to track the tip of the tongue, the corner of the mouth, the upper lip and the lower lip. To record licking in the absence of the lick spout, we trained a linear classifier using logistic regression of the following metrics: 1) the confidence score for the tip of the tongue, 2) the confidence score for the corner of the mouth and 3) the Euclidean distance between the upper and lower lip. Data collected from the capacitive lick sensor was used as ground truth for the classifier.

2-photon Ca^{2+} imaging in head-fixed, behaving mice

Mice were habituated to the head-fixation setup for 3 days beginning 8-10 weeks after surgery. Ca^{2+} imaging data was acquired using an Olympus FV-MPE-RS Multiphoton microscope with Spectra Physics MaiTai HPDS laser, tuned to 920 nm with 100 fs pulse width at 80 MHz. Each 128x128 pixel scan was acquired with a 20x air objective (LCPLN20XIR, Olympus), using a Galvo-Galvo scanner at 5Hz. Stimulus delivery and behavioral measurements were controlled through a custom software written in LabVIEW (National Instruments) and operated through a DAQ (USB-6008, National Instruments). Each imaging session lasted between 30-45 minutes and was synchronized with the stimulus delivery software through a TTL pulse. The imaging depth was manually adjusted to closely match that of the first imaging day such that we recorded from overlapping populations across days of imaging. Animals were excluded from analysis if a) histology showed that either the GRIN lens or the jGCaMP7s virus was mistargeted or b) the motion during imaging was too severe for successful motion-correction. 2 animals were excluded due to mistargeting and 2 animals were excluded due to excessive motion.

Image Processing:

Ca^{2+} imaging data were first motion-corrected using the non-rigid motion correction algorithm NoRMCorre (Pnevmatikakis and Giovannucci, 2017). Afterwards, neural traces were extracted from the motion-corrected data using constrained nonnegative matrix factorization (CNMF) (Giovannucci et al., 2019; Pnevmatikakis et al., 2016). Briefly, this algorithm estimates a spatial matrix (analogous to the idea of ROI's in manual processing methods) and a temporal matrix whose products equal the motion-corrected spatiotemporal fluorescence data. Spatial components identified by CNMF were inspected by eye to ensure they were not artifacts. A Gaussian Mixture Model (GMM) was used to estimate the baseline fluorescence of each neuron. To account for potential low-frequency drift in the baseline, the GMM was applied along a moving window of 2,500 frames (500 seconds). The fluorescence of each neuron at each time point *t* was then normalized to the moving baseline to calculate $\Delta F/F = F_t - F_{baseline}/F_{baseline}$. For analysis comparing the activity of the same neuron across multiple, spatial components from two different imaging days were matched manually. All subsequent analyses were performed using custom code written in MATLAB (R2022b).

Hierarchical clustering of pooled averaged responses

ΔF/F in response to all 6 odors on day 6 were averaged across trials then Z-scored. The resulting trial-average values from the following timebins were averaged across time: 1) the first second during each odor, 2) the last second during each odor, and 3) the first second after each odor. The resulting 18-element vectors were sorted into 6 clusters after agglomerative hierarchical clustering using euclidean distance and ward linkage.

Responsiveness criteria

To determine how many neurons were responsive to a given odor, we compared ΔF/F at each frame during the 2 second odor period against a pooled distribution of ΔF/F values from the 2-seconds prior to odor onset using a Wilcoxon rank sum test. The resulting p-values were evaluated with Holm-Bonferroni correction to ensure that familywise error rate (FWER) was below 0.05. We then calculated the percentage of responsive neurons for each animal to show the mean and the standard error as a function of time. We also counted the number of neurons

813 that were significantly responsive for at least 4 frames during the odor period to report the total
814 percentage of responsive neurons during odor.

815 Single neuron logistic classifiers

816 To test how reliably a single neuron's fluorescence could discriminate between 2 odors,
817 we assessed the performance of binary logistic classifiers trained on a single neuron's
818 responses to 2 odors. For each neuron and odor pair, we averaged the ΔF/F during the last
819 second of the odor exposure for each trial then Z-scored across all trials. The resulting 60-
820 element vector was used to train a linear classifier using logistic regression. The receiver
821 operator characteristic (ROC) was evaluated for each single neuron pairwise classifier and the
822 area under the curve (AUC) reported. To test if a given pairwise classifier performed
823 significantly better than chance, we compared the accuracy of each classifier against a
824 distribution of 10,000 classifiers trained on shuffled labels.

825 Normalized ΔΔF/F correlations

826 To compare the average response of a neuron to each odor, the trial-averaged ΔF/F
827 during the last second of odor exposure from each trial was averaged and then subtracted from
828 the trial-averaged ΔF/F during the 2 seconds prior to odor delivery. This ΔΔF/F value was
829 scaled to the largest positive ΔΔF/F value of each neuron for all odors. To assess the similarity
830 of the average response to a given pair of odors i and j, we looked at the null linear model in
831 which all neurons respond identically to both odors, i.e. $\Delta\Delta F_j/F = \Delta\Delta F_i/F$. To assess how well
832 this describes the data, we report the R^2 value of the fit.

833 Pairwise euclidean distance

834 To quantify the differences among population-level responses to the 6 odors, we
835 quantified the pairwise Euclidean distance between the trajectories of odor responses. First, we
836 subtracted the ΔF/F values during the 2 seconds prior to odor delivery from each frame then
837 averaged these values across trials for each odor. The pairwise Euclidean distance at each
838 frame was computed for each odor pair and normalized to the maximum pairwise distance
839 measured in all odor pairs at any time bin. These calculations were carried out separately for

each animal and then averaged across biological replicates to report the mean and the standard error.

Population pairwise classifiers

To assess the discriminability of odor responses in high-dimensional space, we measured the accuracy of binary classifiers for a given odor pair. At each time point relative to odor delivery, we pooled ΔF/F values from all trials during which either odor was presented. These values were then normalized and used to train a linear classifier using either a logistic regression or a Support Vector Machine (SVM). The accuracy of the classifier was evaluated via 5-fold cross-validation. To test if a given pairwise decoder performed significantly better than chance, we compared the accuracy of each classifier against a distribution of 10,000 classifiers trained on shuffled labels. All classifiers were trained on populations of neurons simultaneously recorded from individual mice. The resulting cross-validated accuracies were averaged across biological replicates to report the mean and the standard error.

Dimensionality analysis

To quantify the dimensionality of each simultaneously recorded neural population, we calculated its participation ratio (PR). First, we performed principal component analysis of the whole dataset using the singular value decomposition algorithm. The PR was calculated as the square of the sum of the eigenvalues of the covariance matrix divided by the sum of the square of its eigenvalues (Litwin-Kumar et al., 2017; Recanatesi et al., 2019). To account for the differences in number of recorded neurons across individuals, we bootstrapped the PR by randomly sampling *n* neurons from each dataset 1,000 times and reported the average PR value.

Statistical analysis

For simple pairwise comparisons, we used Student's t-tests or, when appropriate, Wilcoxon rank sum tests with Benjamini Hochberg correction to adjust for false discovery rate (FDR). For post hoc comparisons following ANOVA's, we used Tukey's honestly significant difference test which adjusts for family-wise error rate (FWER). For linear mixed-effects models

with individual animals as random effect, we used the MATLAB fitlme function with maximum likelihood estimation algorithm and Quasi-Newton optimization.

Author contributions

D.L. and C.M.R. conceived of the project, participated in its development, and wrote the manuscript. L.L. assisted with anatomy, histology and behavioral analysis. D.L. performed all imaging experiments and analyzed the data.

Acknowledgments

We thank members of Root lab for discussions, M. Aoi for discussions on data analysis, and T. Komiyama and for comments on the manuscript. This research was supported by grants from the NIH (R00DC014516, R01DC018313), and C.M.R. was a Hellman Fellow.

References

Allen WE, Chen MZ, Pichamoorthy N, Tien RH, Pachitariu M, Luo L, Deisseroth K. 2019. Thirst regulates motivated behavior through modulation of brainwide neural population dynamics. *Science* **364**:253.

Beier KT, Steinberg EE, DeLoach KE, Xie S, Miyamichi K, Schwarz L, Gao XJ, Kremer EJ, Malenka RC, Luo L. 2015. Circuit Architecture of VTA Dopamine Neurons Revealed by Systematic Input-Output Mapping. *Cell* **162**:622–634.

Beyeler A, Chang C-J, Silvestre M, Lévêque C, Namburi P, Wildes CP, Tye KM. 2018. Organization of Valence-Encoding and Projection-Defined Neurons in the Basolateral Amygdala. *Cell Rep* **22**:905–918.

Bolam JP, Ingham CA, Izzo PN, Levey AI, Rye DB, Smith AD, Wainer BH. 1986. Substance P-containing terminals in synaptic contact with cholinergic neurons in the neostriatum and basal forebrain: a double immunocytochemical study in the rat. *Brain Res* **397**:279–289.

Chu MW, Li WL, Komiyama T. 2016. Balancing the Robustness and Efficiency of Odor Representations during Learning. *Neuron* **92**:174–186.

Dan Y, Poo M-M. 2004. Spike timing-dependent plasticity of neural circuits. *Neuron* **44**:23–30.

Dobbs LK, Kaplan AR, Lemos JC, Matsui A, Rubinstein M, Alvarez VA. 2016. Dopamine Regulation of Lateral Inhibition between Striatal Neurons Gates the Stimulant Actions of Cocaine. *Neuron* **90**:1100–1113.

Faget L, Osakada F, Duan J, Ressler R, Johnson AB, Proudfoot JA, Yoo JH, Callaway EM, Hnasko TS. 2016. Afferent Inputs to Neurotransmitter-Defined Cell Types in the Ventral Tegmental Area. *Cell Rep* **15**:2796–2808.

Faget L, Zell V, Souter E, McPherson A, Ressler R, Gutierrez-Reed N, Yoo JH, Dulcis D, Hnasko TS. 2018. Opponent control of behavioral reinforcement by inhibitory and excitatory projections from the ventral pallidum. *Nat Commun* **9**:849.

Fink AJP, Axel R, Schoonover CE. 2019. A virtual burrow assay for head–fixed mice measures habituation, discrimination, exploration and avoidance without training. *Elife* **8**:e45658.

Fujimoto A, Hori Y, Nagai Y, Kikuchi E, Oyama K, Suhara T, Minamimoto T. 2019. Signaling

Incentive and Drive in the Primate Ventral Pallidum for Motivational Control of Goal-Directed Action. *J Neurosci* **39**:1793–1804.
Gadziola MA, Stetzik LA, Wright KN, Milton AJ, Arakawa K, Del Mar Cortijo M, Wesson DW. 2020. A Neural System that Represents the Association of Odors with Rewarded Outcomes and Promotes Behavioral Engagement. *Cell Rep* **32**:107919.
Gadziola MA, Tylicki KA, Christian DL, Wesson DW. 2015. The olfactory tubercle encodes odor valence in behaving mice. *J Neurosci* **35**:4515–4527.
Giovannucci A, Friedrich J, Gunn P, Kalfon J, Brown BL, Koay SA, Taxidis J, Najafi F, Gauthier JL, Zhou P, Khakh BS, Tank DW, Chklovskii DB, Pnevmatikakis EA. 2019. CaImAn an open source tool for scalable calcium imaging data analysis. *Elife* **8**. doi:10.7554/eLife.38173
Groenewegen HJ, Russchen FT. 1984. Organization of the efferent projections of the nucleus accumbens to pallidal, hypothalamic, and mesencephalic structures: a tracing and immunohistochemical study in the cat. *J Comp Neurol* **223**:347–367.
Gubner NR, Wilhelm CJ, Phillips TJ, Mitchell SH. 2010. Strain differences in behavioral inhibition in a Go/No-go task demonstrated using 15 inbred mouse strains. *Alcohol Clin Exp Res* **34**:1353–1362.
Haberly LB, Price JL. 1977. The axonal projection patterns of the mitral and tufted cells of the olfactory bulb in the rat. *Brain Res* **129**:152–157.
Hollerman JR, Schultz W. 1998. Dopamine neurons report an error in the temporal prediction of reward during learning. *Nat Neurosci* **1**:304–309.
Igarashi KM, Ieki N, An M, Yamaguchi Y, Nagayama S, Kobayakawa K, Kobayakawa R, Tanifuji M, Sakano H, Chen WR, Mori K. 2012. Parallel mitral and tufted cell pathways route distinct odor information to different targets in the olfactory cortex. *J Neurosci* **32**:7970–7985.
Ikemoto S. 2007. Dopamine reward circuitry: two projection systems from the ventral midbrain to the nucleus accumbens-olfactory tubercle complex. *Brain Res Rev* **56**:27–78.
Ikemoto S. 2003. Involvement of the olfactory tubercle in cocaine reward: intracranial self-administration studies. *J Neurosci* **23**:9305–9311.
In ’t Zandt EE, Cansler HL, Denson HB, Wesson DW. 2019. Centrifugal Innervation of the Olfactory Bulb: A Reappraisal. *eNeuro* **6**. doi:10.1523/ENEURO.0390-18.2019
Jackson J, Karnani MM, Zemelman BV, Burdakov D, Lee AK. 2018. Inhibitory Control of Prefrontal Cortex by the Claustrum. *Neuron* **99**:1029–1039.e4.
Jones DL, Mogenson GJ. 1980. Nucleus accumbens to globus pallidus GABA projection: electrophysiological and iontophoretic investigations. *Brain Res* **188**:93–105.
Kupchik YM, Brown RM, Heinsbroek JA, Lobo MK, Schwartz DJ, Kalivas PW. 2015. Coding the direct/indirect pathways by D1 and D2 receptors is not valid for accumbens projections. *Nat Neurosci* **18**:1230–1232.
Lederman J, Lardeux S, Nicola SM. 2021. Vigor Encoding in the Ventral Pallidum. *eNeuro* **8**. doi:10.1523/ENEURO.0064-21.2021
Litwin-Kumar A, Harris KD, Axel R, Sompolinsky H, Abbott LF. 2017. Optimal Degrees of Synaptic Connectivity. *Neuron* **93**:1153–1164.e7.
Martiros N, Kapoor V, Kim SE, Murthy VN. 2022. Distinct representation of cue-outcome association by D1 and D2 neurons in the ventral striatum’s olfactory tubercle. *Elife* **11**. doi:10.7554/eLife.75463
Mathis A, Mamidanna P, Cury KM, Abe T, Murthy VN, Mathis MW, Bethge M. 2018. DeepLabCut: markerless pose estimation of user-defined body parts with deep learning. *Nat Neurosci* **21**:1281–1289.
Millman DJ, Murthy VN. 2020. Rapid Learning of Odor–Value Association in the Olfactory

Striatum. *J Neurosci* **40**:4335–4347.
Murata K, Kinoshita T, Fukazawa Y, Kobayashi K, Yamanaka A, Hikida T, Manabe H, Yamaguchi M. 2019. Opposing Roles of Dopamine Receptor D1- and D2-Expressing Neurons in the Anteromedial Olfactory Tubercle in Acquisition of Place Preference in Mice. *Front Behav Neurosci* **13**:50.
Newman R, Winans SS. 1980. An experimental study of the ventral striatum of the golden hamster. II. Neuronal connections of the olfactory tubercle. *J Comp Neurol* **191**:193–212.
Oettl L-L, Scheller M, Filosa C, Wieland S, Haag F, Loeb C, Durstewitz D, Shusterman R, Russo E, Kelsch W. 2020. Phasic dopamine reinforces distinct striatal stimulus encoding in the olfactory tubercle driving dopaminergic reward prediction. *Nat Commun* **11**:3460.
Ottenheimer DJ, Bari BA, Sutlief E, Fraser KM, Kim TH, Richard JM, Cohen JY, Janak PH. 2020a. A quantitative reward prediction error signal in the ventral pallidum. *Nat Neurosci* **23**:1267–1276.
Ottenheimer DJ, Wang K, Tong X, Fraser KM, Richard JM, Janak PH. 2020b. Reward activity in ventral pallidum tracks satiety-sensitive preference and drives choice behavior. *Sci Adv* **6**. doi:10.1126/sciadv.abc9321
Ottenheimer D, Richard JM, Janak PH. 2018. Ventral pallidum encodes relative reward value earlier and more robustly than nucleus accumbens. *Nat Commun* **9**:4350.
Pnevmatikakis EA, Giovannucci A. 2017. NoRMCorre: An online algorithm for piecewise rigid motion correction of calcium imaging data. *J Neurosci Methods* **291**:83–94.
Pnevmatikakis EA, Soudry D, Gao Y, Machado TA, Merel J, Pfau D, Reardon T, Mu Y, Lacefield C, Yang W, Ahrens M, Bruno R, Jessell TM, Peterka DS, Yuste R, Paninski L. 2016. Simultaneous Denoising, Deconvolution, and Demixing of Calcium Imaging Data. *Neuron* **89**:285–299.
Recanatesi S, Ocker GK, Buice MA, Shea-Brown E. 2019. Dimensionality in recurrent spiking networks: Global trends in activity and local origins in connectivity. *PLoS Comput Biol* **15**:e1006446.
Rescorla RA. 1972. A theory of Pavlovian conditioning : Variations in the effectiveness of reinforcement and non-reinforcement. *Classical conditioning, Current research and theory* **2**:64–69.
Ricardo JA. 1980. Efferent connections of the subthalamic region in the rat. I. The subthalamic nucleus of Luys. *Brain Res* **202**:257–271.
Richard JM, Ambroggi F, Janak PH, Fields HL. 2016. Ventral Pallidum Neurons Encode Incentive Value and Promote Cue-Elicited Instrumental Actions. *Neuron* **90**:1165–1173.
Schultz W, Dayan P, Montague PR. 1997. A neural substrate of prediction and reward. *Science* **275**:1593–1599.
Scott JW. 1981. Electrophysiological identification of mitral and tufted cells and distributions of their axons in olfactory system of the rat. *J Neurophysiol* **46**:918–931.
Shannon CE. 1948. A mathematical theory of communication. *The Bell System Technical Journal* **27**:379–423.
Smith KS, Tindell AJ, Aldridge JW, Berridge KC. 2009. Ventral pallidum roles in reward and motivation. *Behav Brain Res* **196**:155–167.
Soares-Cunha C, de Vasconcelos NAP, Coimbra B, Domingues AV, Silva JM, Loureiro-Campos E, Gaspar R, Sotiropoulos I, Sousa N, Rodrigues AJ. 2020. Nucleus accumbens medium spiny neurons subtypes signal both reward and aversion. *Mol Psychiatry* **25**:3241–3255.
Stephenson-Jones M, Bravo-Rivera C, Ahrens S, Furlan A, Xiao X, Fernandes-Henriques C, Li B. 2020. Opposing Contributions of GABAergic and Glutamatergic Ventral Pallidal Neurons to Motivational Behaviors. *Neuron* **105**:921–933.e5.

1007 Sutton RS. 1988. Learning to predict by the methods of temporal differences. *Mach Learn* **3**:9–
1008 44.
1009 Tachibana Y, Hikosaka O. 2012. The primate ventral pallidum encodes expected reward value
1010 and regulates motor action. *Neuron* **76**:826–837.
1011 Tindell AJ, Smith KS, Berridge KC, Aldridge JW. 2005. VP neurons integrate learning and
1012 physiological signals to code incentive salience of conditioned cues. *Soc Neurosci Abstr*.
1013 Tindell AJ, Smith KS, Peciña S, Berridge KC, Aldridge JW. 2006. Ventral pallidum firing codes
1014 hedonic reward: when a bad taste turns good. *J Neurophysiol* **96**:2399–2409.
1015 Tritsch NX, Sabatini BL. 2012. Dopaminergic modulation of synaptic transmission in cortex and
1016 striatum. *Neuron* **76**:33–50.
1017 Turner MS, Lavin A, Grace AA, Napier TC. 2001. Regulation of limbic information outflow by the
1018 subthalamic nucleus: excitatory amino acid projections to the ventral pallidum. *J Neurosci*
1019 **21**:2820–2832.
1020 Wang PY, Boboila C, Chin M, Higashi-Howard A, Shamash P, Wu Z, Stein NP, Abbott LF, Axel
1021 R. 2020. Transient and Persistent Representations of Odor Value in Prefrontal Cortex.
1022 *Neuron* **108**:209–224.e6.
1023 Watabe-Uchida M, Zhu L, Ogawa SK, Vamanrao A, Uchida N. 2012. Whole-brain mapping of
1024 direct inputs to midbrain dopamine neurons. *Neuron* **74**:858–873.
1025 Wesson DW. 2020. The Tubular Striatum. *J Neurosci* **40**:7379–7386.
1026 Wesson DW, Wilson DA. 2010. Smelling Sounds: Olfactory–Auditory Sensory Convergence in
1027 the Olfactory Tubercle. *J Neurosci* **30**:3013–3021.
1028 Wieland S, Schindler S, Huber C, Köhr G, Oswald MJ, Kelsch W. 2015. Phasic Dopamine
1029 Modifies Sensory-Driven Output of Striatal Neurons through Synaptic Plasticity. *J Neurosci*
1030 **35**:9946–9956.
1031 Zahm DS, Heimer L. 1987. The ventral striatopallidothalamic projection. III. Striatal cells of the
1032 olfactory tubercle establish direct synaptic contact with ventral pallidal cells projecting to
1033 mediodorsal thalamus. *Brain Res* **404**:327–331.
1034 Zhang Z, Liu Q, Wen P, Zhang J, Rao X, Zhou Z, Zhang H, He X, Li J, Zhou Z, Xu X, Zhang X,
1035 Luo R, Lv G, Li H, Cao P, Wang L, Xu F. 2017a. Activation of the dopaminergic pathway
1036 from VTA to the medial olfactory tubercle generates odor-preference and reward. *Elife* **6**.
1037 doi:10.7554/eLife.25423
1038 Zhang Z, Zhang H, Wen P, Zhu X, Wang L, Liu Q, Wang J, He X, Wang H, Xu F. 2017b. Whole-
1039 Brain Mapping of the Inputs and Outputs of the Medial Part of the Olfactory Tubercle. *Front*
1040 *Neural Circuits* **11**:52.
1041 Zhou L, Furuta T, Kaneko T. 2003. Chemical organization of projection neurons in the rat
1042 accumbens nucleus and olfactory tubercle. *Neuroscience* **120**:783–798.

Figure 1:

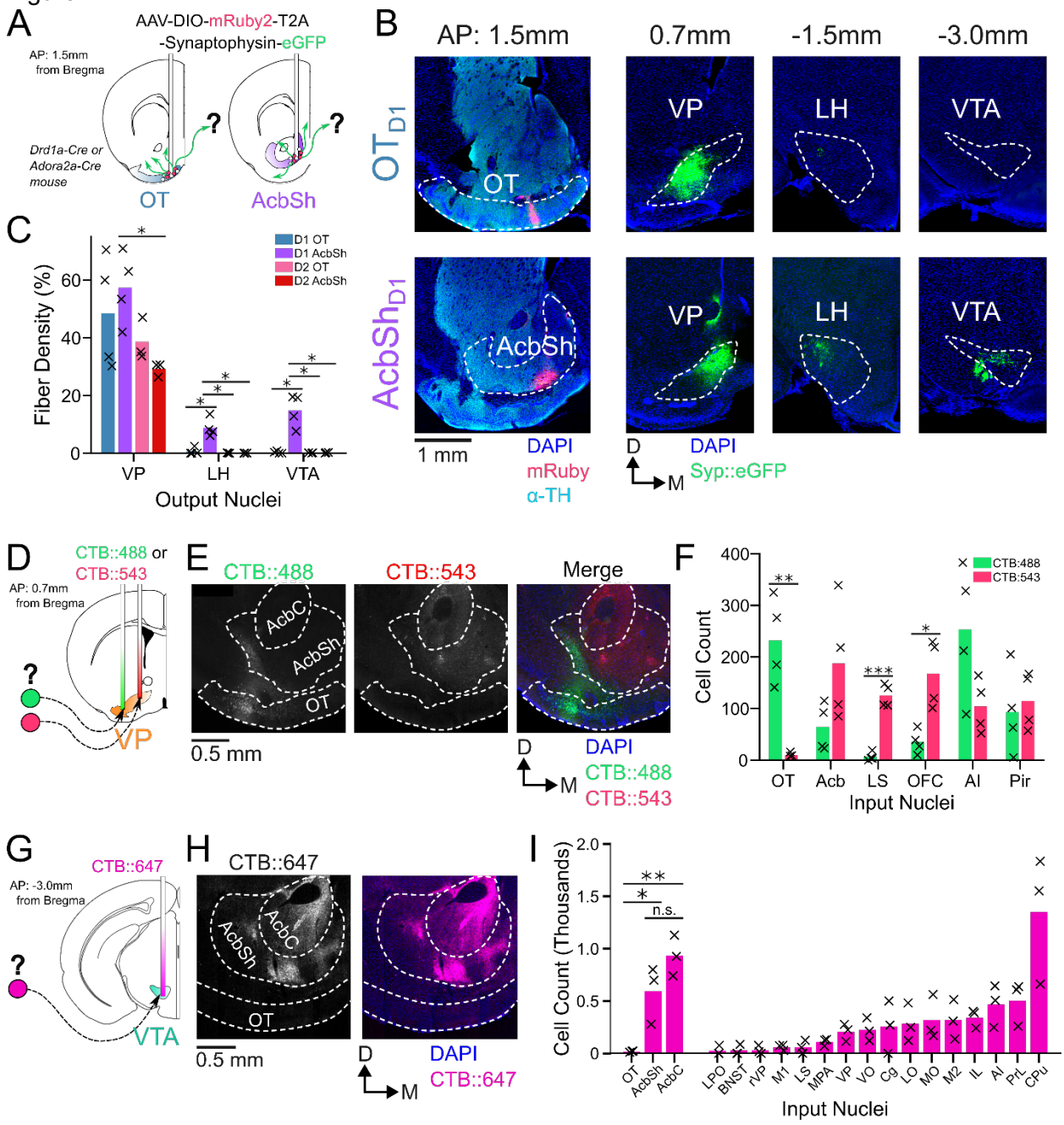
A
AAV-DIO-mRuby2-T2A
-Synaptophysin-eGFP
AP: 1.5mm
from Bregma
Drd1a-Cre or
Adora2a-Cre
mouse
OT
AcbSh
B
AP: 1.5mm
0.7mm
-1.5mm
-3.0mm
OT D1
AcbSh D1
OT
VP
LH
VTA
AcbSh
1 mm
DAPI
mRuby
α-TH
D
M
DAPI
Syp::eGFP
C
Fiber Density (%)
D1 OT
D1 AcbSh
D2 OT
D2 AcbSh
VP
LH
VTA
Output Nuclei
D
CTB::488 or
CTB::543
AP: 0.7mm
from Bregma
VP
E
CTB::488
CTB::543
Merge
AcbC
AcbSh
OT
0.5 mm
D
M
DAPI
CTB::488
CTB::543
F
Cell Count
CTB:488
CTB:543
OT
Acb
LS
OFC
AI
Pir
Input Nuclei
G
CTB::647
AP: -3.0mm
from Bregma
VTA
H
CTB::647
AcbSh
AcbC
OT
0.5 mm
D
M
DAPI
CTB::647
I
Cell Count (Thousands)
n.s.
OT
AcbSh
AcbC
LPO
BNST
rVP
M1
LS
MPA
VP
VO
Cg
LO
MO
M2
IL
AI
PrL
CPu
Input Nuclei

Figure 1. OT_{D1} and OT_{D2} primarily project to the lateral portion of the VP. (**A**) Schematic representation of Cre-dependent anterograde axonal AAV tracing experiments used to characterize outputs of OT neurons. *Drd1*+ and *Drd2*+ neurons were separately labeled by using *Drd1*-Cre and *Adora2a*-Cre mouse lines, respectively. (**B**) Representative images from OT_{D1} (top) vs. the $AcbSh_{D1}$ injection (bot). Target sites (far-left column) are stained with α-tyrosine hydroxylase antibodies to visualize the boundary between VP and OT. (**C**) Quantifying the % of output regions with fluorescence (n=3-4). (**D**) Schematic representation of 2-color retrograde CTB tracing experiment used to confirm OT to VP connectivity. CTB::488 and CTB::543 were injected to the lateral and medial portion of the VP, respectively. (**E**) Representative images of CTB labeled neurons in the OT and Acb. (**F**) The number of labeled cells was quantified (n=4). (**G**) Schematic representation of retrograde CTB tracing experiment used to test OT to VTA connectivity. CTB::647 was injected in the VTA. (**H**) Representative image shows robust AcbSh and AcbC labeling but no OT labeling. (**I**) Quantification of labeling in different nuclei (n=3). Pairwise comparisons were done using the Student's t-test. The p-values were corrected for FDR by Benjamini-Hocherg procedure. ***$p<0.001$, **$p<0.01$, *$p<0.05$. See Tables S1-S3 for detailed statistics.

Figure 2:

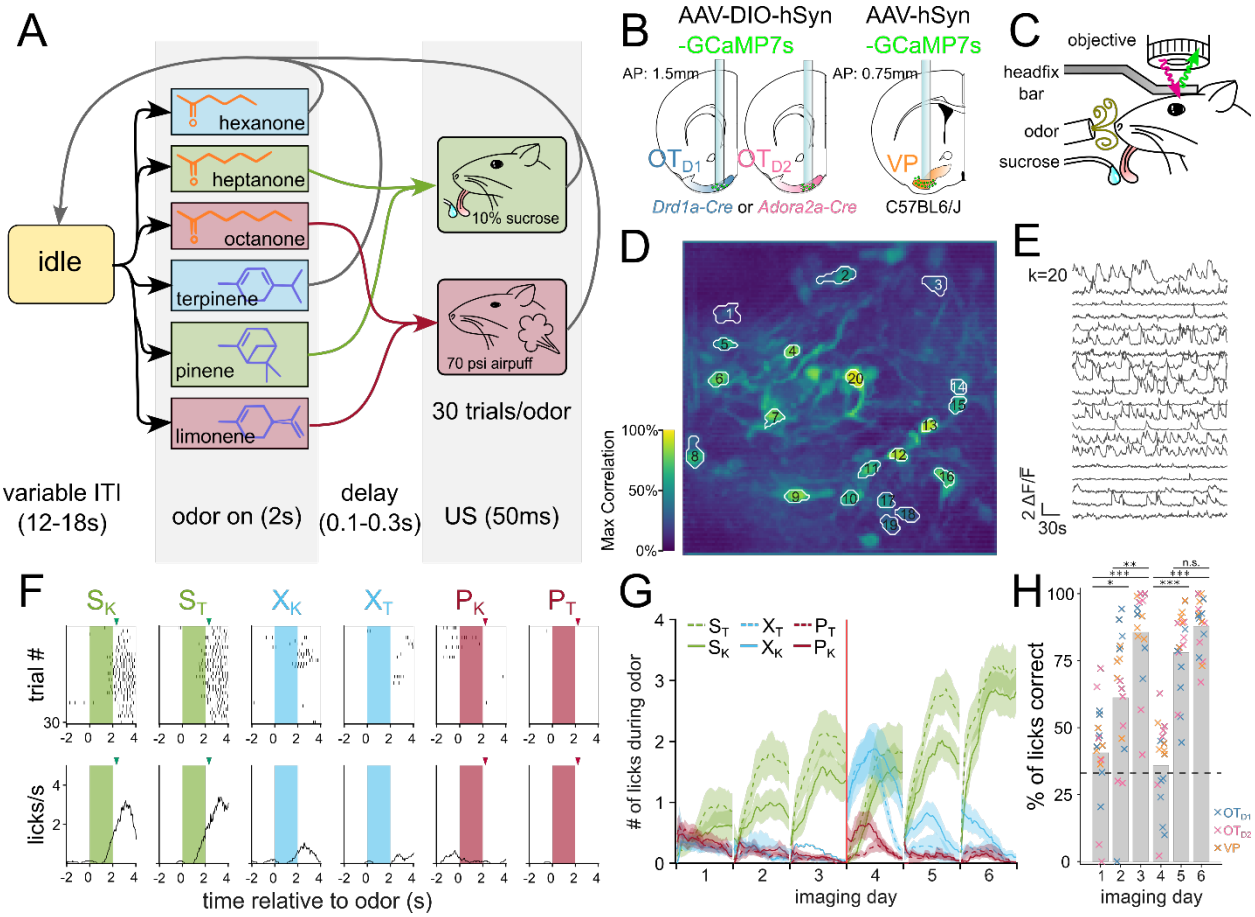
A
hexanone
heptanone
octanone
terpinene
pinene
limonene
idle
10% sucrose
70 psi airpuff
30 trials/odor
variable ITI
(12-18s)
odor on (2s)
delay
(0.1-0.3s)
US (50ms)
B
AAV-DIO-hSyn
-GCaMP7s
AAV-hSyn
-GCaMP7s
AP: 1.5mm
AP: 0.75mm
OTD1
OTD2
VP
Drd1a-Cre or Adora2a-Cre
C57BL6/J
C
objective
headfix
bar
odor
sucrose
D
Max Correlation
100%
50%
0%
E
k=20
2 ΔF/F
30s
F
SK
ST
XK
XT
PK
PT
trial #
licks/s
time relative to odor (s)
G
# of licks during odor
imaging day
H
% of licks correct
imaging day
n.s.

Figure 2. Head-fixed 2-photon Ca^{2+} imaging of OT_{D1}, OT_{D2}, or VP neurons during 6-odor conditioning paradigm. (**A**) State-diagram of odor conditioning paradigm. Each trial begins with 2 seconds of odor delivery. Odors are chosen in pseudorandomized order such that the same odor is not repeated more than twice in a row. At the end of odor delivery, there is a variable delay (100-300ms), after which the animal is given either a 10% sucrose solution (S_K and S_T), a 70 psi airpuff (P_K and P_T), or nothing (X_K and X_T). Trials are separated by a variable intertrial interval (ITI; 12-18s). Schematic representation of (**B**) lens implant surgery and (**C**) headfix 2-photon microscopy setup. An example of spatial (**D**) and temporal (**E**) components extracted by CNMF from *Drd1*-Cre animal on day 3 of imaging. (**D**) The spatial footprints of 20 example neurons are shown on top of a maximum-correlation pixel image that was used to seed the factorization. The number displayed over each neuron matches the row number of the temporal components in (**E**). (**F**) An example raster plot (top) and averaged-across-trials trace (bottom) of the licking behavior recorded concurrently as (**D**) and (**E**). The timing of odor delivery is shown as shaded rectangles. The timing of US delivery is shown as arrowheads. (**G**) The mean total licks during each of the odors is shown averaged across all animals (n=17) after application of a moving-average filter with a window size of 10 trials. Red line marks the sucrose and airpuff contingency switch between day 3 and day 4. (**H**) Bar graph showing the licks during either sucrose cue expressed as a fraction of all licks during any odor. FWER-adjusted statistical significance for post hoc comparisons are shown as: ***$p<0.001$, **$p<0.01$, *$p<0.05$. See Tables S4-5 for detailed statistics.

Figure 3:

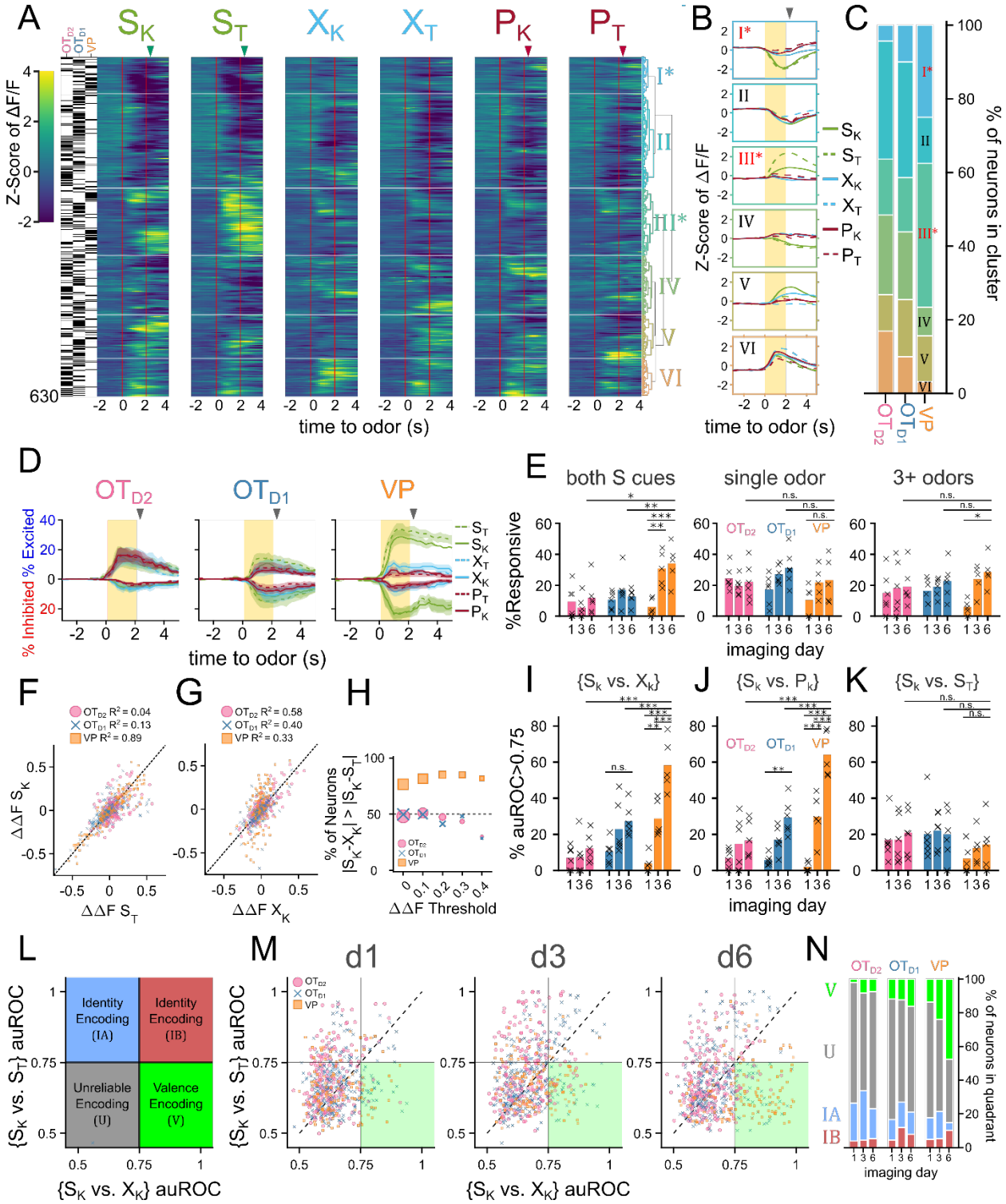
A
B
C
D
E
F
G
H
I
J
K
L
M
N
Z-Score of ΔF/F
time to odor (s)
% of neurons in cluster
% Inhibited % Excited
%Responsive
imaging day
both S cues
single odor
3+ odors
ΔΔF S_K
ΔΔF S_T
ΔΔF X_K
% of Neurons
ΔΔF Threshold
% auROC>0.75
{S_K vs. X_K}
{S_K vs. P_K}
{S_K vs. S_T}
Identity Encoding (IA)
Identity Encoding (IB)
Unreliable Encoding (U)
Valence Encoding (V)
{S_K vs. S_T} auROC
{S_K vs. X_K} auROC
d1
d3
d6
% of neurons in quadrant

Figure 3. VP neurons encode reward-contingency more robustly than OT_{D1} or OT_{D2} neurons. (**A**) Heatmap of odor-evoked activities in OT_{D1}, OT_{D2}, and VP neurons from day 6 of imaging. The fluorescence measurements from each neuron were averaged over trials, Z-scored, then pooled for hierarchical clustering. Neurons are grouped by similarity, with the dendrogram shown on the right and a raster plot on the left indicating which region a given neuron is from. Horizontal white lines demarcate the boundaries between the 6 clusters. Odor delivered at 0-2 seconds marked by vertical red lines and US delivery is marked by arrowheads. From left to right, the columns represent neural responses to sucrose-paired ketone and terpene, control ketone and terpene, and airpuff-paired ketone and terpene (S_K, S_T, X_K, X_T, P_K, P_T). (**B**) Average Z-scored activity of each cluster to each of the 6 odors on day 6 of imaging. Yellow bar indicates 2-seconds of odor exposure. (**C**) The distribution of clusters by population. (**D**) Percentage of total neurons that were significantly excited or inhibited by each odor (Bonferroni-adjusted FDR < 0.05) as a function of time relative to odor. Lines represent the mean across biological replicates and the shaded area reflects the mean ± SEM. (**E**) Bar graph showing % of neurons from each population that are responsive to both sucrose-paired odors in the same direction (left), responsive to only a single odor (middle), or responsive to at least 3 odors (right). Bars represent the mean across biological replicates and x's mark individual animals. (**F**) Scatterplot comparing the magnitudes of S_K responses ($\Delta\Delta S_K$) to S_T responses ($\Delta\Delta S_T$). The dotted line represents the hypothetical scenario where $\Delta\Delta S_K = \Delta\Delta S_T$. For each population, the R^2 value of the 2-d distribution compared to the $\Delta\Delta S_K = \Delta\Delta S_T$ line is reported. (**G**) Same as F but comparing $\Delta\Delta S_K$ to $\Delta\Delta X_K$. (**H**) Lineplot showing the % of neurons from each population where the difference between $\Delta\Delta S_K$ and $\Delta\Delta X_K$ is lower than that between $\Delta\Delta S_K$ and $\Delta\Delta S_T$. (**I**) Bargraph showing % of neurons whose responses to {S_K vs. X_K} can be discriminated by a linear classifier with auROC>0.75. (**J**) Same as (I) but for {S_K vs P_K}. (**K**) Same as (I) but for {S_K vs S_T}. (**L**) Schematic representation of 4 possible categories for a joint-distribution of {S_K vs. X_K} and {S_K vs. S_T} auROC values. Identity-encoding neurons could be in any quadrant other than the bottom-left whereas valence-encoding neurons should be in the bottom-right quadrant. (**M**) Scatterplot of each neuron's auROC value for {S_K vs. X_K} on the x-axis and {S_K vs. S_T} on the y-axis on days 1, 3 and 6 of imaging. (**N**) Stacked bar graph showing the distribution of neurons from each population that fall into each of the 4 quadrants across the 3 different imaging days. FWER-adjusted statistical significance for post hoc comparisons are shown as: ***p<0.001, **p<0.01, *p<0.05, n.s. p>0.05. See Tables S6-17 for detailed statistics.

Figure 4:

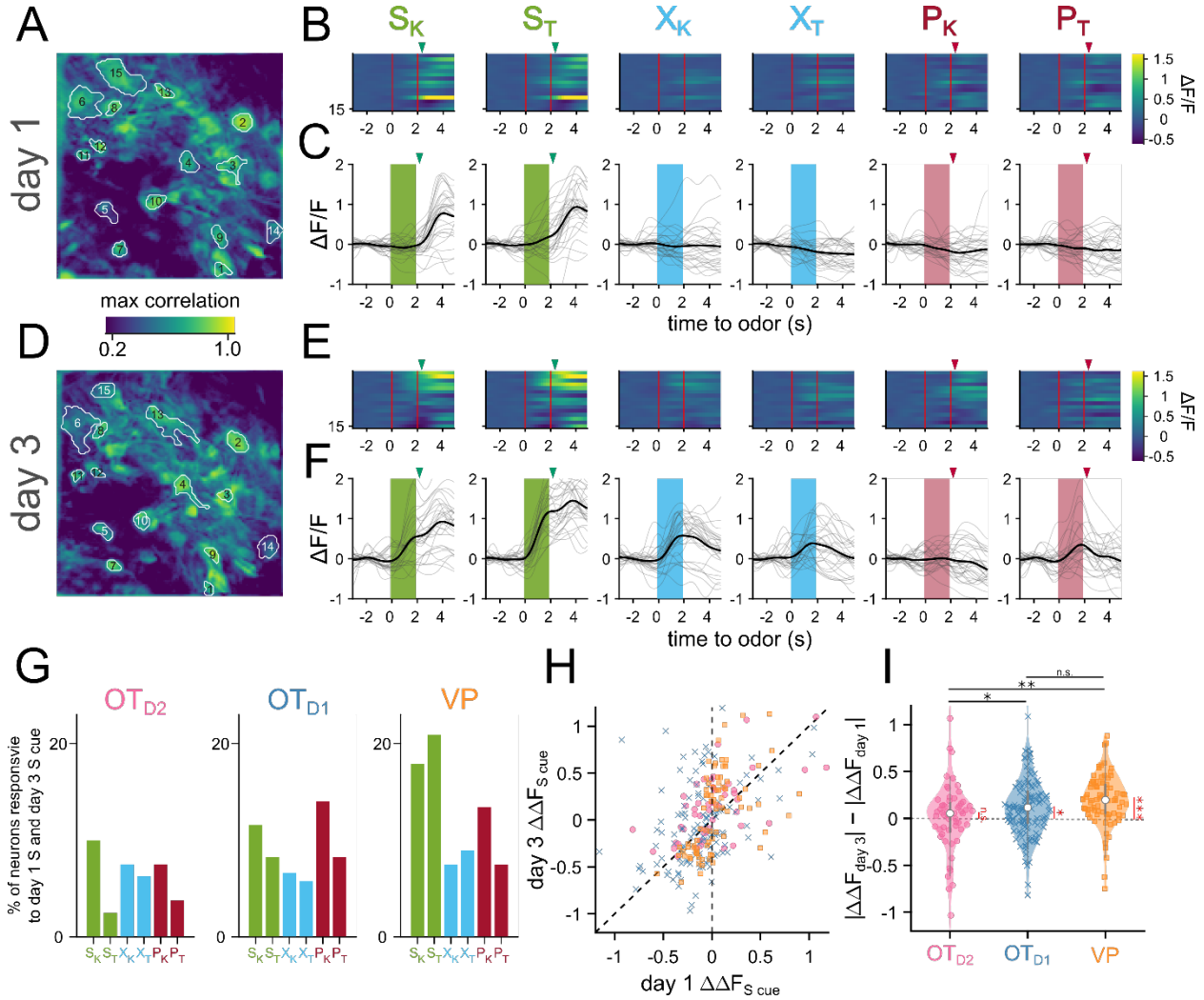
A
day 1
max correlation
0.2
1.0
B
C
D
day 3
E
F
ΔF/F
time to odor (s)
G
OT$_{D2}$
OT$_{D1}$
VP
% of neurons responsvie to day 1 S and day 3 S cue
H
day 3 ΔΔF$_{S\ cue}$
day 1 ΔΔF$_{S\ cue}$
I
|ΔΔF$_{day\ 3}$| − |ΔΔF$_{day\ 1}$|
n.s.

Figure 4. Sucrose responsive VP neurons become sucrose-cue responsive after pairing. (**A**) The spatial footprints of 15 neurons from day 1 are outlined over a max-correlation projection image. (**B**) Heatmap of averaged-over-trials ΔF/F in response to 6 odors on day 1. Odor delivery period is shown with 2 red vertical lines and sucrose/airpuff timing is shown with downward arrowhead. (**C**) An example neuron's responses on day 1 across 30 trials to 6 different odors. Individual trial traces are shown in light gray whereas the averaged-across trials trace is shown in black. Odor delivery period is depicted as shaded rectangles and US delivery is marked by arrowheads. (**D-F**) Same as (**A-C**), respectively, but for day 3. (**G**) Percentage of all tracked neurons that were both sucrose-responsive on day 1 and odor-responsive in the same direction on day 3. (**H**) Scatter plot of averaged-over-trials responses to S_K or S_T on day 1 (x-axis) and day 3 (y-axis). Each point is a neuron that was successfully matched from day 1 and day 3. Neurons from OT_{D2}, OT_{D1}, and VP are plotted as pink circles, blue crosses, and yellow squares, respectively. Neurons that have increased response magnitudes on day 3 would fall between the 2 dotted lines. (**I**) Violin plot showing the distributions of day 3 responsive magnitude – day 1 response magnitude. Black asterisks show statistical significance of pairwise comparisons and red asterisks show statistical significance for one-sample t-tests. Pairwise comparisons were done using the Student's t-test. The p-values were corrected for FDR by Benjamini-Hocherg procedure. ***$p<0.001$, **$p<0.01$, *$p<0.05$, n.s. $p>0.05$. See Tables S18-19 for detailed statistics.

Figure 5:

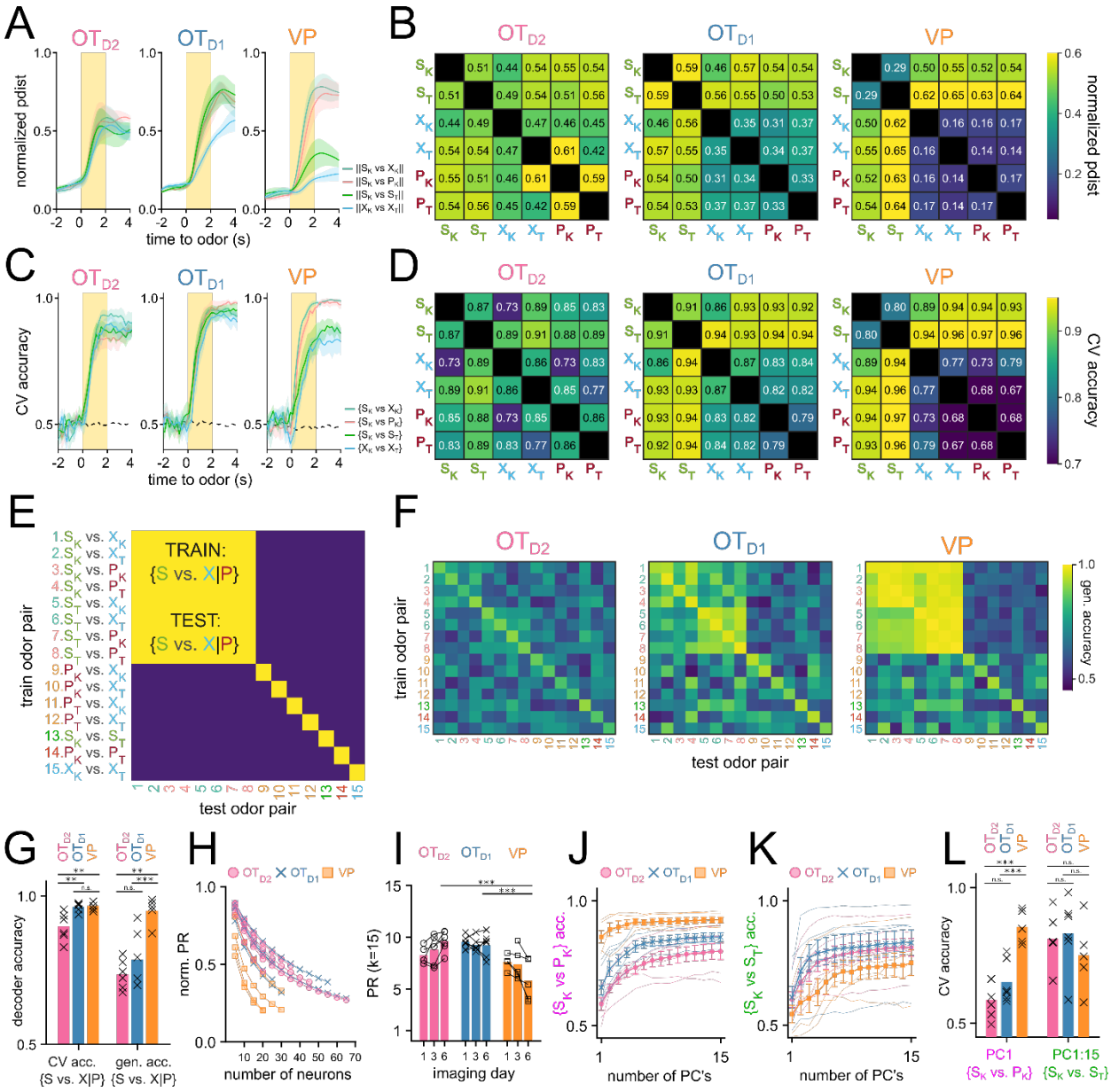
A
B
C
D
E
F
G
H
I
J
K
L
OT_D2
OT_D1
VP
normalized pdist
time to odor (s)
CV accuracy
normalized pdist
TRAIN:
{S vs. X|P}
TEST:
{S vs. X|P}
train odor pair
test odor pair
gen. accuracy
decoder accuracy
CV acc.
{S vs. X|P}
gen. acc.
{S vs. X|P}
norm. PR
number of neurons
PR (k=15)
imaging day
number of PC's
CV accuracy
PC1
PC1:15

Figure 5. OT encodes odor identity in high-dimensional space and VP encodes reward-contingency in low-dimensional space. (**A**) Average normalized pairwise Euclidean distance between odor-evoked population-level activity from day 6 of imaging shown as a function of time relative to odor delivery. Traces show the average value across biological replicates of the same population and the shaded areas represent the average ± SEM. (**B**) A heatmap of the average normalized pairwise distance during the odor delivery period. (**C**) Average CV accuracy of binary pairwise linear classifiers trained on population data plotted against time relative to odor delivery. (**D**). A heatmap of the average CV accuracy during the odor delivery period. (**E**) Schematic representation of generalized linear classification performance for an idealized valence encoder. Each row corresponds to the training odor-pair and each column corresponds to the testing odor-pair. For an idealized valence encoder, the decodability would generalize well across odor-pairs of the equal valence grouping outlined in red. Note that the elements along the diagonal are cases where training and testing odor-pairs are identical and do not reflect generalizability. (**F**) Heatmap representing the maximum generalized linear classification accuracy during odor delivery period averaged across biological replicates for each population. (**G**) Mean cross-validated linear classifier accuracy for S-cue vs. control or puff-cue classification and the generalized accuracy for S-cue vs. control or puff-cue classification after training on a different pair. Bar represents the mean across biological replicates and x's mark accuracy values for individual animals. (**H**) Average PR normalized to *n* calculated after randomly subsampling an increasing number of neurons. (**I**) Average PR calculated after subsampling 15 neurons. (**J**) Average CV accuracy of linear classifiers trained on $\{S_K$ vs. $P_K\}$ plotted against number of principal components used for training. For each simultaneously imaged group of neurons, 15 neurons were subsampled and classifiers were trained on an increasing number of principal components. Thinner faded lines show mean accuracy across subsampling for individual animals. Markers represent the mean across biological replicates. Error bars indicate SEM across biological replicates. (**K**) Average CV accuracy of linear classifiers trained on $\{S_K$ vs. $S_T\}$. (**L**) Comparison of the average accuracy of $\{S_K$ vs. $P_K\}$ classifiers trained on the 1st PC vs. $\{S_K$ vs. $S_T\}$ classifiers trained on all 15 PC's. FWER-adjusted statistical significance for post hoc comparisons are shown as: ***$p<0.001$, **$p<0.01$, *$p<0.05$, n.s. $p>0.05$. See Tables S20-29 for detailed statistics.

Figure 6:

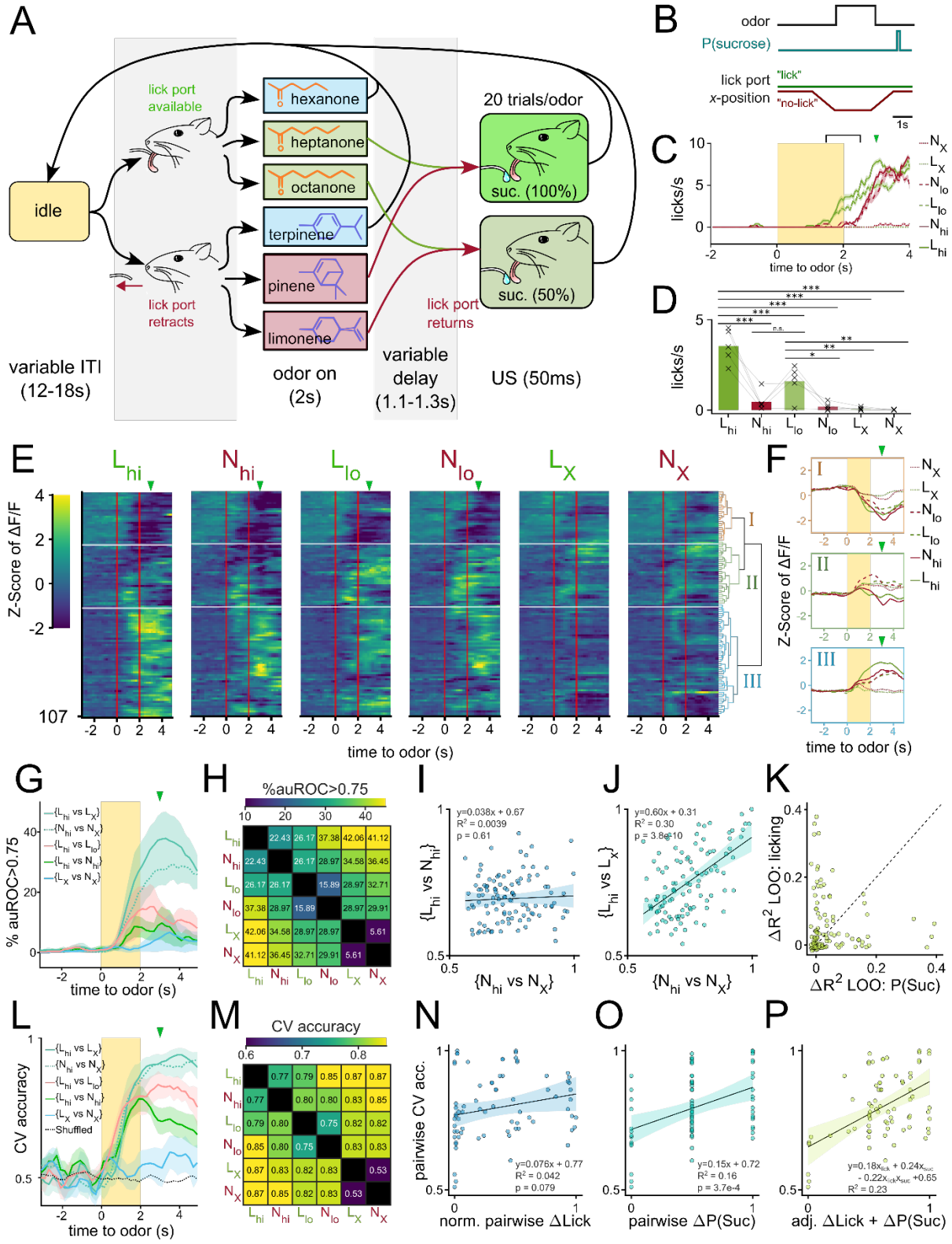
A
idle
lick port available
lick port retracts
hexanone
heptanone
octanone
terpinene
pinene
limonene
20 trials/odor
suc. (100%)
suc. (50%)
lick port returns
variable ITI (12-18s)
odor on (2s)
variable delay (1.1-1.3s)
US (50ms)
B
odor
P(sucrose)
lick port x-position
"lick"
"no-lick"
1s
C
licks/s
time to odor (s)
D
licks/s
E
Z-Score of ΔF/F
time to odor (s)
F
Z-Score of ΔF/F
time to odor (s)
G
% auROC>0.75
time to odor (s)
H
%auROC>0.75
I
y=0.038x + 0.67
R² = 0.0039
p = 0.61
J
y=0.60x + 0.31
R² = 0.30
p = 3.8e-10
K
ΔR² LOO: licking
ΔR² LOO: P(Suc)
L
CV accuracy
time to odor (s)
M
CV accuracy
N
pairwise CV acc.
y=0.076x + 0.77
R² = 0.042
p = 0.079
norm. pairwise ΔLick
O
y=0.15x + 0.72
R² = 0.16
p = 3.7e-4
pairwise ΔP(Suc)
P
y=0.18x_lick + 0.24x_suc - 0.22x_lick x_suc +0.65
R² = 0.23
adj. ΔLick + ΔP(Suc)

Figure 6. Separate VP populations encode reward-contingency and licking vigor. (**A**) State diagram for odor pairing paradigm where lick spout is removed during the presentation of half of the odors. The paradigm is similar to one described in Fig2A with the following key differences: 1) the lick spout is moved away from the animal's mouth during the presentation of half of the odors (N_{hi}, N_{lo}, N_X). 2) sucrose is delivered after a longer variable delay (1.1-1.3s). 3) 2 of the odors have 100% sucrose contingency (L_{hi}, N_{hi}), 2 of the odors have 50% sucrose contingency (L_{lo}, N_{lo}), and the other 2 have 0% sucrose contingency (L_X, N_X). (**B**) Schematic showing the timing of lick port movement relative to odor and sucrose delivery. (**C**) Licking behavior to 6 odors averaged across 30 trials from a representative animal. Duration of odor delivery is marked by the shaded rectangle and the average time of sucrose delivery is marked by the arrowhead. The time bin used for subsequent analysis (last 0.5s of odor and first 0.5s of delay) is outlined by square brackets (**D**) Average licks/s for each odor measured between the last 0.5s of odor and the first 0.5s of delay. Data were pooled from the day of highest difference between licks to L_{hi} and N_{hi}. (**E**) Heatmap of odor-evoked activity in VP neurons pooled from each animal's day of highest difference between licks to L_{hi} and N_{hi}. Neurons are grouped according to the clustering dendrogram, shown on the right. Horizontal white lines demarcate the boundaries between the 3 clusters. Odor delivery is marked by vertical red lines. (**F**) Average Z-scored activity of each cluster to each of the 6 odors. Yellow bar indicates 2-seconds of odor exposure. (**G**) The percentage of single-neuron linear classifiers with auROC>0.75 as a function of time relative to odor delivery. Shaded area represents the SEM across biological replicates (n=5). (**H**) Heatmap of the percentage of pooled VP neurons with auROC>0.75 during the last 0.5s of odor and first 0.5s of delay. (**I**) Scatterplot comparing the auROC for {L_{hi} vs N_{hi}} (y-axis) and {N_{hi} vs. N_X} (x-axis) for each neuron. The line of best fit is plotted as a dotted line, with the 95% confidence interval shaded in. (**J**) Same as (I) but comparing the auROC for {L_{hi} vs L_X} (y-axis) and {N_{hi} vs. N_X} (x-axis). (**K**) Scatterplot comparing regression models that explain each neuron's activity on a given trial as a function of anticipatory licking or sucrose contingency. The values plotted are the loss in R^2 in models without anticipatory licking (y-axis) or sucrose contingency (x-axis) when compared to a model with both variables and their interaction term. (**L**) CV accuracy for 5 different odor pairs as a function of time relative to odor delivery. (**M**) Heatmap of average pairwise CV accuracy trained on the last 0.5s of odor and the first 0.5s of delay. (**N**) Scatterplot of all pairwise classifier accuracies from all animals (y-axis) and the corresponding range-normalized average pairwise difference in anticipatory licking (x-axis). (**O**) Scatterplot of all pairwise classifier accuracies from all animals (y-axis) and the corresponding pairwise difference in reward-contingency (x-axis). (**P**) Scatterplot of all pairwise classifier accuracies (y-axis) and the adjusted combined model of ranged-normalized Δlick and Δreward-contingency (x-axis). FWER-adjusted statistical significance for post hoc comparisons are shown as: ***$p<0.001$, **$p<0.01$, *$p<0.05$, n.s. $p>0.05$. See Tables S30-31 for detailed statistics.

Figure S1:

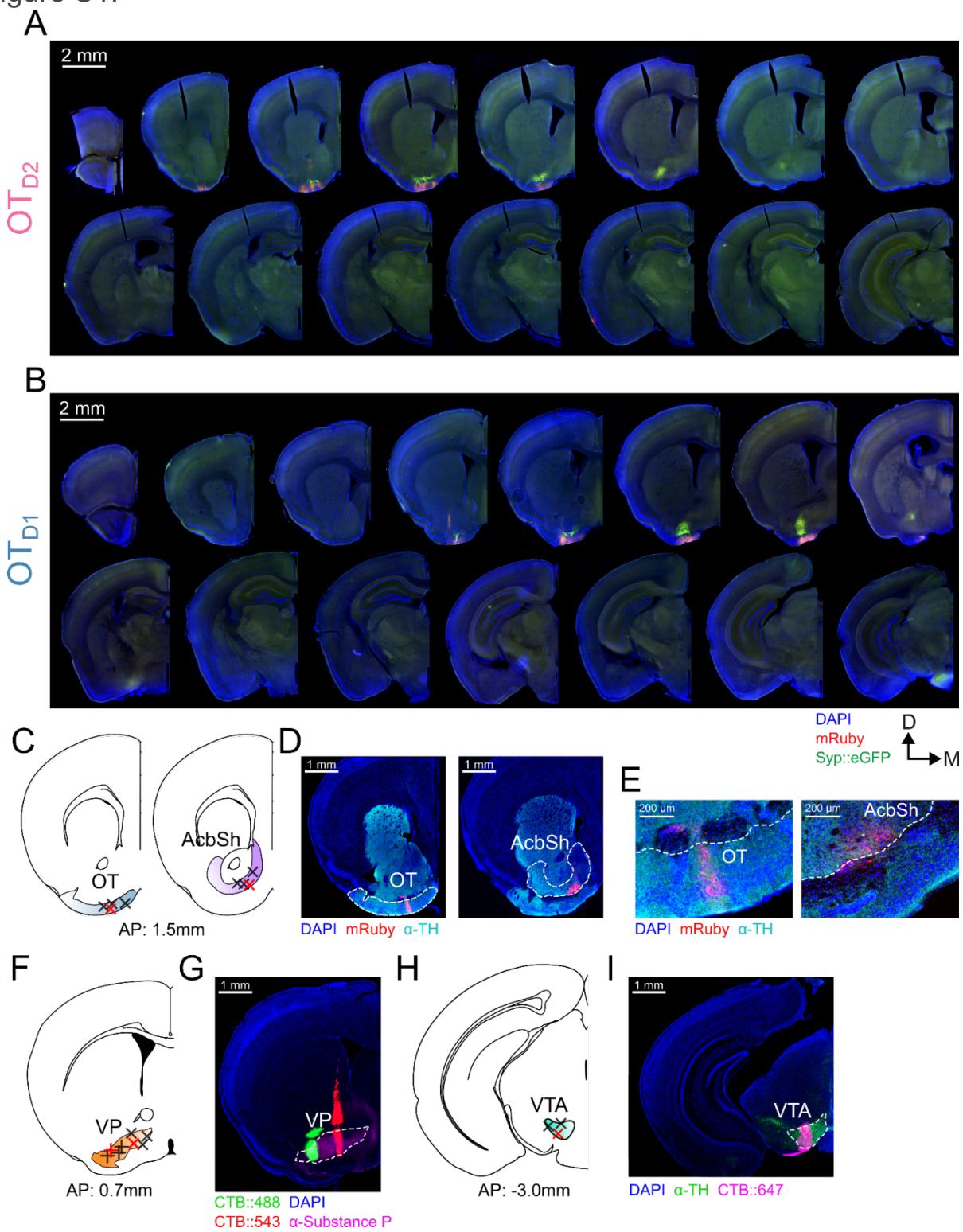
A
2 mm
OT$_{D2}$
B
2 mm
OT$_{D1}$
C
OT
AcbSh
AP: 1.5mm
D
1 mm
OT
1 mm
AcbSh
DAPI mRuby α-TH
DAPI
mRuby
Syp::eGFP
D
M
E
200 µm
OT
200 µm
AcbSh
DAPI mRuby α-TH
F
VP
AP: 0.7mm
G
1 mm
VP
CTB::488 DAPI
CTB::543 α-Substance P
H
VTA
AP: -3.0mm
I
1 mm
VTA
DAPI α-TH CTB::647

Figure S1. OT_{D1} and OT_{D2} primarily project to the lateral portion of the VP.
(**A**) Serial coronal sections from a representative experiment where AAVDJ-hSyn-FLEX-mRuby-T2A-syn-eGFP virus was injected into the anterior OT of an *Adora2a*-Cre mouse. Sections are roughly 400µm apart from each other and range from +2.5mm to -3.0mm relative to bregma. (**B**) Same as (A) but in a *Drd1*-Cre mouse. (**C**) Schematic showing the centroids of 4 injection sites for OT and AcbSh anterograde tracing experiments. (**D**, **E**) Representative images of the injection sites shown in (C). Sections were counterstained with α-TH to delineate the boundary between the striatum and the rostral ventral pallidum. The centroids of these samples are marked as red x's in (C). (**F**) Schematic showing the centroids of 4 CTB injection sites for lateral and medial VP. CTB::488 injection to the lateral VP are marked by +'s whereas CTB::543 injection to the medial VP are marked by x's. (**G**) Representative image of the injection sites shown in (F). Sections were counterstained with α-Substance P to mark the boundary of the VP. The centroids of this sample are marked by the red + and red x in (F). (**H**) Schematic showing the centroids of 3 CTB injection sites for VTA. (**I**) Representative image of the injection sites shown in (H). Sections were counterstained with α-TH to mark the boundary of the VTA.

Figure S2:

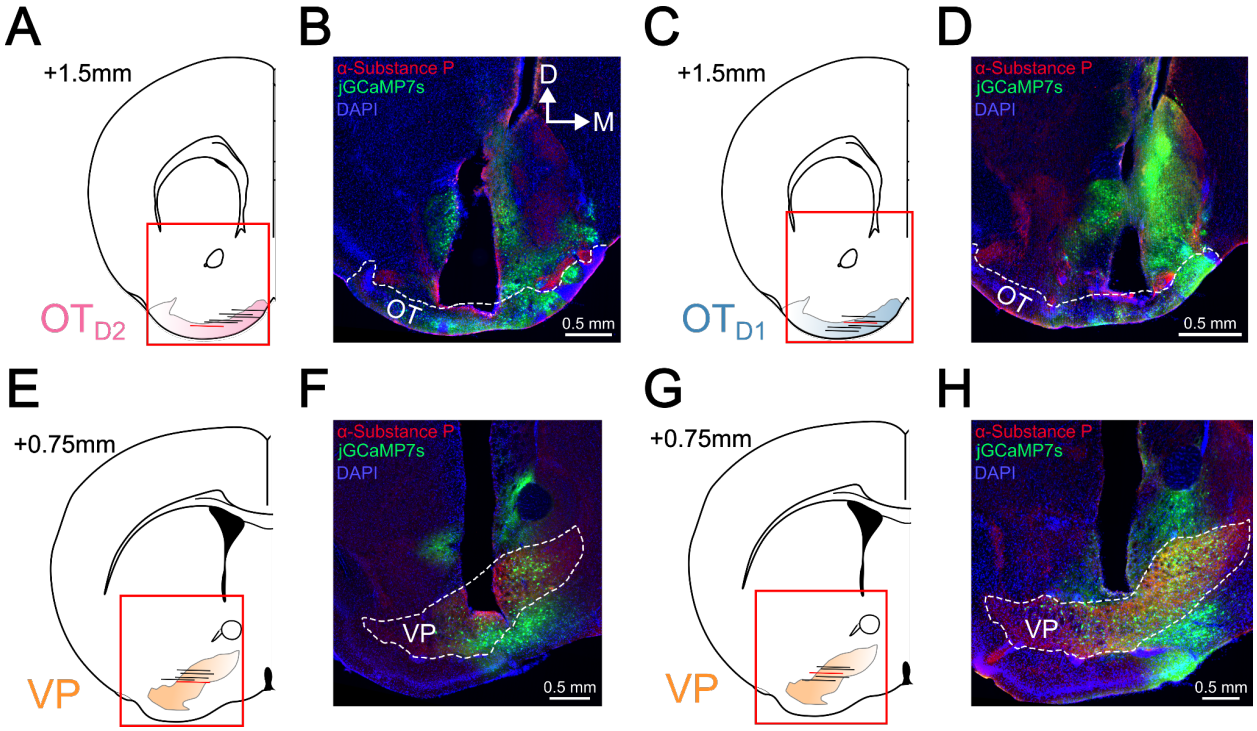
A
+1.5mm
OT$_{D2}$
B
α-Substance P
jGCaMP7s
DAPI
D
M
OT
0.5 mm
C
+1.5mm
OT$_{D1}$
D
α-Substance P
jGCaMP7s
DAPI
OT
0.5 mm
E
+0.75mm
VP
F
α-Substance P
jGCaMP7s
DAPI
VP
0.5 mm
G
+0.75mm
VP
H
α-Substance P
jGCaMP7s
DAPI
VP
0.5 mm

Figure S2. Histological verification of lens implant location. (**A**) Schematic showing the center, along the AP axis, of the implanted GRIN lens in 6 OT_{D2} jGCaMP7s animals. (**B**) Representative image of lens implant sites shown in (A). Sections were counterstained with α-Substance P to delineate the boundary of the VP. This sample is marked by a red horizontal line in (A). (**C**) Schematic as in (A) for 6 OT_{D1} jGCaMP7s animals. (**D**) Representative image of lens implant sites shown in (C). (**E**) Schematic as in (A) for 5 VP jGCaMP7s animals. (**F**) Representative image of lens implant sites shown in (E). (**G**) Schematic as in (A) for 5 VP jGCaMP7s animals recorded during the lick spout retraction paradigm (Figure 6). (**H**) Representative image of lens implant sites shown in (G). Sections were counterstained with α-Substance P to delineate the boundary of the VP. This sample is marked by a red horizontal line in (G).

Figure S3:

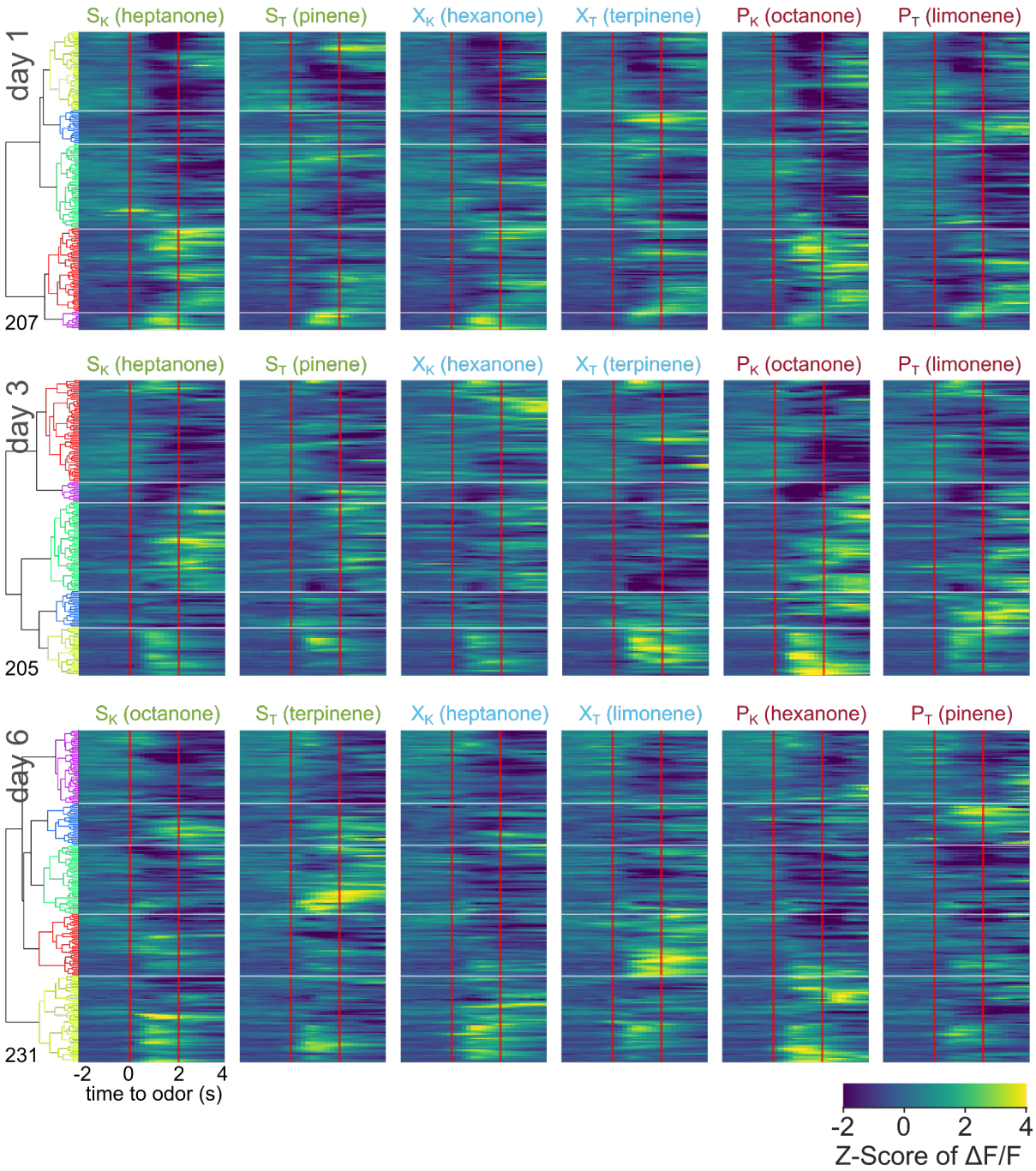
S_K (heptanone)
S_T (pinene)
X_K (hexanone)
X_T (terpinene)
P_K (octanone)
P_T (limonene)
day 1
207
S_K (heptanone)
S_T (pinene)
X_K (hexanone)
X_T (terpinene)
P_K (octanone)
P_T (limonene)
day 3
205
S_K (octanone)
S_T (terpinene)
X_K (heptanone)
X_T (limonene)
P_K (hexanone)
P_T (pinene)
day 6
231
-2 0 2 4
time to odor (s)
-2 0 2 4
Z-Score of ΔF/F

Figure S3. Pooled averaged-over-trials neural activity of all neurons from OT_{D2} animals across days. Heatmap of odor-evoked activity in OT_{D2} neurons from day 1, day 3, and day 6 of imaging. The fluorescence measurements from each neuron were averaged over trials, Z-scored, then pooled for hierarchical clustering. Neurons are grouped by similarity, with the dendrogram shown on the right. Horizontal white lines demarcate the boundaries between the 6 clusters. Odor delivered at 0-2 seconds marked by vertical red lines. From left to right, the columns represent neural responses to sucrose-paired ketone and terpene, control ketone and terpene, and airpuff-paired ketone and terpene (S_K, S_T, X_K, X_T, P_K, P_T). Data is pooled from 6 animals.

Figure S4:

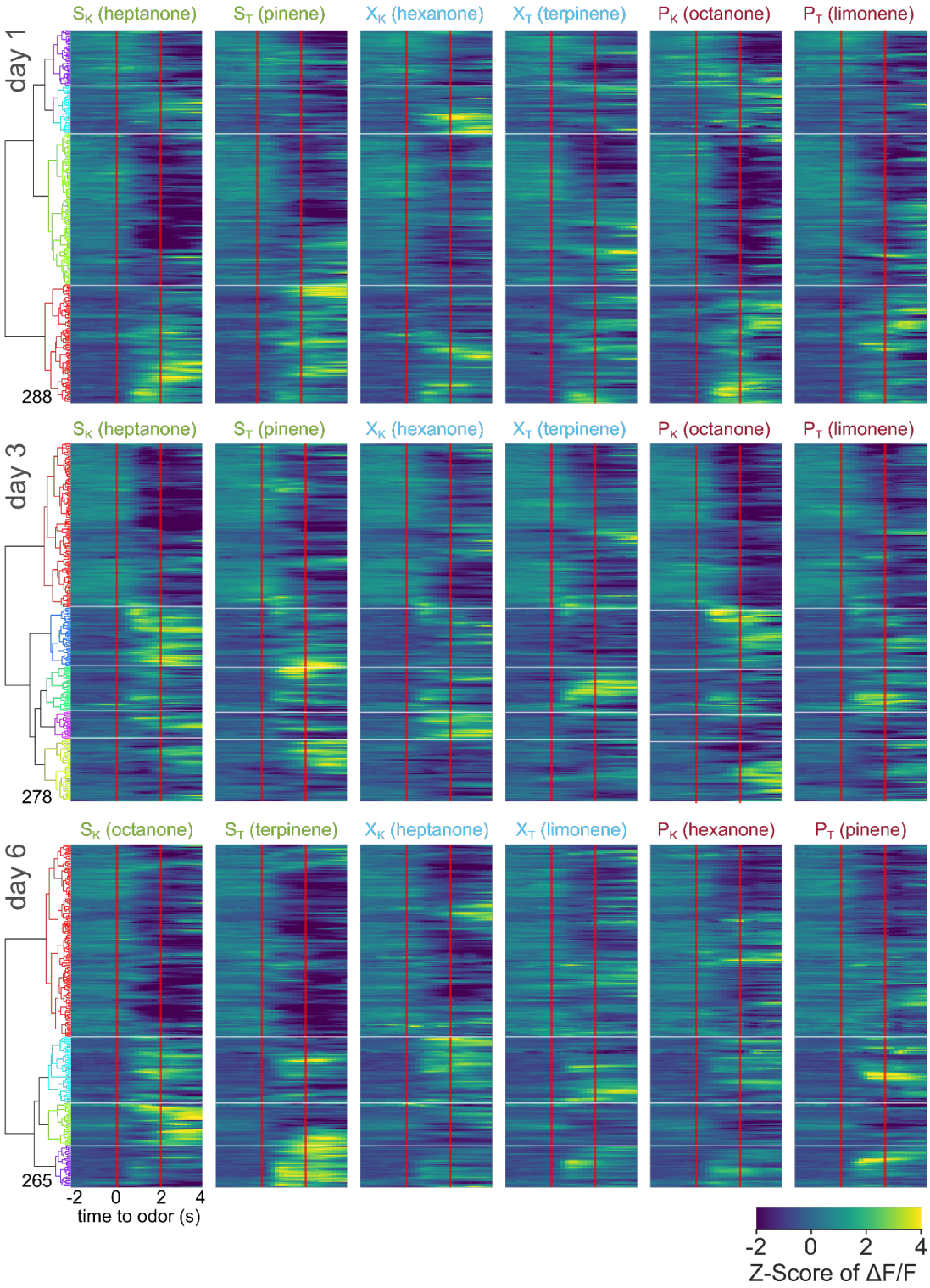
day 1
S_K (heptanone)
S_T (pinene)
X_K (hexanone)
X_T (terpinene)
P_K (octanone)
P_T (limonene)
288
day 3
S_K (heptanone)
S_T (pinene)
X_K (hexanone)
X_T (terpinene)
P_K (octanone)
P_T (limonene)
278
day 6
S_K (octanone)
S_T (terpinene)
X_K (heptanone)
X_T (limonene)
P_K (hexanone)
P_T (pinene)
265
-2 0 2 4
time to odor (s)
-2 0 2 4
Z-Score of ΔF/F

Figure S4. Pooled averaged-over-trials neural activity of all neurons from OT_{D1} animals across days. Heatmap of odor-evoked activity in OT_{D1} neurons from day 1, day 3, and day 6 of imaging.. The fluorescence measurements from each neuron were averaged over trials, Z-scored, then pooled for hierarchical clustering. Neurons are grouped by similarity, with the dendrogram shown on the right. Horizontal white lines demarcate the boundaries between the 6 clusters. Odor delivered at 0-2 seconds marked by vertical red lines. From left to right, the columns represent neural responses to sucrose-paired ketone and terpene, control ketone and terpene, and airpuff-paired ketone and terpene (S_K, S_T, X_K, X_T, P_K, P_T). Data is pooled from 6 animals.

Figure S5:

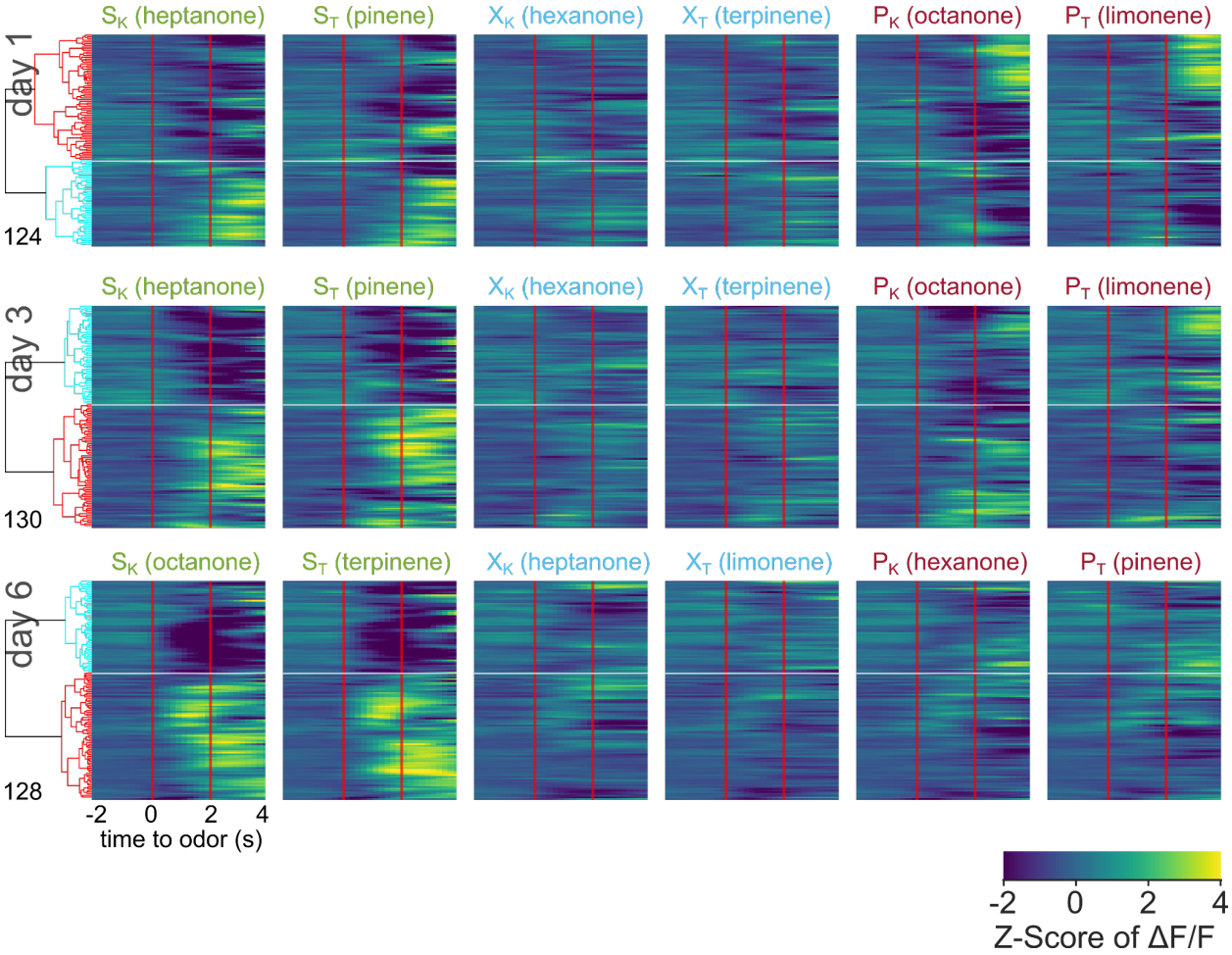
S_K (heptanone)
S_T (pinene)
X_K (hexanone)
X_T (terpinene)
P_K (octanone)
P_T (limonene)
day 1
124
S_K (heptanone)
S_T (pinene)
X_K (hexanone)
X_T (terpinene)
P_K (octanone)
P_T (limonene)
day 3
130
S_K (octanone)
S_T (terpinene)
X_K (heptanone)
X_T (limonene)
P_K (hexanone)
P_T (pinene)
day 6
128
-2 0 2 4
time to odor (s)
-2 0 2 4
Z-Score of ΔF/F

Figure S5. Pooled averaged-over-trials neural activity of all neurons from VP animals across days. Heatmap of odor-evoked activity in VP neurons from day 1, day 3, and day 6 of imaging. The fluorescence measurements from each neuron were averaged over trials, Z-scored, then pooled for hierarchical clustering. Neurons are grouped by similarity, with the dendrogram shown on the right. Horizontal white lines demarcate the boundaries between the 6 clusters. Odor delivered at 0-2 seconds marked by vertical red lines. From left to right, the columns represent neural responses to sucrose-paired ketone and terpene, control ketone and terpene, and airpuff-paired ketone and terpene (S_K, S_T, X_K, X_T, P_K, P_T). Data is pooled from 5 animals.

Figure S6:

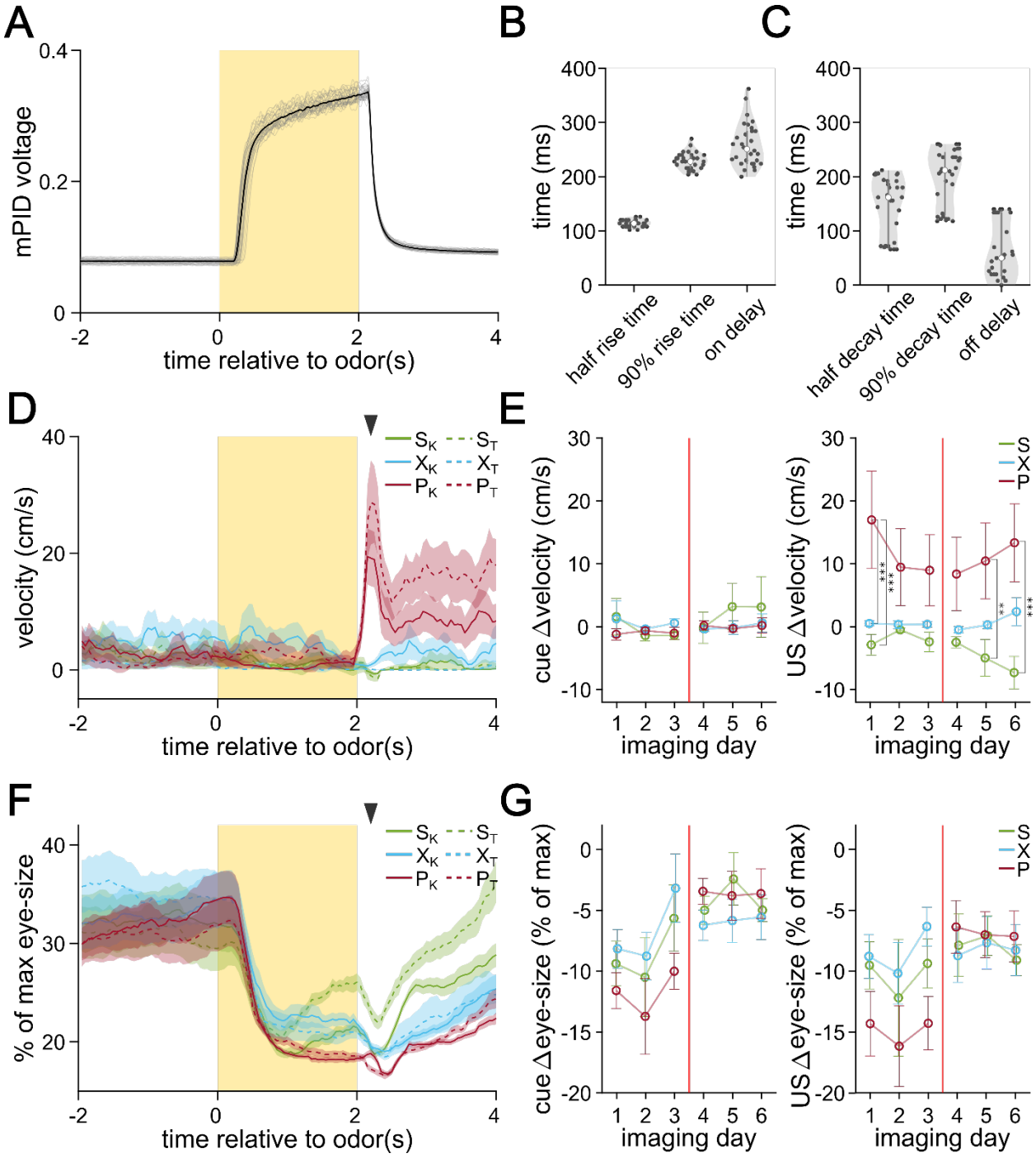
A
mPID voltage
time relative to odor(s)
B
time (ms)
half rise time
90% rise time
on delay
C
time (ms)
half decay time
90% decay time
off delay
D
velocity (cm/s)
time relative to odor(s)
E
cue Δvelocity (cm/s)
US Δvelocity (cm/s)
imaging day
F
% of max eye-size
time relative to odor(s)
G
cue Δeye-size (% of max)
US Δeye-size (% of max)
imaging day

Figure S6. Extended behavioral analysis from imaging period. (**A**) mPID voltage reading in response to 30 trials of a sample odor (α-terpinene) delivery. The time period during which the odor valve was turned on is shown by the yellow rectangle. Individual recordings are shown in gray and the average is shown in black. (**B**) On-kinetics of odor delivery. On delay refers to the interval between the valve turning on and the mPID voltage increasing by more than 10% of baseline. (**C**) Off-kinetics of odor delivery. Off delay refers to the interval between the odor valve turning off and the mPID voltage decreasing by more than 10% of its maximum. (**D**) Representative velocity of the head-fixed mouse in response to the 6 different odors measured by a digital encoder. The lines represent the average across 30 trials and the shaded areas represent the SEM. The black arrowhead marks when the US is delivered. (**E**) The difference in walking velocity in response to odor (left) and US delivery (right). Differences are calculated between the last second before odor delivery and the last second before the odor exposure (left) or the first half second after US delivery (right) grouped by US pairing. Circles represent the average across animals and the error bars show SEM. (**F**) Representative changes in range-normalized eye-size in response to the 6 different odors. (**G**) The difference in eye-size in response to odor (left) and US delivery (right). Differences are calculated between the last second before odor delivery and the last second before the odor exposure (left) or the first half second after US delivery (right) grouped by US pairing. Circles represent the average across animals and the error bars show SEM. FWER-adjusted statistical significance for post hoc comparisons are shown as: ***$p<0.001$, **$p<0.01$, *$p<0.05$, n.s. $p>0.05$. See Tables S32-36 for detailed statistics.

Figure S7:

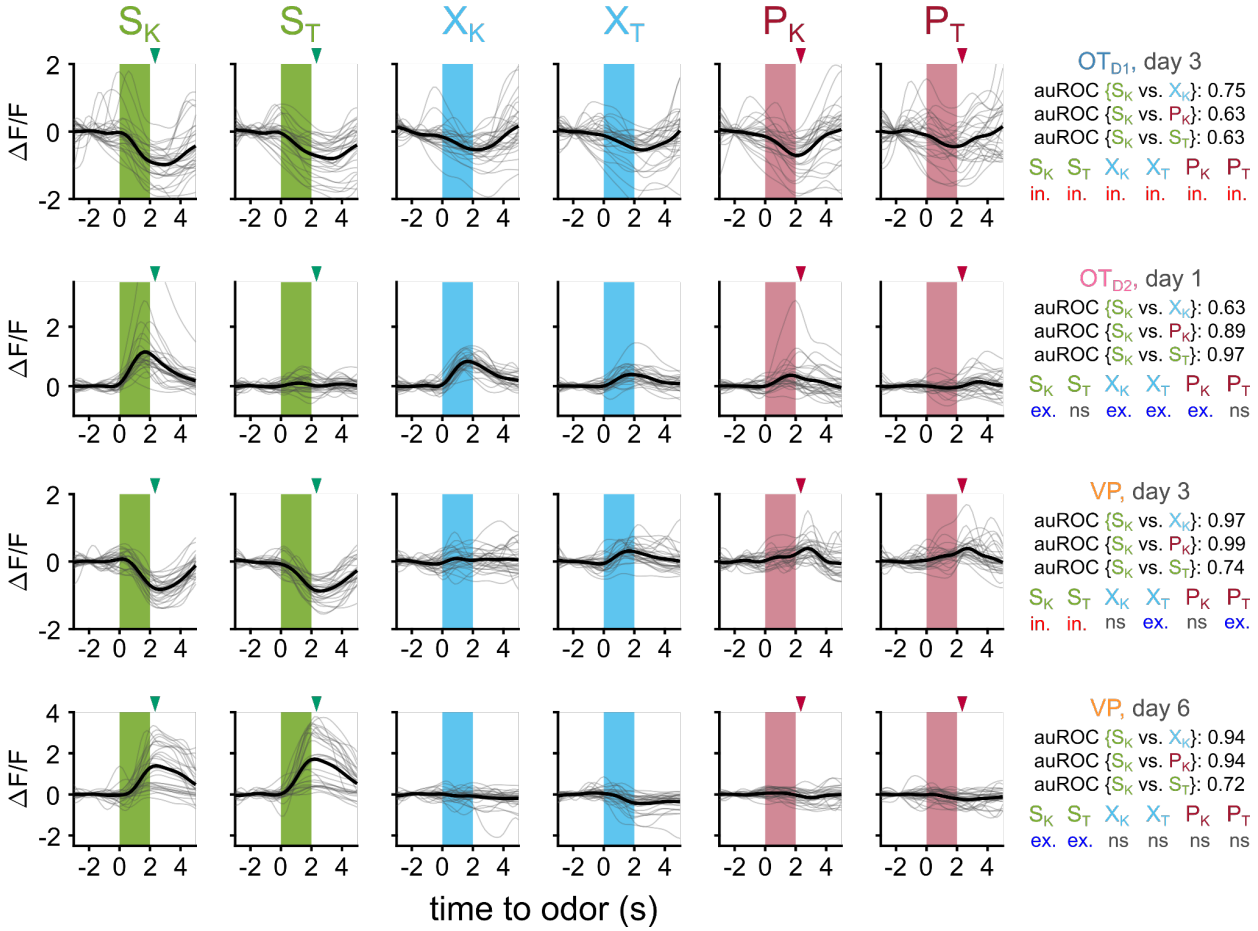
S_K S_T X_K X_T P_K P_T
ΔF/F
time to odor (s)
OT_{D1}, day 3
auROC {S_K vs. X_K}: 0.75
auROC {S_K vs. P_K}: 0.63
auROC {S_K vs. S_T}: 0.63
S_K S_T X_K X_T P_K P_T
in. in. in. in. in. in.
OT_{D2}, day 1
auROC {S_K vs. X_K}: 0.63
auROC {S_K vs. P_K}: 0.89
auROC {S_K vs. S_T}: 0.97
S_K S_T X_K X_T P_K P_T
ex. ns ex. ex. ex. ns
VP, day 3
auROC {S_K vs. X_K}: 0.97
auROC {S_K vs. P_K}: 0.99
auROC {S_K vs. S_T}: 0.74
S_K S_T X_K X_T P_K P_T
in. in. ns ex. ns ex.
VP, day 6
auROC {S_K vs. X_K}: 0.94
auROC {S_K vs. P_K}: 0.94
auROC {S_K vs. S_T}: 0.72
S_K S_T X_K X_T P_K P_T
ex. ex. ns ns ns ns

Figure S7. Traces of example neurons and their corresponding metrics. (**A**) Example traces from an OT_{D1} neuron recorded on day 3. Each column shows this neuron's response to a given odor across 30 trials (gray). The average across all trials is shown in black. For green and red arrowheads mark the time at which sucrose and airpuff were delivered, respectively. auROC values from single-neuron binary classifiers for discriminating {S_K vs. X_K}, {S_K vs. P_K}, and {S_K vs. S_T} are displayed on the right. Additionally, the results of statistical analysis to determine if this neuron reliably responded to each odor (in. = significant inhibitory response, exc. = significant excitatory response, ns= no significant difference between baseline and odor period). (**B**) Example traces from an OT_{D2} neuron recorded on day 1. (**C**) Example traces from a VP neuron recorded on day 3. (**D**) Example traces from a VP neuron recorded on day 6.

Figure S8:

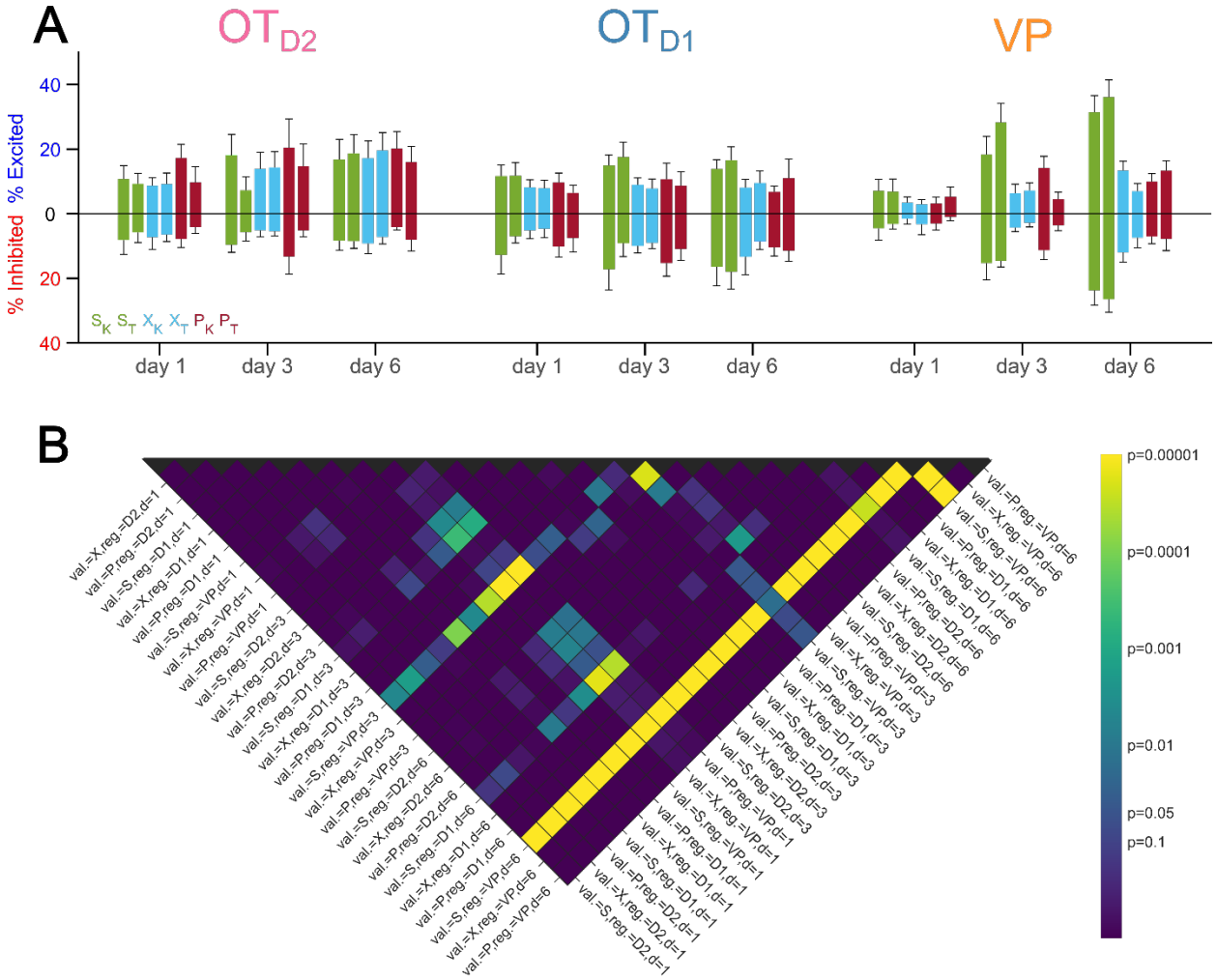
A
OTD2
OTD1
VP
% Inhibited % Excited
40
20
0
20
40
SK ST XK XT PK PT
day 1
day 3
day 6
day 1
day 3
day 6
day 1
day 3
day 6
B
p=0.00001
p=0.0001
p=0.001
p=0.01
p=0.05
p=0.1

Figure S8. Percentage of neurons responsive to each odor across days. (**A**) Bar graphs showing percentage of neurons from each region on imaging days 1, 3 and 6 that were significantly excited or inhibited by each odor. The average across animals is shown by the bar and the error bars represent SEM. (**B**) Heatmap of post hoc pairwise comparison p-values of percent responsive across imaging days and imaging region. See Table S37 for detailed statistics.

Figure S9:

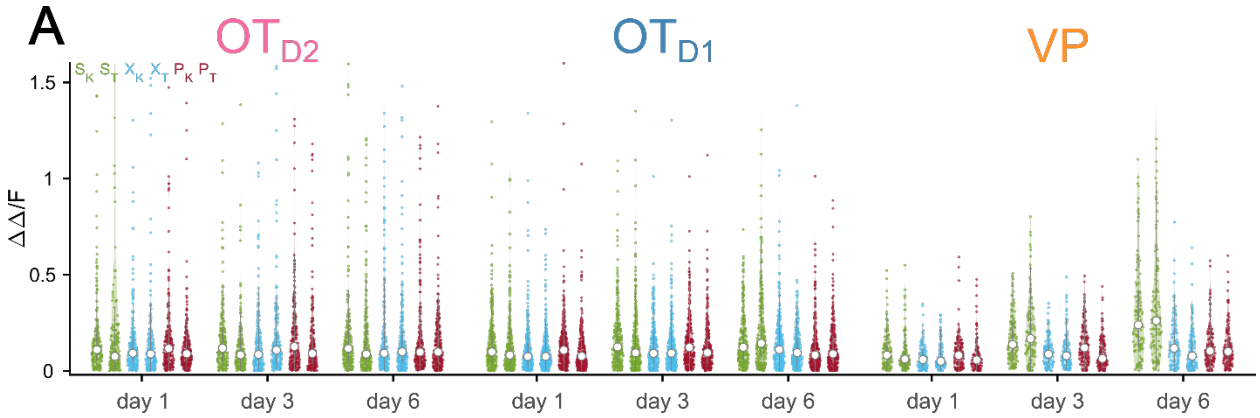
A
OTD2
OTD1
VP
SK ST XK XT PK PT
1.5
1
0.5
0
ΔΔ/F
day 1
day 3
day 6
day 1
day 3
day 6
day 1
day 3
day 6

Figure S9. Distribution of response magnitudes to each odor across days. Violin plots showing the averaged-over-trials response magnitudes to each odor during the last second of odor exposure. See Table S38 for detailed statistics.

Figure S10:

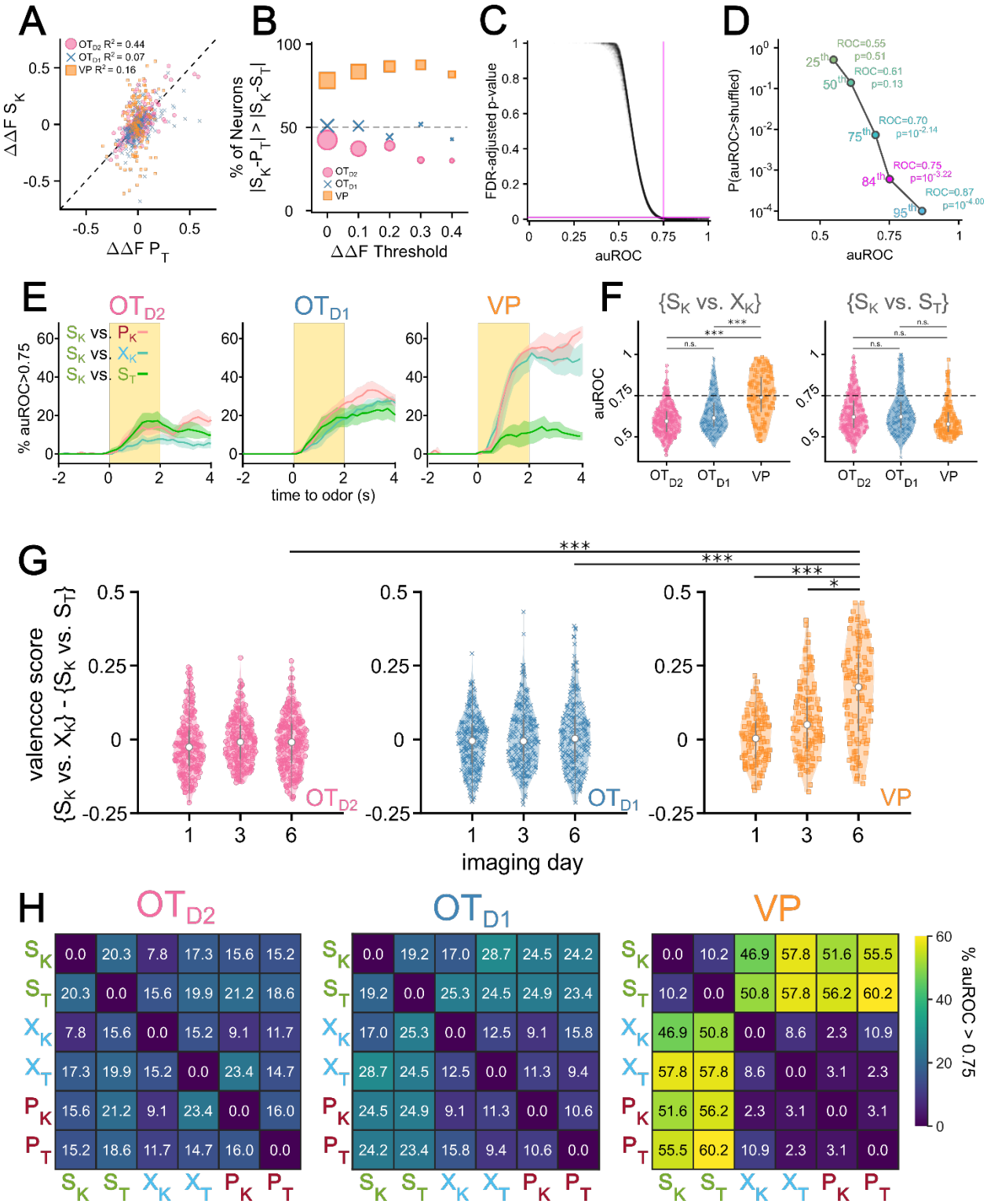
A
OTD2 R² = 0.44
OTD1 R² = 0.07
VP R² = 0.16
ΔΔF SK
ΔΔF PT
B
% of Neurons |SK-PT| > |SK-ST|
OTD2
OTD1
VP
ΔΔF Threshold
C
FDR-adjusted p-value
auROC
D
P(auROC>shuffled)
ROC=0.55 p=0.51
ROC=0.61 p=0.13
ROC=0.70 p=10^-2.14
ROC=0.75 p=10^-3.22
ROC=0.87 p=10^-4.00
25th
50th
75th
84th
95th
auROC
E
OTD2
OTD1
VP
SK vs. PK
SK vs. XK
SK vs. ST
% auROC>0.75
time to odor (s)
F
{SK vs. XK}
{SK vs. ST}
auROC
n.s.
***
G
valencce score
{SK vs. XK} - {SK vs. ST}
imaging day
H
OTD2
OTD1
VP
% auROC > 0.75

Figure S10. Pairwise analysis of single neuron odor encoding.

(**A**) Scatterplot comparing the magnitudes of S_K responses ($\Delta\Delta S_K$) to P_T responses ($\Delta\Delta P_T$). The dotted line represents the hypothetical scenario where $\Delta\Delta S_K = \Delta\Delta P_T$. For each population, the R^2 value of the 2-d distribution compared to the $\Delta\Delta S_K = \Delta\Delta P_T$ line is reported. (**B**) The percentage of neurons from each population where the difference between $\Delta\Delta S_K$ and $\Delta\Delta P_T$ is lower than that between $\Delta\Delta S_K$ and $\Delta\Delta S_T$. (**C**) Bootstrapped FDR-adjusted p-values as a function of auROC values of single-neuron binary classifiers. In total, there are 27,900 single-neuron binary classifiers (15 pairwise classifiers for each of the 1860 recordings across 3 regions and days 1, 3 and 6 of imaging). Each classifier was compared against 10,000 shuffles. Horizontal magenta line marks FDR-adjusted p-value of 0.001 and the vertical magenta line marks auROC of 0.75. (**D**) The 25th, 50th, 75th, 84th and 95th percentiles of auROC values and their corresponding unadjusted p-values. For auROC values that were greater than all 10,000 shuffles, a conservative p-value of 0.0001 was assigned. (**E**) The percentage of day 6 {S_K vs P_K}, {S_K vs X_K}, and {S_K vs S_T} auROC values greater than 0.75 as a function of time relative to odor, grouped by region. Lines represent the average across biological replicates and the shaded area shows the SEM. (**F**) Violin plot showing the distribution of pooled day 6 {S_K vs X_K} (left) and {S_K vs S_T} (right) auROC values grouped by region. Horizontal dotted line marks auROC = 0.75. (**G**) Violin plot of the distribution of single-neuron valence scores (defined as the difference between the average auROC for {S vs. X|P} classification and {S_K vs. S_T} classification), grouped by imaging day and region. (**H**) Heatmap of percentage of single-neuron pairwise classifiers with auROC>0.75. Classifiers were trained from neural activity recorded during the last second of odor exposure. Percentage of neurons with auROC>0.75 for a given binary classification was averaged across animals and grouped by region. For post hoc pairwise comparisons, the median values for all neurons in each animal were compared across imaging day and region. The FWER-adjusted p-values are shown as: ***p<0.001, **p<0.01, *p<0.05, n.s. p>0.05. See Tables S39-46 for detailed statistics.

Figure S11:

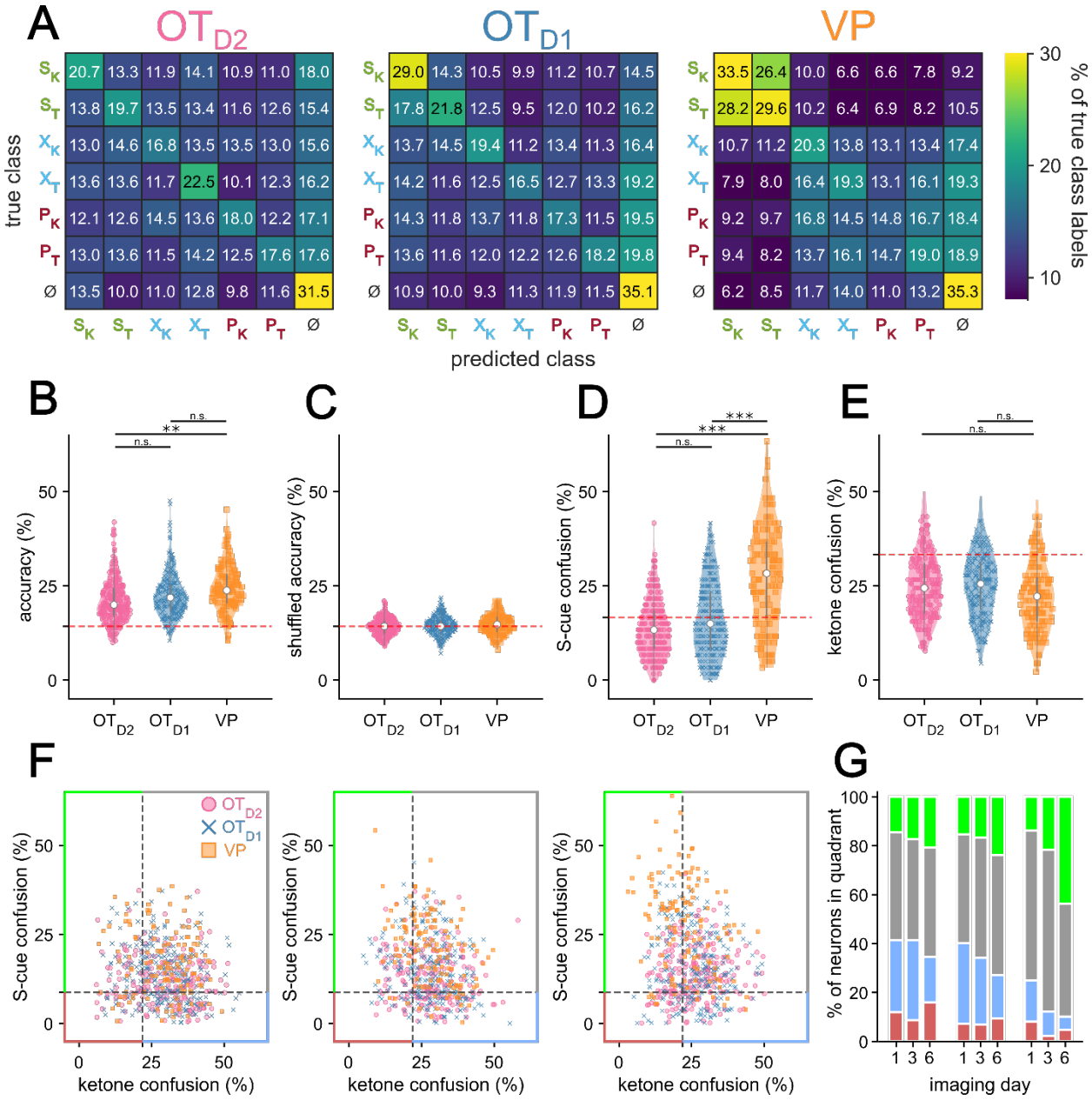
A
OTD2
OTD1
VP
true class
predicted class
% of true class labels
B
C
D
E
accuracy (%)
shuffled accuracy (%)
S-cue confusion (%)
ketone confusion (%)
n.s.
**
***
F
G
% of neurons in quadrant
imaging day

Figure S11. Multinomial analysis of single neuron odor encoding (**A**) Confusion matrix of single-neuron MNR classifiers trained on neural activity during the last second of odor exposure on day 6 of imaging. Rows represent the true class while columns represent the predicted class. Each confusion matrix is averaged across 10 k-fold and across all neurons of a given region. ϕ represents data taken from 30 pre-odor bins randomly sampled from -1.5 to -0.5 seconds relative to odor delivery. (**B**) Violin plot of single-neuron MNR classifier accuracy, averaged across 10 k-fold, grouped by region. (**C**) Violin plot of the single-neuron MNR classifier accuracy trained on shuffled data. Each data point represents the average across 10 shuffles. (**D**) Violin plot of MNR S-cue confusion, i.e. confusion between S_K and S_T. This corresponds to 1) when the true class was S_K but predicted class was S_T and 2) when the true class was S_T but the predicted class was S_K. (**E**) Violin plot of MNR confusion among all ketones. This corresponds when the true class was a ketone and the predicted class was a different ketone (e.g. true class = X_K and predicted class = P_K). (**F**) Scatterplot of each neuron's ketone confusion on the x-axis and S-cue confusion on the y-axis on days 1, 3, and 6 of imaging. (**G**) Stacked bar graph showing the distribution of neurons from each population that fall into each of the 4 quadrants across the 3 different imaging days. For post hoc pairwise comparisons, the median values for all neurons in each animal were compared across imaging day and region. The FWER-adjusted p-values are shown as: ***$p<0.001$, **$p<0.01$, *$p<0.05$, n.s. $p>0.05$. See Tables S47-53 for detailed statistics.

Figure S12:

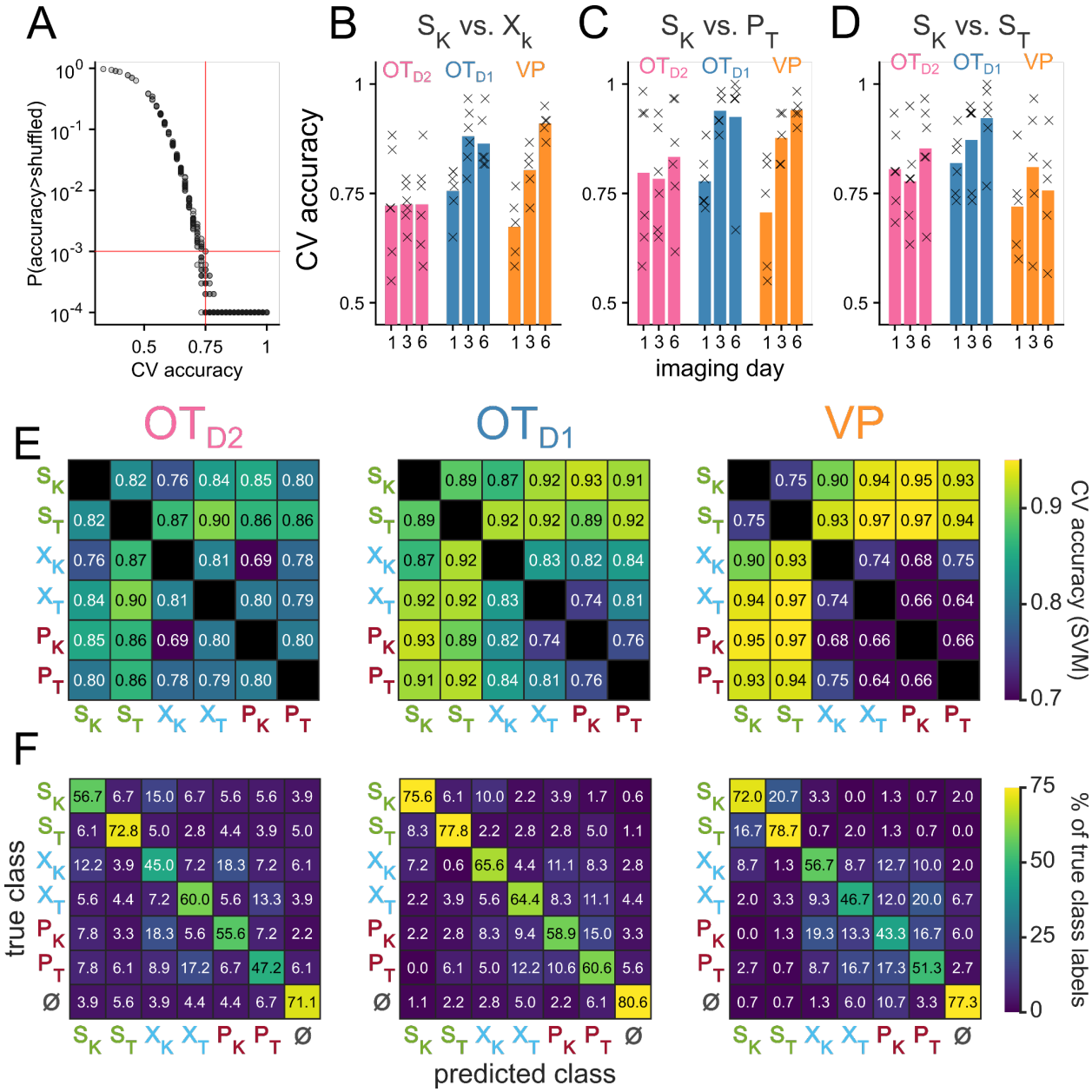
A
P(accuracy>shuffled)
CV accuracy
B
S_K vs. X_k
C
S_K vs. P_T
D
S_K vs. S_T
OT_{D2} OT_{D1} VP
CV accuracy
imaging day
E
OT_{D2}
OT_{D1}
VP
CV accuracy (SVM)
F
true class
predicted class
% of true class labels

Figure S12. Analysis of population-level odor encoding (**A**) Scatterplot of CV-accuracy of linear classifiers trained on simultaneously-recorded neurons on the x-axis and their bootstrapped unadjusted p-values on the y-axis. Red horizontal line marks p = 0.001 and red red vertical line marks CV accuracy = 0.75. All classifiers with CV accuracy higher than 0.75 had p<0.001. In total, there are 765 binary classifiers (15 pairwise classifiers for each of the 51 recordings across 3 regions and days 1, 3, and 6 of imaging). Each classifier was compared against 10,000 shuffles. For auROC values that were greater than all 10,000 shuffles, a conservative p-value of 0.0001 was assigned. (**B**) The CV accuracy for {S_K vs X_K} binary classification trained on the last second of population-level activity. The bars represent the average across biological replicates. CV accuracy from individual animals are shown as x's. (**C**) Same as (B) but for {S_K vs. P_T} classification. (**D**) Same as (B) but for {S_K vs. S_T} classification. (**E**) Heatmap of CV accuracy from binary SVM's trained on day 6 of imaging with a radial basis function kernel. CV accuracy was averaged across biological replicates. (**F**) Confusion matrix of population-level MNR classifiers trained on neural activity during the last second of odor exposure on day 6 of imaging. Rows represent the true class while columns represent the predicted class. Each confusion matrix is averaged across biological replicates. ϕ represents data taken from 30 pre-odor bins randomly sampled from -1.5 to -0.5 seconds relative to odor delivery. See Tables S54-59 for details on statistical comparison of average classifier accuracy across animals.

Figure S13:

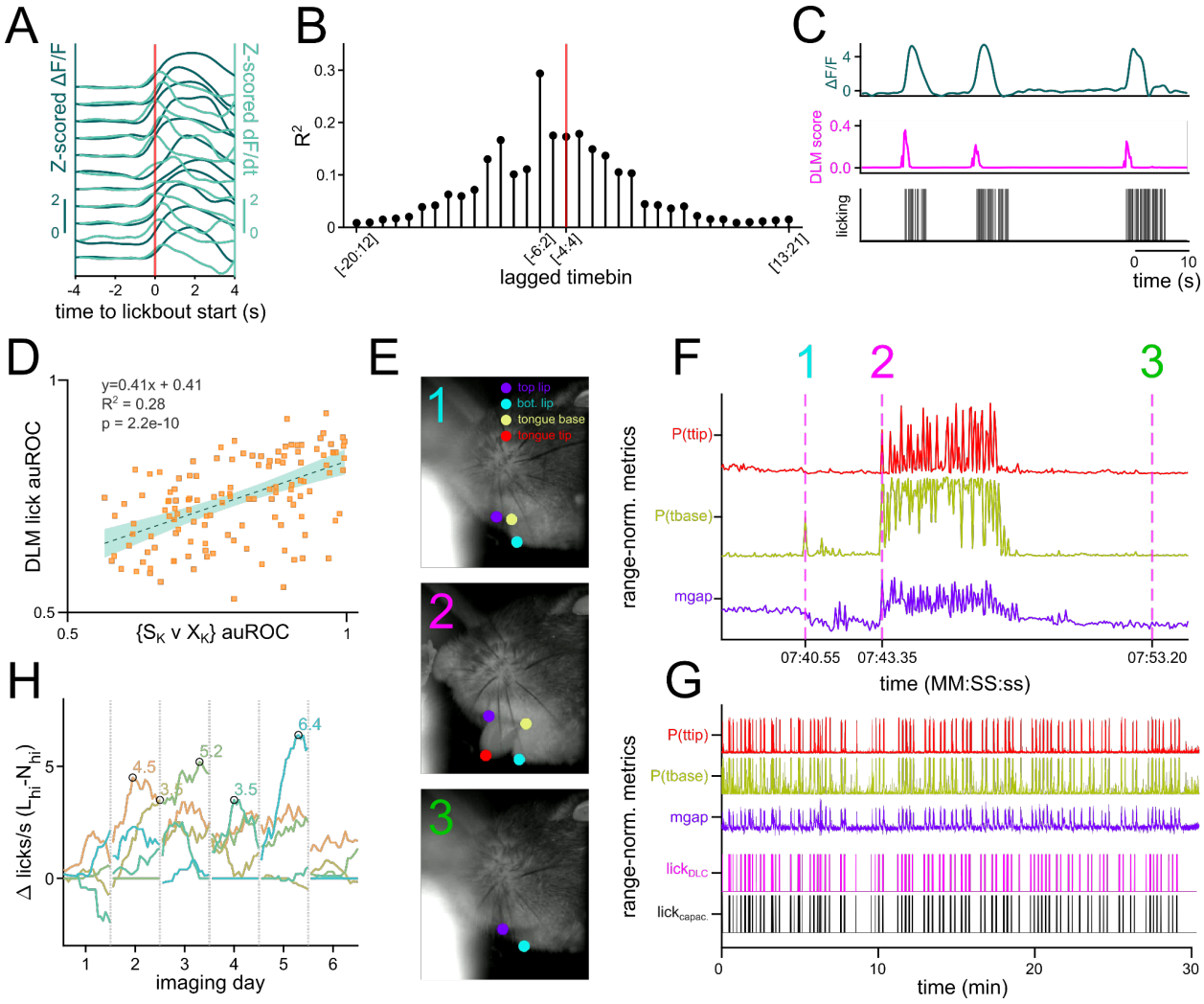
A
Z-scored ΔF/F
Z-scored dF/dt
time to lickbout start (s)
B
R²
lagged timebin
[-20:12]
[-6:2]
[-4:4]
[13:21]
C
ΔF/F
DLM score
licking
time (s)
D
y=0.41x + 0.41
R² = 0.28
p = 2.2e-10
DLM lick auROC
{S_K v X_K} auROC
E
top lip
bot. lip
tongue base
tongue tip
F
range-norm. metrics
P(ttip)
P(tbase)
mgap
07:40.55
07:43.35
07:53.20
time (MM:SS:ss)
G
lick_DLC
lick_capac
time (min)
H
Δ licks/s (L_hi-N_hi)
imaging day

Figure S13. Camera-based detection of licking in head-fixed animals (**A-C**) Metrics of a representative neurons with activity that predicts licking. (**A**) Representative neuron's Z-scored ΔF/F (dark green) and Z-scored dF/dt (light green) aligned to the onset of a lickbout. Each line represents the same neuron's activity during an individual lickbout. (**B**) Stemplot showing an example of the lagged correlation between the onset of licking and the fluorescence of a neuron across 9 frames (1 frame = 0.2s). Time bins of various lags are shown on the x-axis (negative number denotes frames that precede onset of licking) and the resulting R^2 is plotted on the y-axis. Red vertical line marks the case where the 9 frames are centered on the onset of licking. As an example, [-6:2] refers to fluorescence between 1.2 seconds prior to lickbout onset and 0.4 seconds after lickbout onset. (**C**) The output of a distributed lag model (DLM) that predicts the onset of a lickbout from ΔF/F of a single neuron. ΔF/F (dark green, top), DLM score (magenta, middle), and the licking recorded by a capacitive sensor (black, bottom) are shown in parallel. The DLM model was trained using 9 distributed frames ([-6:2]) of ΔF/F for each frame of lickbout onset. (**D**) Scatterplot of day 6 VP neurons' DLM lick classifier auROC on the y-axis plotted against their mean {S_K vs. X_K} auROC on the x-axis. The slope, intercept, R^2, and p-value of the slope are shown on the top left corner. (**E**) 3 example snapshots of the camera feed during moving lick spout paradigm with overlay of DeepLabCut labeling. The coordinates of top lip, bottom lip, base of tongue (tbase), and tip of tongue (ttip) are displayed with a probability cutoff of 0.4. (**F**) Range-normalized metrics from DLC labeling. P(ttip) (red, top) is the probability score assigned to the labeling of the tongue tip. P(tbase) (yellow, middle) is the probability score assigned to the labeling of the tongue base. Mgap (purple, bottom) is the Euclidean distance between the top lip and the bottom lip. The 3 vertical magenta lines represent the timing of the 3 snapshots shown in (E). (**G**) The same range-normalized metrics as in (F) plotted against the ground truth licking data from capacitive sensor (black, bottom) and DLC-based licking classifier score (magenta, second from bottom). (**H**) Lineplot showing the difference in total licking to L_{hi} and N_{hi} during the time bin (1.5-2.5 seconds after odor onset) used for most analyses plotted against imaging day for individual animals. The time of peak difference is circled in black.

Supplemental Tables

Table S1:

Group A	Group B	Lower Limit	A-B	Upper Limit	FDR adjusted P-value
$OT_{D1} \rightarrow VP$	$Acb_{D1} \rightarrow VP$	-20.506	-8.798	2.910	0.577
$OT_{D1} \rightarrow VP$	$OT_{D2} \rightarrow VP$	-0.851	9.922	20.694	0.577
$OT_{D1} \rightarrow VP$	$Acb_{D2} \rightarrow VP$	9.338	19.340	29.341	0.291
$Acb_{D1} \rightarrow VP$	$OT_{D2} \rightarrow VP$	11.163	18.719	26.275	0.161
$Acb_{D1} \rightarrow VP$	$Acb_{D2} \rightarrow VP$	21.729	28.137	34.545	3.394E-02
$OT_{D2} \rightarrow VP$	$Acb_{D2} \rightarrow VP$	4.942	9.418	13.894	0.206
$OT_{D1} \rightarrow VP$	$Acb_{D1} \rightarrow VP$	-9.944	-8.199	-6.453	2.223E-02
$OT_{D1} \rightarrow LH$	$OT_{D2} \rightarrow LH$	-0.045	0.564	1.173	0.577
$OT_{D1} \rightarrow LH$	$Acb_{D2} \rightarrow LH$	-0.016	0.591	1.198	0.577
$Acb_{D1} \rightarrow LH$	$OT_{D2} \rightarrow LH$	7.125	8.763	10.401	2.223E-02
$Acb_{D1} \rightarrow LH$	$Acb_{D2} \rightarrow LH$	7.153	8.790	10.426	2.223E-02
$OT_{D2} \rightarrow LH$	$Acb_{D2} \rightarrow LH$	-0.029	0.027	0.082	0.655
$OT_{D1} \rightarrow VTA$	$Acb_{D1} \rightarrow VTA$	-17.357	-14.504	-11.650	2.223E-02
$OT_{D1} \rightarrow VTA$	$OT_{D2} \rightarrow VTA$	-0.022	0.183	0.387	0.577

Table S1. Pairwise comparisons of anterograde labeling from OT and AcbSh (Fig1C).

Table S2:

Group A	Group B	Lower Limit	A-B	Upper Limit	FDR adjusted P-value
AI→vlVP	AI→dmVP	78.249	148.500	218.751	0.116
Acb→vlVP	Acb→dmVP	-185.929	-123.250	-60.571	0.116
LS→vlVP	LS→dmVP	-130.496	-118.750	-107.004	3.27E-04
OFC→vlVP	OFC→dmVP	-167.021	-132.000	-96.979	1.86E-02
OT→vlVP	OT→dmVP	179.793	221.750	263.707	5.57E-03
Pir→vlVP	Pir→dmVP	-71.946	-21.500	28.946	0.685

Table S2. Pairwise comparisons of retrograde labeling from vlVP and dmVP (Fig1F).

Table S3:

Group A	Group B	Lower Limit	A-B	Upper Limit	FDR adjusted P-value
OT→VTA	AcbSh→VTA	-735.101	-575	-414.899	3.44E-02
OT→VTA	AcbC→VTA	-1027.381	-915	-802.619	3.71E-03
AcbC→VTA	AcbSh→VTA	144.452	340	535.548	0.157

Table S3. Pairwise comparisons of retrograde labeling from VTA (Fig1I).

Table S4:

Source	Sum Sq.	d.f.	Mean Sq.	F	Prob>F
day	4.301	5	0.860	27.638	2.29E-16
region	0.143	2	0.072	2.301	0.106
day:region	0.251	10	0.025	0.806	0.623
Error	2.583	83	0.031		
Total	7.305	100			

Table S4. 2-way ANOVA for effect of day or lens placement on licking accuracy (Fig2H).

Table S5:

Group A	Group B	Lower Limit	A-B	Upper Limit	P-value
day 1	day 2	-0.385	-0.208	-0.031	1.18E-02
day 1	day 3	-0.632	-0.452	-0.272	2.03E-09
day 1	day 4	-0.134	0.043	0.220	0.980
day 1	day 5	-0.558	-0.381	-0.203	2.30E-07
day 1	day 6	-0.650	-0.473	-0.295	2.58E-10
day 2	day 3	-0.424	-0.244	-0.064	2.18E-03
day 2	day 4	0.074	0.251	0.429	1.14E-03
day 2	day 5	-0.350	-0.172	0.005	0.061
day 2	day 6	-0.441	-0.264	-0.087	5.33E-04
day 3	day 4	0.315	0.495	0.675	8.31E-11
day 3	day 5	-0.109	0.071	0.251	0.856
day 3	day 6	-0.200	-0.021	0.159	0.999
day 4	day 5	-0.601	-0.424	-0.247	1.00E-08
day 4	day 6	-0.693	-0.516	-0.338	9.77E-12
day 5	day 6	-0.269	-0.092	0.085	0.657

Table S5. Post hoc pairwise comparisons of licking accuracy across imaging days (Fig2H).

Table S6:

Source	Sum Sq.	d.f.	Mean Sq.	F	Prob>F
day	0.05917	2	0.02958	2.99563	0.06079
region	0.03696	2	0.01848	1.87142	0.16651
day:region	0.06481	4	0.01620	1.64062	0.18197
Error	0.41479	42	0.00988		
Total	0.57170	50			

Table S6. 2-way ANOVA for effect of day or lens placement on percentage of neurons responsive to a single odor (Fig3E).

Table S7:

Group A	Group B	Lower Limit	A-B	Upper Limit	P-value
d1,D2 OT	d3,D2 OT	-0.140	0.048	0.236	0.995
d1,D2 OT	d6,D2 OT	-0.164	0.024	0.211	1.000
d3,D2 OT	d6,D2 OT	-0.212	-0.024	0.163	1.000
d1,D1 OT	d3,D1 OT	-0.287	-0.099	0.088	0.724
d1,D1 OT	d6,D1 OT	-0.328	-0.141	0.047	0.285
d3,D1 OT	d6,D1 OT	-0.229	-0.041	0.146	0.998
d1,VP	d3,VP	-0.321	-0.115	0.090	0.662
d1,VP	d6,VP	-0.335	-0.129	0.076	0.513
d3,VP	d6,VP	-0.220	-0.014	0.191	1.000
d1,D2 OT	d1,D1 OT	-0.115	0.072	0.260	0.937
d1,D2 OT	d1,VP	-0.056	0.141	0.338	0.341
d1,D1 OT	d1,VP	-0.128	0.069	0.265	0.964
d3,D2 OT	d3,D1 OT	-0.263	-0.075	0.112	0.923
d3,D2 OT	d3,VP	-0.219	-0.022	0.175	1.000
d3,D1 OT	d3,VP	-0.144	0.053	0.250	0.993
d6,D2 OT	d6,D1 OT	-0.280	-0.092	0.095	0.796
d6,D2 OT	d6,VP	-0.209	-0.012	0.184	1.000
d6,D1 OT	d6,VP	-0.117	0.080	0.276	0.918

Table S7. Post hoc pairwise comparisons of percentage of neurons responsive to a single odor across imaging days and region (Fig3E).

Table S8:

Source	Sum Sq.	d.f.	Mean Sq.	F	Prob>F
day	0.10897	2	0.05448	4.58607	0.01580
region	0.00469	2	0.00234	0.19732	0.82168
day:region	0.06640	4	0.01660	1.39730	0.25144
Error	0.49897	42	0.01188		
Total	0.66598	50			

Table S8. 2-way ANOVA for effect of day or lens placement on percentage of neurons responsive to 3 or more odors (Fig3E).

Table S9:

Group A	Group B	Lower Limit	A-B	Upper Limit	P-value
d1,D2 OT	d3,D2 OT	-0.237	-0.031	0.175	1.000
d1,D2 OT	d6,D2 OT	-0.246	-0.040	0.165	0.999
d3,D2 OT	d6,D2 OT	-0.215	-0.009	0.196	1.000
d1,D1 OT	d3,D1 OT	-0.230	-0.024	0.182	1.000
d1,D1 OT	d6,D1 OT	-0.269	-0.063	0.143	0.984
d3,D1 OT	d6,D1 OT	-0.245	-0.039	0.167	0.999
d1,VP	d3,VP	-0.406	-0.181	0.044	0.207
d1,VP	d6,VP	-0.453	-0.228	-0.003	0.046
d3,VP	d6,VP	-0.272	-0.047	0.178	0.999
d1,D2 OT	d1,D1 OT	-0.220	-0.014	0.191	1.000
d1,D2 OT	d1,VP	-0.124	0.092	0.308	0.894
d1,D1 OT	d1,VP	-0.109	0.106	0.322	0.793
d3,D2 OT	d3,D1 OT	-0.213	-0.007	0.198	1.000
d3,D2 OT	d3,VP	-0.274	-0.058	0.158	0.993
d3,D1 OT	d3,VP	-0.266	-0.051	0.165	0.997
d6,D2 OT	d6,D1 OT	-0.243	-0.037	0.168	1.000
d6,D2 OT	d6,VP	-0.311	-0.096	0.120	0.871
d6,D1 OT	d6,VP	-0.274	-0.059	0.157	0.993

Table S9. Post hoc pairwise comparisons of percentage of neurons responsive to 3 or more odors across imaging days and region (Fig3E).

Table S10:

Source	Sum Sq.	d.f.	Mean Sq.	F	Prob>F
day	0.11460	2	0.05730	6.60475	0.00321
region	0.18370	2	0.09185	10.58706	0.00019
day:region	0.16522	4	0.04131	4.76096	0.00294
Error	0.36438	42	0.00868		
Total	0.80767	50			

Table S10. 2-way ANOVA for effect of day or lens placement on percentage of neurons responsive to both S-cues (Fig3E).

Table S11:

Group A	Group B	Lower Limit	A-B	Upper Limit	P-value
d1,D2 OT	d3,D2 OT	-0.139	0.037	0.213	0.999
d1,D2 OT	d6,D2 OT	-0.200	-0.024	0.151	1.000
d3,D2 OT	d6,D2 OT	-0.237	-0.062	0.114	0.963
d1,D1 OT	d3,D1 OT	-0.239	-0.063	0.112	0.957
d1,D1 OT	d6,D1 OT	-0.196	-0.020	0.156	1.000
d3,D1 OT	d6,D1 OT	-0.133	0.043	0.219	0.996
d1,VP	d3,VP	-0.441	-0.248	-0.056	3.79E-03
d1,VP	d6,VP	-0.473	-0.281	-0.088	7.12E-04
d3,VP	d6,VP	-0.225	-0.032	0.160	1.000
d1,D2 OT	d1,D1 OT	-0.189	-0.013	0.163	1.000
d1,D2 OT	d1,VP	-0.151	0.033	0.217	1.000
d1,D1 OT	d1,VP	-0.138	0.046	0.230	0.996
d3,D2 OT	d3,D1 OT	-0.289	-0.114	0.062	0.480
d3,D2 OT	d3,VP	-0.437	-0.252	-0.068	1.72E-03
d3,D1 OT	d3,VP	-0.323	-0.139	0.045	0.279
d6,D2 OT	d6,D1 OT	-0.185	-0.009	0.167	1.000
d6,D2 OT	d6,VP	-0.408	-0.223	-0.039	7.94E-03
d6,D1 OT	d6,VP	-0.399	-0.214	-0.030	1.23E-02

Table S11. Post hoc pairwise comparisons of percentage of neurons responsive to both S-cues across imaging days and region (Fig3E).

Table S12:

Source	Sum Sq.	d.f.	Mean Sq.	F	Prob>F
day	0.85429	2	0.42714	46.23443	2.439E-11
region	0.32224	2	0.16112	17.43954	3.064E-06
day:region	0.40111	4	0.10028	10.85411	3.918E-06
Error	0.38802	42	0.00924		
Total	1.87808	50			

Table S12. 2-way ANOVA for effect of day or lens placement on percentage of neurons with auROC>0.75 for {S_K vs. P_K} (Fig3I).

Table S13:

Group A	Group B	Lower Limit	A-B	Upper Limit	P-value
d1,D2 OT	d3,D2 OT	-0.259	-0.078	0.103	0.890
d1,D2 OT	d6,D2 OT	-0.279	-0.097	0.084	0.709
d3,D2 OT	d6,D2 OT	-0.201	-0.020	0.162	1.000
d1,D1 OT	d3,D1 OT	-0.293	-0.112	0.069	0.541
d1,D1 OT	d6,D1 OT	-0.417	-0.236	-0.054	0.003
d3,D1 OT	d6,D1 OT	-0.305	-0.124	0.058	0.407
d1,VP	d3,VP	-0.476	-0.278	-0.079	0.001
d1,VP	d6,VP	-0.820	-0.621	-0.423	2.00E-11
d3,VP	d6,VP	-0.542	-0.344	-0.145	4.09E-05
d1,D2 OT	d1,D1 OT	-0.170	0.011	0.192	1.000
d1,D2 OT	d1,VP	-0.141	0.049	0.239	0.995
d1,D1 OT	d1,VP	-0.152	0.038	0.228	0.999
d3,D2 OT	d3,D1 OT	-0.204	-0.023	0.158	1.000
d3,D2 OT	d3,VP	-0.341	-0.151	0.039	0.221
d3,D1 OT	d3,VP	-0.318	-0.128	0.062	0.427
d6,D2 OT	d6,D1 OT	-0.309	-0.127	0.054	0.370
d6,D2 OT	d6,VP	-0.665	-0.475	-0.285	1.15E-08
d6,D1 OT	d6,VP	-0.538	-0.348	-0.158	1.43E-05

Table S13. Post hoc comparisons of percentage of neurons with auROC>0.75 for {S_K vs. P_K} across imaging day and region (Fig3l).

Table S14:

Source	Sum Sq.	d.f.	Mean Sq.	F	Prob>F
day	0.551	2	0.275	28.099	1.794E-08
region	0.377	2	0.188	19.265	1.156E-06
day:region	0.364	4	0.0912	9.310	1.764E-05
Error	0.411	42	0.009		
Total	1.637	50			

Table S14. 2-way ANOVA for effect of day or lens placement on percentage of neurons with auROC>0.75 for {S_K vs. X_K} (Fig3J).

Table S15:

Group A	Group B	Lower Limit	A-B	Upper Limit	P-value
d1,D2 OT	d3,D2 OT	-0.189	-0.002	0.184	1.000
d1,D2 OT	d6,D2 OT	-0.238	-0.052	0.135	0.992
d3,D2 OT	d6,D2 OT	-0.236	-0.049	0.137	0.994
d1,D1 OT	d3,D1 OT	-0.313	-0.126	0.061	0.421
d1,D1 OT	d6,D1 OT	-0.356	-0.170	0.017	0.102
d3,D1 OT	d6,D1 OT	-0.230	-0.044	0.143	0.997
d1,VP	d3,VP	-0.454	-0.250	-0.045	7.23E-03
d1,VP	d6,VP	-0.750	-0.545	-0.341	2.05E-09
d3,VP	d6,VP	-0.500	-0.295	-0.091	8.14E-04
d1,D2 OT	d1,D1 OT	-0.219	-0.033	0.154	1.000
d1,D2 OT	d1,VP	-0.163	0.033	0.229	1.000
d1,D1 OT	d1,VP	-0.130	0.066	0.261	0.972
d3,D2 OT	d3,D1 OT	-0.343	-0.156	0.031	0.167
d3,D2 OT	d3,VP	-0.410	-0.214	-0.019	2.26E-02
d3,D1 OT	d3,VP	-0.254	-0.058	0.138	0.987
d6,D2 OT	d6,D1 OT	-0.337	-0.151	0.036	0.204
d6,D2 OT	d6,VP	-0.656	-0.461	-0.265	5.39E-08
d6,D1 OT	d6,VP	-0.506	-0.310	-0.114	1.95E-04

Table S15. Post hoc comparisons of percentage of neurons with auROC>0.75 for {S_K vs. X_K} across imaging day and region (Fig3J).

Table S16:

Source	Sum Sq.	d.f.	Mean Sq.	F	Prob>F
day	0.01400	2	0.00700	0.45251	0.63909
region	0.08031	2	0.04015	2.59595	0.08650
day:region	0.01282	4	0.00321	0.20726	0.93297
Error	0.64967	42	0.01547		
Total	0.75527	50			

Table S16. 2-way ANOVA for effect of day or lens placement on percentage of neurons with auROC>0.75 for {S_K vs. S_T} (Fig3K).

Table S17:

Group A	Group B	Lower Limit	A-B	Upper Limit	P-value
d1,D2 OT	d3,D2 OT	-0.237	-0.002	0.232	1.000
d1,D2 OT	d6,D2 OT	-0.276	-0.041	0.193	1.000
d3,D2 OT	d6,D2 OT	-0.274	-0.039	0.196	1.000
d1,D1 OT	d3,D1 OT	-0.255	-0.020	0.214	1.000
d1,D1 OT	d6,D1 OT	-0.233	0.001	0.236	1.000
d3,D1 OT	d6,D1 OT	-0.213	0.022	0.257	1.000
d1,VP	d3,VP	-0.316	-0.059	0.198	0.998
d1,VP	d6,VP	-0.336	-0.079	0.178	0.983
d3,VP	d6,VP	-0.277	-0.020	0.237	1.000
d1,D2 OT	d1,D1 OT	-0.267	-0.032	0.202	1.000
d1,D2 OT	d1,VP	-0.142	0.104	0.350	0.900
d1,D1 OT	d1,VP	-0.110	0.136	0.382	0.678
d3,D2 OT	d3,D1 OT	-0.285	-0.050	0.184	0.999
d3,D2 OT	d3,VP	-0.199	0.047	0.293	0.999
d3,D1 OT	d3,VP	-0.149	0.097	0.344	0.928
d6,D2 OT	d6,D1 OT	-0.224	0.011	0.245	1.000
d6,D2 OT	d6,VP	-0.180	0.066	0.312	0.993
d6,D1 OT	d6,VP	-0.191	0.055	0.302	0.998

Table S17. Post hoc comparisons of percentage of neurons with auROC>0.75 for {S_K vs. S_T} across imaging day and region (Fig3K).

Table S18:

Group A	Group B	Lower Limit	A-B	Upper Limit	FDR adjusted P-value
D2 OT	D1 OT	-0.204	-0.138	-0.073	4.37E-02
D2 OT	VP	-0.275	-0.214	-0.153	1.08E-03
D1 OT	VP	-0.120	-0.075	-0.031	0.141

Table S18. Pairwise comparisons of $|\Delta\Delta F_{day3}|-|\Delta\Delta F_{day1}|$ across regions (Fig4I).

Table S19:

Population	Lower Limit	Mean	Upper Limit	FDR adjusted P-value
D2 OT	-0.146	-6.51E-02	1.58E-02	0.259
D1 OT	2.78E-02	7.83E-02	0.129	4.48E-02
VP	0.133	0.174	0.215	2.49E-07

Table S19. One sample t-tests of $|\Delta\Delta F_{day3}|-|\Delta\Delta F_{day1}|$ in different regions (Fig4I).

Table S20:

Source	Sum Sq.	d.f.	Mean Sq.	F	Prob>F
region	0.018	2	9.10E-03	9.569	2.40E-03
Error	0.013	14	9.51E-04		
Total	0.032	16			

Table S20. One-way ANOVA for effect of region on {S vs. X|P} linear classifier accuracy (Fig5G).

Table S21:

Group A	Group B	Lower Limit	A-B	Upper Limit	P-value
D2 OT	D1 OT	-0.114	-0.067	-0.020	5.57E-03
D2 OT	VP	-0.119	-0.070	-0.021	5.65E-03
D1 OT	VP	-0.052	-0.003	0.046	0.985

Table S21. Post hoc comparisons of {S vs. X|P} linear classifier accuracy across regions (Fig5G).

Table S22:

Source	Sum Sq.	d.f.	Mean Sq.	F	Prob>F
region	0.134	2	0.067	14.136	4.37E-04
Error	0.066	14	0.005		
Total	0.201	16			

Table S22. One-way ANOVA for effect of region on generalized {S vs. X|P} linear classifier accuracy (Fig5G).

Table S23:

Group A	Group B	Lower Limit	A-B	Upper Limit	P-value
D2 OT	D1 OT	-0.153	-0.049	0.055	0.451
D2 OT	VP	-0.323	-0.214	-0.105	4.17E-04
D1 OT	VP	-0.274	-0.165	-0.056	3.84E-03

Table S23. Post hoc comparisons of generalized {S vs. X|P} linear classifier accuracy across regions (Fig5G).

Table S24:

Source	Sum Sq.	d.f.	Mean Sq.	F	Prob>F
days	0.775	2	0.387	0.277	0.759
region	50.226	2	25.113	17.969	2.704E-06
days:region	14.484	4	3.621	2.591	0.051

Table S24. 2-way ANOVA for effect of imaging days or region on normalized PR (Fig5l).

Table S25:

Group A	Group B	Lower Limit	A-B	Upper Limit	P-value
d1,D2 OT	d3,D2 OT	-2.938	-0.592	1.754	0.995
d1,D2 OT	d6,D2 OT	-3.700	-1.355	0.991	0.623
d3,D2 OT	d6,D2 OT	-2.999	-0.762	1.474	0.968
d1,D1 OT	d3,D1 OT	-1.948	0.289	2.526	1
d1,D1 OT	d6,D1 OT	-1.965	0.272	2.509	1
d3,D1 OT	d6,D1 OT	-2.254	-0.017	2.220	1
d1,VP	d3,VP	-2.404	0.195	2.794	1
d1,VP	d6,VP	-0.783	1.816	4.415	0.372
d3,VP	d6,VP	-0.829	1.621	4.071	0.445
d1,D2 OT	d3,D1 OT	-3.316	-0.971	1.375	0.907
d1,D2 OT	d1,VP	-1.921	0.678	3.277	0.994
d1,D1 OT	d1,VP	-0.563	1.938	4.438	0.245
d3,D2 OT	d3,D1 OT	-2.615	-0.378	1.858	1
d3,D2 OT	d3,VP	-0.881	1.465	3.811	0.522
d3,D1 OT	d3,VP	-0.502	1.843	4.189	0.229
d6,D2 OT	d6,D1 OT	-1.870	0.367	2.604	1
d6,D2 OT	d6,VP	1.503	3.848	6.194	1.14E-04
d6,D1 OT	d6,VP	1.135	3.481	5.827	5.67E-04

Table S25. Post hoc comparisons of normalized PR across imaging day and region (Fig5l).

Table S26:

Source	Sum Sq.	d.f.	Mean Sq.	F	Prob>F
region	0.209	2	0.104	20.965	6.16E-05
Error	0.070	14	0.005		
Total	0.279	16			

Table S26. One-way ANOVA for effect of region on {S_K vs. P_K} linear classifier accuracy trained on PC1 (Fig5L).

Table S27:

Group A	Group B	Lower Limit	A-B	Upper Limit	P-value
D2 OT	D1 OT	-0.172	-0.066	0.041	0.273
D2 OT	VP	-0.380	-0.268	-0.157	5.64E-05
D1 OT	VP	-0.315	-0.203	-0.091	8.57E-04

Table S27. Post hoc comparisons of {S_K vs. P_K} linear classifier accuracy trained on PC1 across regions (Fig5L).

Table S28:

Source	Sum Sq.	d.f.	Mean Sq.	F	Prob>F
region	0.019	2	0.009	0.646	0.539
Error	0.206	14	0.015		
Total	0.225	16			

Table S28. One-way ANOVA for effect of region on {S_K vs. S_T} linear classifier accuracy trained on PC1-PC15 (Fig5L).

Table S29:

Group A	Group B	Lower Limit	A-B	Upper Limit	P-value
D2 OT	D1 OT	-0.203	-0.019	0.164	0.958
D2 OT	VP	-0.131	0.061	0.253	0.687
D1 OT	VP	-0.111	0.081	0.273	0.529

Table S29. Post hoc comparisons of {S_K vs. S_T} linear classifier accuracy trained on PC1-PC15 across regions (Fig5L).

Table S30:

Source	Sum Sq.	d.f.	Mean Sq.	F	Prob>F
spout	17.176	1	17.176	50.125	2.56E-07
S%	19.415	2	9.707	28.329	4.82E-07
spout:S%	11.533	2	5.767	16.829	2.71E-05
Error	8.224	24	0.343		
Total	56.348	29			

Table S30. 2-way ANOVA for effect of lick spout presence and sucrose contingency on anticipatory licking (Fig6C).

Table S31:

Group A	Group B	Lower Limit	A-B	Upper Limit	P-value
spout=0, S0.0	spout=1, S0.0	-1.205	-0.060	1.085	1
spout=0, S0.0	spout=0, S0.5	-1.335	-0.190	0.955	0.995
spout=0, S0.0	spout=1, S0.5	-2.725	-1.580	-0.435	3.24E-03
spout=0, S0.0	spout=0, S1.0	-1.595	-0.450	0.695	0.825
spout=0, S0.0	spout=1, S1.0	-4.685	-3.540	-2.395	1.66E-08
spout=1, S0.0	spout=0, S0.5	-1.275	-0.130	1.015	0.999
spout=1, S0.0	spout=1, S0.5	-2.665	-1.520	-0.375	4.80E-03
spout=1, S0.0	spout=0, S1.0	-1.535	-0.390	0.755	0.895
spout=1, S0.0	spout=1, S1.0	-4.625	-3.480	-2.335	2.29E-08
spout=0, S0.5	spout=1, S0.5	-2.535	-1.390	-0.245	1.11E-02
spout=0, S0.5	spout=0, S1.0	-1.405	-0.260	0.885	0.980
spout=0, S0.5	spout=1, S1.0	-4.495	-3.350	-2.205	4.70E-08
spout=1, S0.5	spout=0, S1.0	-0.015	1.130	2.275	5.44E-02
spout=1, S0.5	spout=1, S1.0	-3.105	-1.960	-0.815	2.58E-04
spout=0, S1.0	spout=1, S1.0	-4.235	-3.090	-1.945	2.07E-07

Table S31. Post hoc comparisons of anticipatory licking across spout presence and sucrose contingency (Fig6C).

Table S32:

Source	Sum Sq.	d.f.	Mean Sq.	F	Prob>F
days	466.659	5	93.332	1.199	0.308
valence	217.697	2	108.849	1.399	0.248
days:valence	671.044	10	67.104	0.862	0.569
Error	35948.767	462	77.811		
Total	37302.764	479			

Table S32. 2-way ANOVA for effect of imaging day and valence of odor on velocity during cue presentation (FigS6E).

Table S33:

Source	Sum Sq.	d.f.	Mean Sq.	F	Prob>F
days	851.615	5	170.323	0.660	0.654
valence	29846.379	2	14923.189	57.811	3.91E-23
days:valence	2979.836	10	297.984	1.154	0.320
Error	119259.047	462	258.136		
Total	153052.200	479			

Table S33. 2-way ANOVA for effect of imaging day and valence of odor on velocity during unconditioned stimulus (FigS6E).

Table S34:

Group A	Group B	Lower Limit	A-B	Upper Limit	P-value
d1,P	d1,X	5.990	20.970	35.951	1.51E-04
d1,P	d1,S	10.286	25.266	40.246	5.70E-07
d2,P	d2,X	-3.390	11.591	26.571	0.381
d2,P	d2,S	-2.310	12.670	27.651	0.225
d3,P	d3,X	-4.604	10.942	26.488	0.565
d3,P	d3,S	-1.079	14.466	30.012	0.104
d4,P	d4,X	-4.253	11.292	26.838	0.504
d4,P	d4,S	-1.729	13.817	29.363	0.155
d5,P	d5,X	-2.610	12.936	28.482	0.251
d5,P	d5,S	4.085	19.631	35.177	1.45E-03
d6,P	d6,X	-1.619	13.927	29.473	0.145
d6,P	d6,S	10.737	26.283	41.829	5.22E-07
d1,P	d2,P	-5.400	9.580	24.560	0.733
d1,P	d3,P	-5.063	10.203	25.469	0.660
d1,P	d4,P	-4.305	10.961	26.227	0.526
d1,P	d5,P	-6.954	8.311	23.577	0.913
d1,P	d6,P	-10.637	4.628	19.894	1
d2,P	d3,P	-14.643	0.623	15.889	1
d2,P	d4,P	-13.885	1.381	16.647	1
d2,P	d5,P	-16.534	-1.269	13.997	1
d2,P	d6,P	-20.217	-4.951	10.314	1
d3,P	d4,P	-14.788	0.758	16.304	1
d3,P	d5,P	-17.437	-1.892	13.654	1

d3,P	d6,P	-21.120	-5.574	9.971	0.999
d4,P	d5,P	-18.196	-2.650	12.896	1
d4,P	d6,P	-21.878	-6.333	9.213	0.995
d5,P	d6,P	-19.229	-3.683	11.863	1
d1,X	d2,X	-14.780	0.200	15.181	1
d1,X	d3,X	-15.091	0.175	15.441	1
d1,X	d4,X	-13.982	1.283	16.549	1
d1,X	d5,X	-14.989	0.277	15.543	1
d1,X	d6,X	-17.680	-2.414	12.851	1
d2,X	d3,X	-15.291	-0.025	15.240	1
d2,X	d4,X	-14.183	1.083	16.349	1
d2,X	d5,X	-15.189	0.077	15.342	1
d2,X	d6,X	-17.881	-2.615	12.651	1
d3,X	d4,X	-14.437	1.108	16.654	1
d3,X	d5,X	-15.444	0.102	15.648	1
d3,X	d6,X	-18.135	-2.589	12.956	1
d4,X	d5,X	-16.552	-1.006	14.540	1
d4,X	d6,X	-19.244	-3.698	11.848	1
d5,X	d6,X	-18.237	-2.691	12.854	1
d1,S	d2,S	-17.996	-3.015	11.965	1
d1,S	d3,S	-15.862	-0.597	14.669	1
d1,S	d4,S	-15.753	-0.488	14.778	1
d1,S	d5,S	-12.589	2.677	17.942	1
d1,S	d6,S	-9.620	5.646	20.911	0.998
d2,S	d3,S	-12.847	2.419	17.685	1

d2,S	d4,S	-12.738	2.528	17.794	1
d2,S	d5,S	-9.574	5.692	20.958	0.998
d2,S	d6,S	-6.605	8.661	23.927	0.880
d3,S	d4,S	-15.437	0.109	15.655	1
d3,S	d5,S	-12.273	3.273	18.819	1
d3,S	d6,S	-9.304	6.242	21.788	0.996
d4,S	d5,S	-12.382	3.164	18.710	1
d4,S	d6,S	-9.413	6.133	21.679	0.997
d5,S	d6,S	-12.577	2.969	18.515	1

Table S34. Post hoc comparisons of velocity during unconditioned stimulus across imaging days and valence of odor (FigS6E).

Table S35:

Source	Sum Sq.	d.f.	Mean Sq.	F	Prob>F
days	0.293	5	0.059	12.301	8.84E-11
valence	0.014	2	0.007	1.523	0.220
days:valence	0.121	10	0.012	2.546	5.95E-03
Error	1.313	276	0.005		
Total	1.739	293			

Table S35. 2-way ANOVA for effect of imaging day and valence of odor on relative eye size during cue presentation (FigS6G).

Table S36:

Source	Sum Sq.	d.f.	Mean Sq.	F	Prob>F
days	0.178	5	0.036	4.529	5.51E-04
valence	0.040	2	0.020	2.574	0.078
days:valence	0.167	10	0.017	2.123	2.29E-02
Error	2.167	276	0.008		
Total	2.547	293			

Table S36. 2-way ANOVA for effect of imaging day and valence of odor on relative eye size during unconditioned stimulus (FigS6G).

Table S37:

Source	Sum Sq.	d.f.	Mean Sq.	F	Prob>F
ket	0.051	1	0.051	3.828	0.051
val.	0.787	2	0.393	29.766	2.48E-12
reg.	6.62E-03	2	0.003	0.250	0.779
day	0.928	2	0.464	35.101	3.57E-14
ket:val.	0.024	2	0.012	0.911	0.403
ket:reg.	0.018	2	0.009	0.671	0.512
ket:day	0.057	2	0.029	2.163	0.117
val.:reg.	0.622	4	0.155	11.763	8.94E-09
val.:day	0.264	4	0.066	4.995	6.85E-04
reg.:day	0.328	4	0.082	6.212	8.79E-05
ket:val.:reg.	0.054	4	0.014	1.025	0.395
ket:val.:day	0.095	4	0.024	1.796	0.130
ket:reg.:day	0.014	4	0.004	0.272	0.896
val.:reg.:day	0.241	8	0.030	2.277	0.023
ket:val.:reg.:day	0.062	8	0.008	0.582	0.792
Error	3.331	252	0.013		
Total	6.670	305			

Table S37. 4-way ANOVA for effect of imaging day, valence, functional group, and region on the percentage of neurons responsive to a given odor (FigS8A).

Table S38:

Formula:					
Fmag ~ 1 + reg*day + reg*val + day*val + reg:day:val + (1 | id)					
Model information					
# of observations:	**Fixed effects coefficients:**	**Random effect coefficients:**		**Covariance parameters:**	
11,160	12	17		2	
Model fit statistics:					
AIC	**BIC**	**Log Likelihood**		**Deviance**	
9050.1	9152.6	-4511.1		9022.1	
Fixed effects coefficients (95% CIs):					
Name	**Estimate**	**SE**	**tStat**	**DF**	**pValue**
intercept	0.469	0.0155	30.228	11,148	5.43E-193
reg_D1	-0.0222	0.0205	-1.0829	11,148	0.279
reg_VP	0.0192	0.0255	0.753	11,148	0.452
day	-0.0140	0.00707	-1.973	11,148	0.0485
val	-0.0244	0.0190	-1.286	11,148	0.198
reg_D1:day	0.00806	0.00947	0.852	11,148	0.394
reg_VP:day	-0.0101	0.0117	-0.862	11,148	0.389
reg_D1:val	-0.00659	0.0251	-0.262	11,148	0.793
reg_VP:val	-0.0359	0.0312	-1.150	11,148	0.250
day:val	0.00799	0.00866	0.922	11,148	0.356
reg_D1:day:val	0.0294	0.0116	2.539	11,148	0.0111
reg_VP:day:val	0.0826	0.0143	5.762	11,148	8.5E-9

Table S38. Linear model of the fixed effects of region, imaging day, and valence and the random effect of individual animal on |ΔΔF/F| (FigS9A).

Table S39:

Formula:					
auROC {S vs. X|P} ~ 1 + region*day + (1 | id)					
Model information					
Number of observations:	**Fixed effects coefficients:**	**Random effect coefficients:**		**Covariance parameters:**	
1860	6	17		2	
Model fit statistics:					
AIC	**BIC**	**Log Likelihood**		**Deviance**	
-4303.7	-4259.5	2159.8		-4319.7	
Fixed effects coefficients (95% CIs):					
Name	**Estimate**	**SE**	**tStat**	**DF**	**pValue**
intercept	0.617	0.009	68.007	1854	0
reg_D1	-0.002	0.012	-0.186	1854	0.853
reg_VP	-0.037	0.014	-2.665	1854	7.76E-03
day	0.003	0.001	1.874	1854	0.061
reg_D1:day	0.007	0.002	3.484	1854	5.06E-04
reg_VP:day	0.029	0.002	12.056	1854	2.80E-32

Table S39. Linear model of the fixed effects of region and imaging day, and the random effect of individual animals on the auROC of single-neuron {S vs. X|P} classifiers (FigS10F).

Table S40:

Source	Sum Sq.	d.f.	Mean Sq.	F	Prob>F
region	0.030	2	0.015	14.686	1.46E-05
day	0.050	2	0.025	24.336	9.58E-08
region:day	0.041	4	0.010	10.001	8.88E-06
Error	0.043	42	0.001		
Total	0.158	50			

Table S40. 2-way ANOVA for effect of imaging day and region on the median auROC value of {S vs. X|P} classifiers for each animal (FigS10F).

Table S41:

Group A	Group B	Lower Limit	A-B	Upper Limit	P-value
D2 OT,d1	D2 OT,d3	-0.072	-0.012	0.049	0.999
D2 OT,d1	D2 OT,d6	-0.075	-0.014	0.046	0.997
D2 OT,d3	D2 OT,d6	-0.063	-0.003	0.058	1
D1 OT,d3	D1 OT,d6	-0.072	-0.012	0.049	0.999
D1 OT,d1	D1 OT,d3	-0.091	-0.030	0.030	0.779
D1 OT,d1	D1 OT,d6	-0.102	-0.042	0.019	0.387
VP,d1	VP,d3	-0.130	-0.064	0.002	6.62E-02
VP,d1	VP,d6	-0.241	-0.174	-0.108	2.83E-09
VP,d3	VP,d6	-0.177	-0.111	-0.044	7.91E-05
D2 OT,d1	D1 OT,d1	-0.056	0.005	0.065	1
D2 OT,d1	VP,d1	-0.050	0.013	0.076	0.999
D1 OT,d1	VP,d1	-0.055	0.008	0.072	1
D2 OT,d3	D1 OT,d3	-0.074	-0.014	0.047	0.998
D2 OT,d3	VP,d3	-0.103	-0.039	0.024	0.537
D1 OT,d3	VP,d3	-0.089	-0.026	0.038	0.921
D2 OT,d6	D1 OT,d6	-0.083	-0.023	0.038	0.948
D2 OT,d6	VP,d6	-0.210	-0.147	-0.084	7.68E-08
D1 OT,d6	VP,d6	-0.188	-0.124	-0.061	3.44E-06

Table S41. Post hoc comparison of the median auROC value for {S vs. X|P} across imaging day and region (FigS10F).

Table S42:

Formula:					
auROC {S_K vs. S_T} ~ 1 + region*day + (1 | id)					
Model information					
Number of observations:	**Fixed effects coefficients:**	**Random effect coefficients:**		**Covariance parameters:**	
1860	6	17		2	
Model fit statistics:					
AIC	**BIC**	**Log Likelihood**		**Deviance**	
-2908.8	-2864.5	1462.4		-2924.8	
Fixed effects coefficients (95% CIs):					
Name	**Estimate**	**SE**	**tStat**	**DF**	**pValue**
intercept	0.636	0.015	42.040	1854	7.72E-272
region_D1	-0.020	0.021	-0.962	1854	0.336
region_VP	-0.024	0.024	-1.014	1854	0.311
day	9.67E-04	5.25E-03	0.184	1854	0.854
region_D1:day	0.011	0.007	1.622	1854	0.105
region_VP:day	-0.003	0.009	-0.346	1854	0.730

Table S42. Linear model of the fixed effects of region and imaging day, and the random effect of individual animals on the auROC of single-neuron {S_K vs. S_T} classifiers (FigS10G).

Table S43:

Source	Sum Sq.	d.f.	Mean Sq.	F	Prob>F
region	0.011	2	5.54E-03	2.793	0.073
day	2.91E-04	2	1.46E-04	0.073	0.929
region:day	3.66E-03	4	9.16E-04	0.462	0.763
Error	0.083	42	1.98E-03		
Total	0.098	50			

Table S43. 2-way ANOVA for effect of imaging day and region on the median auROC value of {S_K vs. S_T} classifiers for each animal (FigS10G).

Table S44:

Formula:					
score ~ 1 + region*day + (1 | id)					
Model information					
Number of observations:	**Fixed effects coefficients:**	**Random effect coefficients:**		**Covariance parameters:**	
1860	6	17		2	
Model fit statistics:					
AIC	**BIC**	**Log Likelihood**		**Deviance**	
-3219.9	-3175.7	1618		-3235.9	
Fixed effects coefficients (95% CIs):					
Name	**Estimate**	**SE**	**tStat**	**DF**	**pValue**
intercept	-0.023	0.015	-1.563	1854	0.118
region_D1	4.19E-03	0.020	0.204	1854	0.838
region_VP	-0.062	0.023	-2.648	1854	8.16E-03
day	5.84E-03	4.83E-03	1.209	1854	0.227
region_D1:day	6.40E-03	6.45E-03	0.991	1854	0.322
region_VP:day	0.075	7.98E-03	9.384	1854	1.80E-20

Table S44: Linear model of the fixed effects of region and imaging day, and the random effect of individual animals on the single-neuron valence scores (FigS10H).

Table S45:

Source	Sum Sq.	d.f.	Mean Sq.	F	Prob>F
reg	0.070	2	0.035	13.163	3.65E-05
day	0.032	2	0.016	6.073	4.82E-03
reg:day	0.045	4	0.011	4.264	5.50E-03
Error	0.111	42	2.65E-03		
Total	0.253	50			

Table S45. 2-way ANOVA for effect of imaging day and region on the median valence score for each animal (FigS10H).

Table S46:

Group A	Group B	Lower Limit	A-B	Upper Limit	P-value
D2 OT,d1	D2 OT,d3	-0.100	-0.003	0.094	1
D2 OT,d1	D2 OT,d6	-0.109	-0.012	0.086	1
D2 OT,d3	D2 OT,d6	-0.106	-0.008	0.089	1
D1 OT,d1	D1 OT,d3	-0.100	-0.002	0.095	1
D1 OT,d1	D1 OT,d6	-0.102	-0.005	0.092	1
D1 OT,d3	D1 OT,d6	-0.100	-0.003	0.095	1
VP,d1	VP,d3	-0.157	-0.051	0.056	0.819
VP,d1	VP,d6	-0.271	-0.165	-0.058	2.87E-04
VP,d3	VP,d6	-0.220	-0.114	-0.007	2.87E-02
D2 OT,d1	D1 OT,d1	-0.112	-0.015	0.082	1
D2 OT,d1	VP,d1	-0.122	-0.020	0.082	1
D1 OT,d1	VP,d1	-0.107	-0.005	0.097	1
D2 OT,d3	D1 OT,d3	-0.111	-0.014	0.083	1
D2 OT,d3	VP,d3	-0.169	-0.067	0.034	0.447
D1 OT,d3	VP,d3	-0.155	-0.053	0.049	0.736
D2 OT,d6	D1 OT,d6	-0.105	-0.008	0.089	1
D2 OT,d6	VP,d6	-0.275	-0.173	-0.071	6.07E-05
D1 OT,d6	VP,d6	-0.266	-0.164	-0.062	1.41E-04

Table S46. Post hoc comparison of the median valence scores across imaging day and region (FigS10H).

Table S47:

Source	Sum Sq.	d.f.	Mean Sq.	F	Prob>F
reg	0.003	2	0.002	4.286	2.02E-02
day	0.006	2	0.003	7.181	2.08E-03
reg:day	0.004	4	0.001	2.622	4.82E-02
Error	0.017	42	0.000		
Total	0.030	50			

Table S47. 2-way ANOVA for effect of imaging day and region on the median single-neuron MNR accuracy for each animal (FigS11B).

Table S48:

Group A	Group B	Lower Limit	A-B	Upper Limit	P-value
D2 OT,d1	D2 OT,d3	-0.051	-0.013	0.024	0.960
D2 OT,d1	D2 OT,d6	-0.045	-0.007	0.031	0.999
D2 OT,d3	D2 OT,d6	-0.032	0.006	0.044	1
D1 OT,d1	D1 OT,d3	-0.047	-0.010	0.028	0.996
D1 OT,d1	D1 OT,d6	-0.050	-0.012	0.026	0.981
D1 OT,d3	D1 OT,d6	-0.040	-0.002	0.036	1
VP,d1	VP,d3	-0.073	-0.031	0.011	0.294
VP,d1	VP,d6	-0.099	-0.058	-0.016	1.47E-03
VP,d3	VP,d6	-0.068	-0.027	0.015	0.490
D2 OT,d1	D1 OT,d1	-0.052	-0.014	0.024	0.953
D2 OT,d1	VP,d1	-0.037	0.003	0.043	1
D1 OT,d1	VP,d1	-0.023	0.017	0.057	0.896
D2 OT,d3	D1 OT,d3	-0.048	-0.010	0.028	0.994
D2 OT,d3	VP,d3	-0.054	-0.014	0.025	0.955
D1 OT,d3	VP,d3	-0.044	-0.005	0.035	1
D2 OT,d6	D1 OT,d6	-0.057	-0.019	0.019	0.797
D2 OT,d6	VP,d6	-0.087	-0.047	-0.008	9.47E-03
D1 OT,d6	VP,d6	-0.069	-0.029	0.011	0.329

Table S48. Post hoc comparison of median single-neuron MNR accuracy across imaging day and region (FigS11B).

Table S49:

Source	Sum Sq.	d.f.	Mean Sq.	F	Prob>F
reg	2.04E-08	2	1.02E-08	0.040	0.961
day	7.71E-07	2	3.86E-07	1.519	0.231
reg:day	1.22E-06	4	3.05E-07	1.200	0.325
Error	1.07E-05	42	2.54E-07		
Total	1.26E-05	50			

Table S49. 2-way ANOVA for effect of imaging day and region on the median single-neuron MNR shuffled accuracy for each animal (FigS11C).

Table S50:

Source	Sum Sq.	d.f.	Mean Sq.	F	Prob>F
reg	0.074	2	0.037	27.720	2.11E-08
day	0.019	2	9.43E-03	7.066	2.26E-03
reg:day	0.011	4	2.65E-03	1.986	1.14E-01
Error	0.056	42	1.33E-03		
Total	0.157	50			

Table S50. 2-way ANOVA for effect of imaging day and region on the median S-cue/S-cue confusion for each animal (FigS11D).

Table S51:

Group A	Group B	Lower Limit	A-B	Upper Limit	P-value
D2 OT,d1	D1 OT,d1	-0.090	-0.021	0.048	0.985
D2 OT,d1	VP,d1	-0.132	-0.060	0.012	0.174
D1 OT,d1	VP,d1	-0.111	-0.039	0.033	0.700
D2 OT,d3	D1 OT,d3	-0.095	-0.026	0.043	0.940
D2 OT,d3	VP,d3	-0.156	-0.084	-0.011	1.30E-02
D1 OT,d3	VP,d3	-0.130	-0.057	0.015	0.223
D2 OT,d6	D1 OT,d6	-0.084	-0.015	0.054	0.998
D2 OT,d6	VP,d6	-0.204	-0.132	-0.059	1.55E-05
D1 OT,d6	VP,d6	-0.189	-0.116	-0.044	1.46E-04
D2 OT,d1	D2 OT,d3	-0.079	-0.010	0.059	1
D2 OT,d1	D2 OT,d6	-0.094	-0.025	0.044	0.955
D2 OT,d3	D2 OT,d6	-0.084	-0.015	0.054	0.998
D1 OT,d1	D1 OT,d3	-0.084	-0.015	0.054	0.998
D1 OT,d1	D1 OT,d6	-0.088	-0.019	0.049	0.990
D1 OT,d3	D1 OT,d6	-0.073	-0.004	0.065	1
VP,d1	VP,d3	-0.109	-0.033	0.042	0.874
VP,d1	VP,d6	-0.172	-0.097	-0.021	4.11E-03
VP,d3	VP,d6	-0.139	-0.063	0.012	0.165

Table S51. Post hoc comparison of median S-cue/S-cue confusion across imaging day and region (FigS11D).

Table S52:

Source	Sum Sq.	d.f.	Mean Sq.	F	Prob>F
reg	1.60E-03	2	7.99E-04	0.681	0.512
day	0.017	2	8.71E-03	7.426	1.73E-03
reg:day	2.53E-03	4	6.31E-04	0.538	0.708
Error	0.049	42	1.17E-03		
Total	0.070	50			

Table S52. 2-way ANOVA for effect of imaging day and region on the median confusion within functional groups for each animal (FigS11E).

Table S53:

Group A	Group B	Lower Limit	A-B	Upper Limit	P-value
D2 OT,d1	D2 OT,d3	-0.055	0.009	0.074	1.000
D2 OT,d1	D2 OT,d6	-0.033	0.031	0.096	0.804
D2 OT,d3	D2 OT,d6	-0.042	0.022	0.087	0.967
D1 OT,d1	D1 OT,d3	-0.063	0.002	0.066	1
D1 OT,d1	D1 OT,d6	-0.034	0.031	0.095	0.828
D1 OT,d3	D1 OT,d6	-0.036	0.029	0.093	0.871
VP,d1	VP,d3	-0.060	0.011	0.082	1
VP,d1	VP,d6	-0.005	0.066	0.136	0.089
VP,d3	VP,d6	-0.016	0.054	0.125	0.255
D2 OT,d1	D1 OT,d1	-0.061	0.004	0.068	1
D2 OT,d1	VP,d1	-0.067	0.001	0.069	1
D1 OT,d1	VP,d1	-0.071	-0.003	0.065	1
D2 OT,d3	D1 OT,d3	-0.068	-0.004	0.061	1
D2 OT,d3	VP,d3	-0.065	0.003	0.070	1
D1 OT,d3	VP,d3	-0.061	0.006	0.074	1
D2 OT,d6	D1 OT,d6	-0.062	0.003	0.067	1
D2 OT,d6	VP,d6	-0.033	0.035	0.103	0.756
D1 OT,d6	VP,d6	-0.036	0.032	0.100	0.828

Table S53. Post hoc comparison of median within-function group confusion across imaging day and region (FigS11E).

Table S54:

Source	Sum Sq.	d.f.	Mean Sq.	F	Prob>F
region	0.010	2	4.92E-03	0.868	0.427
day	0.178	2	0.089	15.734	7.95E-06
region:day	0.064	4	0.016	2.846	3.56E-02
Error	0.238	42	5.67E-03		
Total	0.476	50			

Table S54. 2-way ANOVA for effect of imaging day and region on the mean accuracy for linear classification of {S vs. X} using population data (FigS12B).

Table S55:

Group A	Group B	Lower Limit	A-B	Upper Limit	P-value
D1 OT,d1	D2 OT,d1	-0.108	0.034	0.176	0.997
D1 OT,d1	VP,d1	-0.018	0.131	0.280	0.127
D2 OT,d1	VP,d1	-0.052	0.097	0.246	0.476
D1 OT,d3	D2 OT,d3	-0.081	0.061	0.203	0.889
D1 OT,d3	VP,d3	-0.153	-0.004	0.145	1
D2 OT,d3	VP,d3	-0.214	-0.065	0.084	0.880
D1 OT,d6	D2 OT,d6	-0.142	0.000	0.142	1
D1 OT,d6	VP,d6	-0.202	-0.053	0.096	0.960
D2 OT,d6	VP,d6	-0.202	-0.053	0.096	0.960
D1 OT,d1	D1 OT,d3	-0.190	-0.048	0.094	0.971
D1 OT,d1	D1 OT,d6	-0.214	-0.072	0.070	0.765
D1 OT,d3	D1 OT,d6	-0.166	-0.024	0.118	1
D2 OT,d1	D2 OT,d3	-0.163	-0.021	0.121	1
D2 OT,d1	D2 OT,d6	-0.248	-0.106	0.036	0.288
D2 OT,d3	D2 OT,d6	-0.227	-0.085	0.057	0.575
VP,d1	VP,d3	-0.338	-0.183	-0.027	1.12E-02
VP,d1	VP,d6	-0.411	-0.256	-0.100	1.02E-04
VP,d3	VP,d6	-0.229	-0.073	0.082	0.830

Table S55. Post hoc comparison of mean {S vs. X} accuracy across imaging day and region (FigS12B).

Table S56:

Source	Sum Sq.	d.f.	Mean Sq.	F	Prob>F
region	0.020	2	0.010	1.776	0.182
day	0.255	2	0.128	22.389	2.41E-07
region:day	0.042	4	0.010	1.822	0.143
Error	0.240	42	5.71E-03		
Total	0.543	50			

Table S56. 2-way ANOVA for effect of imaging day and region on the mean accuracy for linear classification of {S vs. P} using population data (FigS12C).

Table S57:

Group A	Group B	Lower Limit	A-B	Upper Limit	P-value
D1 OT,d1	D2 OT,d1	-0.104	0.038	0.181	0.993
D1 OT,d1	VP,d1	-0.051	0.098	0.248	0.453
D2 OT,d1	VP,d1	-0.089	0.060	0.210	0.920
D1 OT,d3	D2 OT,d3	-0.057	0.085	0.228	0.579
D1 OT,d3	VP,d3	-0.134	0.015	0.165	1
D2 OT,d3	VP,d3	-0.219	-0.070	0.079	0.835
D1 OT,d6	D2 OT,d6	-0.124	0.019	0.161	1
D1 OT,d6	VP,d6	-0.192	-0.043	0.107	0.989
D2 OT,d6	VP,d6	-0.211	-0.062	0.088	0.910
D1 OT,d1	D1 OT,d3	-0.233	-0.090	0.052	0.506
D1 OT,d1	D1 OT,d6	-0.262	-0.119	0.023	0.165
D1 OT,d3	D1 OT,d6	-0.172	-0.029	0.113	0.999
D2 OT,d1	D2 OT,d3	-0.186	-0.043	0.099	0.985
D2 OT,d1	D2 OT,d6	-0.281	-0.139	0.004	0.061
D2 OT,d3	D2 OT,d6	-0.238	-0.096	0.047	0.426
VP,d1	VP,d3	-0.329	-0.173	-0.017	1.97E-02
VP,d1	VP,d6	-0.417	-0.261	-0.105	7.71E-05
VP,d3	VP,d6	-0.244	-0.088	0.069	0.662

Table S57. Post hoc comparison of mean {S vs. P} accuracy across imaging day and region (FigS12C).

Table S58:

Source	Sum Sq.	d.f.	Mean Sq.	F	Prob>F
region	0.085	2	0.042	3.600	0.036
day	0.033	2	0.017	1.415	0.254
region:day	0.042	4	0.010	0.890	0.478
Error	0.493	42	0.012		
Total	0.655	50			

Table S58. 2-way ANOVA for effect of imaging day and region on the accuracy for linear classification of {S_K vs. S_T} using population data (FigS12D).

Table S59:

Group A	Group B	Lower Limit	A-B	Upper Limit	P-value
D1 OT,d1	D2 OT,d1	-0.202	0.003	0.207	1
D1 OT,d1	VP,d1	-0.121	0.094	0.308	0.879
D2 OT,d1	VP,d1	-0.123	0.091	0.306	0.896
D1 OT,d3	D2 OT,d3	-0.238	-0.033	0.171	1
D1 OT,d3	VP,d3	-0.216	-0.002	0.213	1
D2 OT,d3	VP,d3	-0.183	0.032	0.246	1
D1 OT,d6	D2 OT,d6	-0.307	-0.103	0.102	0.776
D1 OT,d6	VP,d6	-0.135	0.079	0.294	0.950
D2 OT,d6	VP,d6	-0.032	0.182	0.397	0.153
D1 OT,d1	D1 OT,d3	-0.199	0.006	0.210	1
D1 OT,d1	D1 OT,d6	-0.227	-0.022	0.182	1
D1 OT,d3	D1 OT,d6	-0.232	-0.028	0.177	1
D2 OT,d1	D2 OT,d3	-0.235	-0.031	0.174	1
D2 OT,d1	D2 OT,d6	-0.332	-0.128	0.077	0.525
D2 OT,d3	D2 OT,d6	-0.302	-0.097	0.107	0.823
VP,d1	VP,d3	-0.314	-0.090	0.134	0.922
VP,d1	VP,d6	-0.261	-0.037	0.187	1
VP,d3	VP,d6	-0.171	0.053	0.277	0.997

Table S59. Post hoc comparison of {S_K vs. S_T} accuracy across imaging day and region (FigS12D).